공학박사 학위논문

Effects of elements doping on properties of tungsten as a plasma-facing material

미량의 합금 원소 첨가가 플라즈마 대면용 텅스텐의 물성에 미치는 영향

2023 년 8 월

서울대학교 대학원

재료공학부

민 건 식 (閔 建 植)

Effects of elements doping on properties of tungsten as a plasma-facing material

지도 교수 한 홍 남

이 논문을 공학박사 학위논문으로 제출함

2023 년 8 월

서울대학교 대학원

재료공학부

민 건 식

민건식의 공학박사 학위논문을 인준함

2023 년 6 월

위 원 장 ______ 박 찬 ______ (인)

부위원장 ______ 한 홍 남 ______ (인)

위 원 ______ 이 명 규 ______ (인)

위 원 ______ 김 형 찬 ______ (인)

위 원 ______ 김 양 후 ______ (인)

ABSTRACT

Tungsten is considered a highly promising candidate for plasma-facing components in fusion reactors due to its unique combination of properties, including a high melting point, high thermal conductivity, and low erosion rate. Nevertheless, the practical application of tungsten in fusion environments is restricted by its low recrystallization temperature and high ductile-to-brittle transition temperature (DBTT). Extensive researches have been conducted to improves the properties of tungsten through the addition of various alloying elements. However, the amounts of alloying elements should be limited to a certain extent in order to avoid the potential plasma instability that arises from the elements. Therefore, this study focuses on fabricating a tungsten material in which minimal amounts of alloying elements, namely yttrium and potassium, were uniformly dispersed throughout the matrix using powder metallurgy techniques. Subsequently, the plasma-facing properties and mechanical properties of the tungsten material were evaluated. Furthermore, experiments and calculations were performed to investigate the relationship between the alloying elements and the resulting properties.

Firstly, the investigation focused on the effect of a small amount of yttrium on the properties of tungsten. Mechanical alloying was employed to disperse less than 0.05 wt.% of yttrium within the tungsten powder and the dispersed yttrium reacted with residual oxygen, resulting in the formation of uniformly distributed yttrium oxide within the matrix during the spark plasma sintering process. The yttrium oxide was identified to be yttria (Y_2O_3) with an average particle size of approximately 20 nm. The presence of nano-sized Y_2O_3 particles played a crucial role in pinning grain boundaries, leading to the formation of a fine-grained microstructure and inhibiting grain growth at elevated temperatures. Furthermore, the high fraction of grain boundaries in the material facilitated the grain boundary diffusion of tungsten atoms during the sintering process, enhancing the overall sinterability. To assess the viability of the Y_2O_3-dispersed tungsten in a nuclear fusion reactor, resistance to deuterium and helium ion irradiation was evaluated. The results confirmed that the Y_2O_3-dispersed specimen exhibited superior irradiation resistance compared to the pure tungsten specimen. Additionally, nanoindentation tests were conducted to analyze the influence of Y_2O_3 particles on the microscopic mechanical properties of tungsten. The distribution of maximum shear stress in the Y_2O_3-dispersed tungsten showed a combination of two lognormal distributions with different mean values. It is due to the introduction of mobile dislocations by the Y_2O_3 particles during sintering, which effectively reduces the microscopic yield stress of the material.

Secondly, the investigation focused on the effect of adding a small amount of potassium on the properties of tungsten. Sintering was performed using tungsten powder doped with approximately 33 wt ppm of potassium under conditions where abnormal grains did not form. The evaporation of potassium during the sintering resulted in the formation of fine bubbles with an average size of approximately 30 nm in tungsten matrix. Uniaxial tensile tests demonstrated that potassium-doped tungsten specimens exhibited lower DBTT compared to pure tungsten specimens despite similar dislocation densities. Through a comparative analysis of dislocation density and maximum shear stress between potassium-doped tungsten and pure tungsten specimens, it was found out that dislocation nucleation played a dominant role in the plastic deformation of potassium-doped tungsten. Molecular dynamics and dislocation dynamics simulations demonstrated that the nano-sized bubbles concentrated stress in the surrounding matrix, facilitating the nucleation of dislocation at lower external stresses. It provided a comprehensive understanding of the mechanism behind the reduction in DBTT in potassium-doped tungsten. Furthermore, an evaluation of the plasma-facing characteristics of potassium-doped tungsten confirmed its excellent thermal stability and resistance to deuterium ion irradiation.

Through this study, it has been confirmed that the properties of tungsten can be significantly enhanced by adding minimal amounts of alloying elements. The production technology that achieves uniform dispersion of minimal elements within a matrix, coupled with a comprehensive understanding of the mechanisms underlying property enhancement, is anticipated to serve as a cornerstone for the future development of manufacturing technologies for high-purity tungsten as a plasma-facing material. Finally, it is believed that this research will provide breakthrough in the field of materials for various extreme environments and pave the way for new avenues in materials development.

Keywords : Tungsten, Plasma-facing material, Ductile-to-brittle transition temperature, Yttrium, Potassium, Plasma-facing properties, Mechanical properties

Student Number : 2019-38391

CONTENTS

LIST OF FIGURES

LIST OF TABLES

Chapter 1. Introduction

1.1. Nuclear fusion reactor

As the global demand for energy continues to increase annually, there has been a significant rise in the emission of greenhouse gases, particularly carbon dioxide (CO_2), resulting from the combustion of fossil fuels (Figure 1). Given the dominant contribution of CO_2 to global warming and subsequent climatic changes, extensive efforts have been dedicated to exploring alternative energy sources that can generate a sufficient amount of energy without emitting CO_2. In this context, nuclear fusion energy has emerged as a compelling solution to address the issue of CO_2 emissions. This promising energy source offers numerous potential advantages, including long-term sustainability, economic viability, and enhanced safety for electricity generation. Furthermore, fusion fuels are abundant and inexpensive, while the production of long-lived radioactive waste is minimized.

The fusion reactor generates energy through the nuclear fusion reaction between deuterium ($\mathrm{D} = {}^{2}_{1}\mathrm{H}$) and tritium ($\mathrm{T} = {}^{3}_{1}\mathrm{H}$), commonly referred to as the D-T reaction. The fusion reaction can be expressed as follows:

$${}^{2}_{1}\mathrm{H} + {}^{3}_{1}\mathrm{H} \rightarrow {}^{4}_{2}\mathrm{He}(3.5\ \mathrm{MeV}) + {}^{1}_{0}\mathrm{n}(14.1\ \mathrm{MeV})$$

This nuclear fusion involves the atomic nuclei that possess positive electric charges. In order to facilitate the bonding of these nuclei and form a new nucleus, the repulsive electric forces must be overcome. It can occur when a significant number of atomic nuclei collide with high velocities under extremely high temperatures. In order for a fusion reaction to take place, it is necessary to elevate the temperature of the plasma to a minimum of 100 million degrees.

Due to this reason, the plasma is confined within a magnetic cage, effectively isolating it thermally from the surrounding materials [1]. The power output is generated through the impact of fast neutrons and highly energetic particles on the reactor walls. The resulting heat, transferred to the blanket structures by the reaction neutrons, is subsequently extracted using a coolant system, which then generates steam and electrical energy through the use of turbines and generators. Among the various concepts for containing the plasma within a magnetic field generated by coils, the tokamak stands out as one of the most extensively studied and promising approaches for achieving controlled thermonuclear fusion power [2]. The International Thermonuclear Experimental Reactor (ITER) is an experimental tokamak reactor that has been planned for construction since 2008.

While magnetic confinement serves to minimize the interaction between hot plasmas and the surrounding materials, complete avoidance of plasma-material interactions is not feasible. In the operational environment, the plasma-facing material (PFM) must be capable of withstanding extreme conditions, including high temperatures, high heat flux, and high ion flux. Therefore, the selection of an appropriate PFM is crucial to ensure the long-term stability of a fusion reactor.

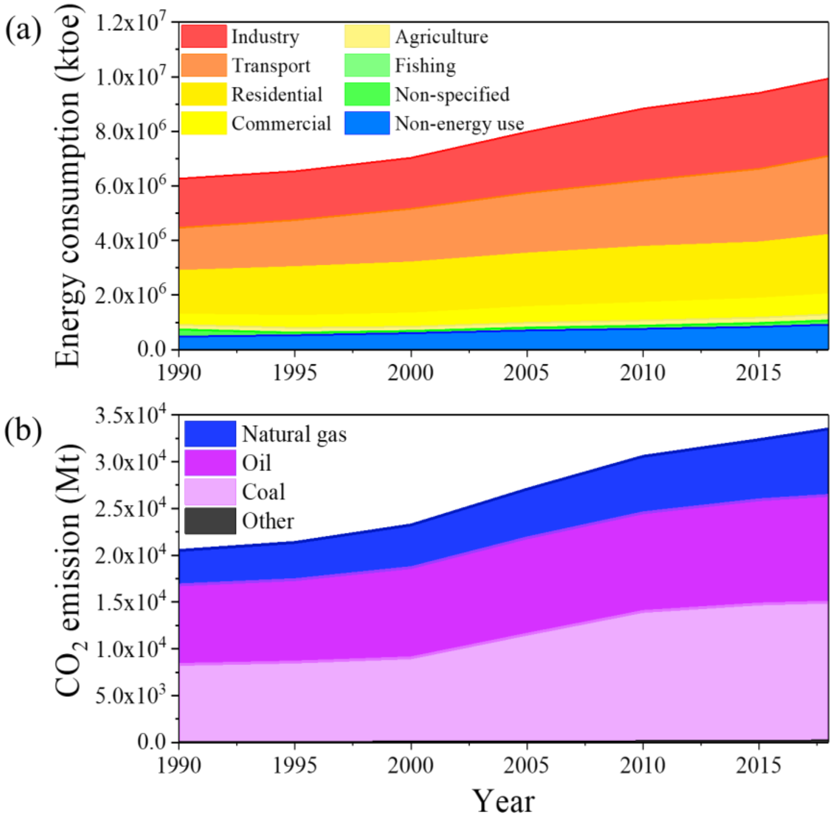

Figure 1 (a) Global energy consumption [3] and (b) CO_2 emission from fossil fuel [4].

1.2. Tungsten as a plasma-facing material

Tungsten is a promising candidate for the plasma-facing components used in extreme environments involving high temperatures and high plasma-ion fluxes, because it exhibits unique properties such as a high melting point, high thermal conductivity, and low erosion rate [5-7]. However, there are several challenging issues that hinder the widespread application of tungsten as a plasma-facing material, such as its low recrystallization temperature and high ductile-to-brittle transition temperature (DBTT).

Tungsten is commonly acknowledged as a hard-to-sinter material. Therefore, the production of commercial pure tungsten typically involves sintering followed by thermomechanical processes. The latter step aims to eliminate any remaining pores from the initial sintering process, resulting in fully dense sintered tungsten [8]. However, tungsten produced through this method often contains numerous dislocations, which adversely affect its mechanical properties due to recrystallization or grain growth at high temperatures [9, 10]. Additionally, the recrystallization of tungsten can lead to embrittlement, making the enhancement of its thermal stability a crucial concern. to overcome this issue, attempts should be made to achieve full densification of tungsten only via sintering.

Spark plasma sintering (SPS) is an effective alternative sintering method in which electric current and pressure are applied simultaneously to powder. Kim et al. [11] suggested that when electric current flows through a polycrystalline metallic material, the charge imbalance formed near a defect weakens atomic bonds and improves atomic mobility. By exploiting these features of SPS, Choi et al. [8] produced pure tungsten with a relative density of 99.9% without any post-processing. However, the hardness of this SPS-produced pure tungsten was lower than that of the commercially obtained pure tungsten produced using sintering and subsequent thermomechanical processes. Therefore, in order to achieve both high thermal stability and excellent mechanical properties simultaneously, alternative strategies such as alloying design are implemented.

The high DBTT of tungsten also significantly restricts its temperature range of applicability [12-14]. In the operational environment of a fusion reactor, where plasma-facing components are exposed to a wide temperature range of 150-2400 °C [15], and undergo intense thermal shock caused by transient events such as edge localized modes [16], the occurrence of such thermal shock can lead to component cracking or failure, and result in accidents such as coolant leakage [17]. Therefore, reducing the DBTT of tungsten is a critical issue for the long-term and reliable utilization of tungsten material in plasma-facing environments.

According to the ITER committee, adherence to specified standards is required for the utilization of tungsten in the divertor, which functions as one of the plasma-facing components in a fusion reactor [18].

- Grain size number: 3 or finer; ASTM E112
- Density: ≥ 19.0 g/cm^3; ASTM B311
- Purity: $\geq$ 99.94%
- Vickers hardness: ≥ 410 HV$_{30}$; ASTM E92

Due to the purity specifications for tungsten, the quantity of dopant elements in tungsten should be restricted.

1.3. Research objectives and structure of thesis

In this study, we aimed to enhance the properties of tungsten by adding minute quantities (< 500 wt ppm) of alloying elements, specifically yttrium and potassium. The doped tungsten samples were fabricated using a powder metallurgical process including SPS. The resulting microstructures and properties of the doped tungsten specimens were meticulously characterized and analyzed, with a particular emphasis on elucidating the correlation between the doped element and the improvement of properties. This thesis is comprised of two main parts.

In Chapter 2. yttrium-doped tungsten powder was prepared through high energy ball-milling and subsequently sintered using the SPS process. Yttrium-rich oxide particles evolve through the reaction between yttrium and residual oxygen atoms during the sintering process. The phase, shape, size, and quantity of these yttrium-rich oxide particles were thoroughly investigated. Additionally, the influence of the oxide dispersion on the sintering behavior, plasma-facing properties, and microscopic mechanical properties of tungsten was explored.

In Chapter 3. potassium-doped tungsten was fabricated using the SPS technique. Potassium-doped tungsten exhibited a lower DBTT when compared to pure tungsten, despite having similar dislocation densities. To gain a comprehensive understanding of the underlying mechanism responsible for this low DBTT, a series of experimental and computational investigations were conducted. The defects present within the specimen were characterized using X-ray diffraction and transmission electron microscopy, while the microscopic plastic behavior of the sintered product was examined through nanoindentation. The relationship between defects and mechanical behavior was further analyzed through molecular dynamics and dislocation dynamics simulations. In addition, the plasma-facing properties of potassium doped tungsten were evaluated.

1.4. References

[1] U. Schumacher, Status and problems of fusion reactor development, Naturwissenschaften 88(3) (2001) 102-12.

[2] E. ITER, Documentation Series No. 24 ITER Technical Basis, IAEA, Vienna http://www-pub.iaea.org/MTCD/publications/PDF/ITER-EDA-DS-24. pdf (2002).

[3] I. data, Based on IEA data from the IEA (2021) Total final consumption (TFC) by sector, World 1990-2018, www.iea.org/statistics. All rights reserved; as modified by Guensik Min, 2021.

[4] I. data, Based on IEA data from the IEA (2021) CO_2 emissions by energy source, World 1990-2018, www.iea.org/statistics. All rights reserved; as modified by Guensik Min, 2021.

[5] M. Merola, D. Loesser, A. Martin, P. Chappuis, R. Mitteau, V. Komarov, R.A. Pitts, S. Gicquel, V. Barabash, L. Giancarli, J. Palmer, M. Nakahira, A. Loarte, D. Campbell, R. Eaton, A. Kukushkin, M. Sugihara, F. Zhang, C.S. Kim, R. Raffray, L. Ferrand, D. Yao, S. Sadakov, A. Furmanek, V. Rozov, T. Hirai, F. Escourbiac, T. Jokinen, B. Calcagno, S. Mori, ITER plasma-facing components, Fusion Engineering and Design 85(10-12) (2010) 2312-2322.

[6] G. Pintsuk, Tungsten as a Plasma-Facing Material, Comprehensive Nuclear Materials2012, pp. 551-581.

[7] S. Wurster, N. Baluc, M. Battabyal, T. Crosby, J. Du, C. García-Rosales, A. Hasegawa, A. Hoffmann, A. Kimura, H. Kurishita, R.J. Kurtz, H. Li, S. Noh, J. Reiser, J. Riesch, M. Rieth, W. Setyawan, M. Walter, J.H. You, R. Pippan, Recent progress in R&D on tungsten alloys for divertor structural and plasma facing materials, Journal of Nuclear Materials 442(1-3) (2013) S181-S189.

[8] J. Choi, H.-M. Sung, K.-B. Roh, S.-H. Hong, G.-H. Kim, H.N. Han, Fabrication of sintered tungsten by spark plasma sintering and investigation of thermal stability, International Journal of Refractory Metals and Hard Materials 69 (2017) 164-169.

[9] Y. Wu, Manufacturing of tungsten and tungsten composites for fusion application via different routes, Tungsten 1(1) (2019) 80-90.

[10] K. Farrell, A.C. Schaffhauser, J.O. Stiegler, Recrystallization, grain growth and the ductile-brittle transition in tungsten sheet, Journal of the Less Common Metals 13(2) (1967) 141-155.

[11] M.-J. Kim, S. Yoon, S. Park, H.-J. Jeong, J.-W. Park, K. Kim, J. Jo, T. Heo, S.-T. Hong, S.H. Cho, Y.-K. Kwon, I.-S. Choi, M. Kim, H.N. Han, Elucidating the origin of electroplasticity in metallic materials, Applied Materials Today 21 (2020).

[12] P. Gumbsch, Brittle fracture and the brittle-to-ductile transition of tungsten, Journal of Nuclear Materials 323(2-3) (2003) 304-312.

[13] A. Giannattasio, M. Tanaka, T.D. Joseph, S.G. Roberts, An empirical correlation between temperature and activation energy for brittle-to-ductile transitions in single-

phase materials, Physica Scripta T128 (2007) 87-90.

[14] S. Nogami, S. Watanabe, J. Reiser, M. Rieth, S. Sickinger, A. Hasegawa, A review of impact properties of tungsten materials, Fusion Engineering and Design 135 (2018) 196-203.

[15] J.-H. You, M. Li, K. Zhang, Structural lifetime assessment for the DEMO divertor targets: Design-by-analysis approach and outstanding issues, Fusion Engineering and Design 164 (2021).

[16] M. Wirtz, J. Linke, T. Loewenhoff, G. Pintsuk, I. Uytdenhouwen, Thermal shock tests to qualify different tungsten grades as plasma facing material, Physica Scripta T167 (2016).

[17] G. Pintsuk, I. Bobin-Vastra, S. Constans, P. Gavila, M. Rödig, B. Riccardi, Qualification and post-mortem characterization of tungsten mock-ups exposed to cyclic high heat flux loading, Fusion Engineering and Design 88(9-10) (2013) 1858-1861.

[18] T. Hirai, V. Barabash, F. Escourbiac, A. Durocher, L. Ferrand, V. Komarov, M. Merola, ITER divertor materials and manufacturing challenges, Fusion Engineering and Design 125 (2017) 250-255.

Chapter 2. Effect of yttrium-doping on tungsten

2.1. Introduction

The dispersion of oxides or carbides is a popular technique for improving hardness and refining the grain size of materials [1-7]. Among these dispersoids, rare earth oxides, such as ThO_2, CeO_2, and Y_2O_3, could be considered suitable for plasma-facing materials exhibiting high strength at high temperatures owing to their high melting point and thermal stability [4, 8, 9]. For example, the dispersion of ThO_2 can contribute to excellent high-temperature mechanical strength. However, their radioactivity poses a significant impediment to their practical application for nuclear reactor [10]. In terms of CeO_2-strengthened W, it has been observed to lower ductile-to-brittle transition temperature (DBTT) while maintaining its thermal conductivity. However, the relative density of the CeO_2-strengthened W did not reach its full density [1]. Unlike ThO_2 and CeO_2, Y_2O_3 exhibits a favorable radiation performance characterized by low activation [11], and contributes to enhancement of sintered density [8], making it a highly attractive option as a dispersoid for tungsten strengthening. In addition, the pinning effect of Y_2O_3 particles helps suppress the mechanical property degradation at high temperatures [12, 13], and the fine-grained microstructure obtained using dispersed Y_2O_3 particles can improve the plasma resistance of materials, because many grain boundaries act as sinks for the defects formed by ion irradiation [14].

Hu et al. [15] found semi-coherent or incoherent interfaces exhibiting low bonding strength at the tungsten– Y_2O_3 interface. Because brittle fracture of tungsten is mainly caused by intergranular cracking, excessive Y_2O_3 addition may lead to a high DBTT. Therefore, the amount of Y_2O_3 must be curbed to suppress the increase in brittleness. However, previous studies have mostly focused on dispersion-strengthened tungsten containing 0.5–5 wt.% Y_2O_3 [16-21]. Consequently, the effects of adding minimal amounts of Y_2O_3 (<0.05 wt.%) on the sinterability and properties of tungsten have hardly been reported.

Oxygen reduces the bonding strength of grain boundaries in tungsten and causes embrittlement [22]. This residual oxygen can be effectively removed during milling or sintering by reacting with yttrium (Y) atoms to form fine Y_2O_3 particles [23]. Therefore, in the present study, a small amount of Y (<0.05 wt.%) was added to tungsten and the resulting effects were analyzed. The composition of Y was determined based on the purity standard (>99.94 wt.% W) of divertor target at the International Thermonuclear Experimental Reactor (ITER) project [24]. The phase, morphology, and size of Y-rich precipitates in the Y-doped tungsten were characterized by transmission electron microscopy (TEM) and small-angle neutron scattering (SANS) analyses. Initially, we identified the influence of mechanical alloying and internal oxidation on the sintering of tungsten by conducting a comparative analysis of the physical properties and microstructure of spark-plasma sintered (SPSed) specimens, prepared by the addition of Y and Y_2O_3, respectively. And Then, the relative densities and densification curves acquired during the SPS of pure and Y-doped tungsten were compared to analyze the effects of Y addition on sinterability. The thermal stabilities of SPSed pure tungsten, SPSed Y-doped tungsten, and commercially obtained pure tungsten specimens were evaluated by analyzing the changes in the microstructure and hardness of samples exposed to various high temperatures (>1000 °C). Additionally, the surface morphologies of plasma ion-irradiated samples were examined by scanning electron microscopy (SEM) to evaluate their resistance to ion irradiation. Nanoindentation experiments were performed to investigate the effect of Y addition on the microscale mechanical behavior of the specimens.

2.2. Experimental procedures

2.2.1 Materials and methods

Commercially obtained pure tungsten powder (TaeguTec; ~0.5 μm, purity 99.9%) and pure Y powder (Sigma Aldrich; <400 μm, purity 99.5%) were used to fabricate the specimens. Tungsten powder was treated in a 99.999% H_2 atmosphere for 2 h at 1200 °C to decrease its oxygen content. The H_2-treated tungsten powder and Y powder were weighed and mixed in an Ar-filled glove box. The amount of Y was set to 0.0394 wt.%, which corresponded to 0.05 wt.% Y_2O_3 in the sample, assuming that all Y atoms reacted with oxygen to form Y_2O_3 during the sample preparation. The pure and Y-doped tungsten powders (denoted as Pure W and W-Y, respectively) were placed in WC-Co vials with milling balls at a ball-to-powder weight ratio of 2:1. The powder was ground in a high-energy ball mill (SPEX Mixer Mill 8000D). The milled powders were subsequently placed in a graphite mold with an inner diameter of 12 mm. A graphite foil was inserted between the mold and powder to serve as a lubricant. During sintering, a graphite spacer was placed between the mold and the electrode. One-step or two-step sintering was performed using an SPS machine. During one-step sintering, the specimen was heated to 1500 °C at a rate of 200 °C/min and maintained at this temperature for 10 min. During two-step sintering, the specimen was heated to 1800 °C at a rate of 50 °C/min, maintained at this temperature for 10 min, cooled to 1400 °C at a rate of 100 °C/min, and then maintained at this temperature for 30 min. Pure W powder was sintered using the two-step method to maximally increase the relative density of the sintered compact [25], whereas W-Y powder was sintered using both the one-step and two-step method. All sintering processes were conducted in vacuum (~10^{-4} atm). A uniaxial pressure of 25 MPa was initially applied and then increased to 65 MPa at 1000 °C. Commercially obtained pure tungsten (Plansee, Austria; purity: 99.97%) manufactured using sintering and thermomechanical processes was used for comparison with the SPSed specimens.

2.2.2 Characterization

The morphologies of the powders and sintered specimens were examined using a field-emission SEM (FE-SEM) device (SU-70, Hitachi) equipped with an electron backscatter diffraction (EBSD) system (EDAX/TSL, Hikari). The specimen surface was mirror-polished with colloidal silica prior to examination. Grain size was measured based on high-angle grain boundaries with a misorientation angle of 15° to adjacent grains. Kernel average misorientation (KAM) maps were acquired to compare the number of dislocations inside the specimens. The average size of milled Pure W and W-Y powder were measured using a laser diffraction particle size analyzer (Mastersizer 3000E, Malvern Panalytical, UK). Nanosized precipitates were observed and characterized by TEM (JEM-2100F, JEOL Ltd.), and the samples for TEM were prepared using a focused-ion-beam device (Helios G4, Thermo Fisher Scientific). The particle size distribution was determined by statistical analysis of approximately 300 particles from several TEM images. SANS was performed to determine the size distribution and volume fraction of nanosized Y-rich particles in the specimens. The SANS measurements were performed using the 18M SANS instrument at the Korea Atomic Energy Research Institute (KAERI). The samples were analyzed at room temperature in two configurations. The wavelengths (λ) of the neutron beam were 5 and 10 Å for sample-to-detector distances of 3.1 and 9.1 m, respectively, with appropriate collimation settings. The scattering vector Q (= $4\pi\sin\theta/\lambda$) ranged from 0.003 to 0.2 $Å^{-1}$.

The hardness of each specimen was measured using a Vickers indenter (Duramin-40 M1, Sturers) and nanoindenter (Ti 750 L UBi, Hysitron) on its polished surface. The load and holding time for the Vickers hardness tests were 3 kg and 10 s, respectively. Nanohardness was measured using a Berkovich-type diamond indenter tip with loading and unloading rates of ±400 $\mu N \cdot s^{-1}$ and a maximum load of 2000 μN. To exclude the effects of grain boundaries from the nanohardness measurements, only the tests conducted on the grain interior were selected with the assistance of scanning probe microscopy. A total of 56, 65, and 78 nanoindentation tests was analyzed for Pure W, W-Y, and commercially obtained pure tungsten specimens, respectively.

To quantitatively analyze the effects of Y addition on sinterability, the densification curves of Pure W and W-Y powders were obtained by conducting SPS at various temperatures. To that end, the samples were heated at a rate of 200 °C/min, maintained at a specific temperature for 5 s, and then cooled in air. The relative densities of the specimens were measured using the Archimedes method, with the theoretical densities of W and Y_2O_3 set as 19.25 and 5.03 g/cm^3, respectively.

To investigate thermal stability, the specimens were annealed at 1000, 1300, and 1700 °C for 1 h in an atmosphere of 95% Ar and 5% H_2, and the resulting changes in microstructure and hardness were probed. Additionally, specimens with a diameter of 10 mm were irradiated with deuterium using an electron-cyclotron-resonance (ECR) system. The incident ion energy was 100 eV per D_2^+, and the corresponding target bias and plasma potential were −87 V and 13 V, respectively. The ratio of D^+, D_2^+ and D_3^+ ion fluxes on the specimens was estimated to be 5:80:15 by the hydrogen global model [26], and the total ion flux was 4.74×10^{21} D^+ m^{-2} s^{-1}. All specimens were exposed for 4 h, which corresponded to a total fluence of ~6.8×10^{25} D^+ m^{-2}. The deuterium retention of each specimen was examined using thermal desorption spectroscopy (TDS). The TDS temperature range was 300–1273 K with a heating rate of 12 K s^{-1}, which satisfied the Redhead approximation and the Kissinger equation for the analysis of desorption energy from the TDS spectra [27]. The retained amount of deuterium was calculated by integrating the release rate with respect to the temperature in the TDS spectrum. In addition, the specimens were subjected to a He^+ ion radiation using an ECR system to assess their radiation resistance. The incident ion energy was set to 50 eV per He^+ ion and the target temperature was maintained at 1000 K, which is a condition where a fuzz structure is observed in tungsten [28, 29] . The surface of the specimens was irradiated with a fluence of 8.5×10^{25} He^+ m^{-2} for 240 min. Throughout the experiment, the pressure was maintained at 2.5 mtorr of He.

2.3. Results and discussion

2.3.1 Characterization of powders and specimens

In order to determine the optimal milling time for W-Y powder, the powder was subjected to high-energy ball milling for various durations, and the resulting morphologies were examined using SEM. Figure 2 (a) illustrates the initial microstructure of the W-Y powder, which retained its pristine tungsten particle size (~0.5 μm) but exhibited a slightly interconnected structure due to the high temperature during the prior H_2-treatment. Due to the low Y content, larger Y particle (~400 μm) was not discernible in the SEM observation. After 0.5 h of milling, although the particles were combined together, the initial morphology was still observed in Figure 2 (b). However, with milling times exceeding 1 hour, the original structure was completely lost, and a rounded shape was formed. Figures 2 (c and d) show that the particle size of W-Y can be decreased further with prolonged milling.

To quantitatively evaluate the effect of milling time on grain refinement of W-Y powder, X-ray diffraction (XRD) analysis was performed, and the crystallite sizes of the milled powders were determined. The crystallite size ($d_{crystallite}$) was calculated using the Scherrer equation as follows [30, 31]:

$$d_{crystallite} = \frac{K\lambda}{\beta \cos\theta} \tag{2}$$

where, K is shape factor which is generally equal to 0.9, λ is a wavelength of X-ray, β is a full-width half-maximum, and θ is a Bragg angle. Figure 3 (a) illustrates the XRD pattern of the milled W-Y powders. It is evident that only the diffraction peak corresponding to the tungsten was detected, which can be attributed to the low Y content. In Figure 3 (b), it can be observed that the crystallite size decreases as the milling time increases, reaching saturation after 2 h. Based on this finding, a milling time of 2 h was selected to maximize the milling effect while minimizing potential contamination from the vial and balls. Figures 4 (a and b) show microstructures of the 2 h-milled Pure W and W-Y powders, respectively. The particles in both powders had a rounded morphology. Moreover, the particle sizes of Pure W and W-Y powders ranged from a few to several tens of μm, with median values of 11.5 and 11.1 μm, respectively (Figure 5). This indicated that the shape and size of the milled Pure W and W-Y powders did not show any significant differences.

Figures 6 (a, b, and c) show microstructures of the SPSed specimens. Uniform microstructures were observed in all specimens, and the average grain sizes in Pure W, two-step W-Y, and one-step W-Y were determined to be 14.81 μm, 8.74 μm, and 2.07 μm, respectively (Table 1). Pure W was exposed to a higher temperature than that of W-Y during SPS, and the dispersoid-induced pinning effect did not exist in the specimen. Therefore, Pure W had a coarser microstructure than those of W-Y specimens owing to its faster grain growth. Figures 6 (d, e, and f) show maps of Pure W, two-step W-Y, and one-step W-Y, respectively. Pure W exhibited relatively higher KAM values only near grain boundaries; however, W-Y specimens showed relatively high KAM values over the entire region. The average KAM values of Pure W and W-Y were 0.21, 0.40, and 0.43, respectively, indicating that W-Y contained more dislocations than Pure W. The dislocations formed by the pressure applied during SPS can be eliminated by high sintering temperatures and sufficient holding times [32]. Meanwhile, many dislocations presumably remained in W-Y specimens due to the presence of dispersoids within the samples, which hindered the movement and annihilation of the dislocations.

Figure 7 illustrates the hardness of the Y_2O_3-dispersion strengthened tungsten specimens prepared in this study, compared with those in the extant literature. It can be observed that the hardness of tungsten showed a tendency to increase with higher Y_2O_3 content. However, in certain cases, the hardness did not exhibit a significant difference compared to that of pure tungsten, even with a large amount of Y_2O_3 added. This suggests that process optimization is necessary to achieve the desired effect of strengthening through the addition of Y_2O_3. In this paper, the hardness of the two-step Pure W specimen was measured to be 357.86 ± 6.33 HV_3, which is comparable to the hardness reported in a previous study on pure tungsten (354 ± 0.72 $HV_{0.01}$ [8]). On the other hand, the hardness of the two-step and one-step W-Y specimens was measured to be 411.57 ± 2.49 HV_3 and 565.11 ± 3.59 HV_3, respectively. The disparity in hardness observed between the two W-Y specimens is believed to be attributable to differences in grain size. In particular, achieving a high hardness level, such as that of the one-step W-Y specimen, is only possible through the addition of Y_2O_3 exceeding 2 wt.% using conventional methods. Hence, it is evident that a minute amount of Y_2O_3 can be effectively dispersed within the tungsten matrix by employing the technique of mechanical alloying and internal oxidation. In subsequent discussions, our focus will be on the one-step W-Y specimen, which exhibited a superior dispersion strengthening effect compared to the other W-Y specimen. The specimens were then intentionally destroyed and the fracture surfaces were examined to observe pores and dispersoids (Figure 8). Significant intergranular fracture was observed in both Pure W and one-step W-Y. This type of fracture generally occurs when tungsten is fractured at temperatures below the DBTT [33, 34]. Moreover, numerous pores were present at the grain boundary and grain triple junction in Pure W (Figures 8 (a and c)). These pores had a spherical or irregular shape, and their size varied from several hundreds of nm to several tens of μm. In contrast, pores were hardly observed on the fracture surface of W-Y, although this sample was fabricated by one-step sintering. These results are consistent with the relative densities of Pure W (97.71%) and one-step W-Y (99.77%) (Table 1). Additionally, second-phase particles that were several tens of nm in size were observed at the grain triple junction in W-Y (Figures 8 (b and d)). These particles assisted in pinning grain boundaries, thereby contributing to the grain refinement of W-Y. The high relative density and small grain size presumably resulted in the large difference in hardness between W-Y (565.11 HV_3) and Pure W (357.86 HV_3).

TEM analysis was performed to characterize the second-phase particles in W-Y. In the grain interior of the W-Y specimen (Figure 9 (a)), dark spherical second-phase particles were dispersed at the grain boundaries and inside the grains. TEM-EDS analysis of the red-circled region in Figure 9 (a) indicated that the area comprised 38 at% Y, 41 at% oxygen, and 21 at% W, suggesting that the particle was a Y-rich oxide (Figure 9 (c)). In the WO_3– Y_2O_3 alloy system [35], various types of W-Y oxides, such as Y_2O_3 [36-38], Y_2WO_6 [39, 40], and Y_6WO_{12} [41], can be formed depending on the powder state and sintering conditions. Thus, selective area electron diffraction (SAED) analysis was performed to identify the phase of the oxide in W-Y (Figure 9 (b)). The obtained patterns corresponded to the $[01\bar{1}]$ zone axis of Y_2O_3.

The sizes of these particles ranged from several tens of nm to a hundred nm, with the average estimated value being approximately 23.56 nm (Figure 10 (a)). This finding is consistent with the SEM image depicted in Figure 8 (d). The influence of precipitation sites on the size distribution was investigated by distinguishing particles located at the grain boundary from those within the grain (Figure 10 (b)). The average particle size at the grain boundary (~27.80 nm) was larger compared to that within the grain interior (~20.74 nm), indicating enhanced diffusion near the grain boundary. The ratio of the number of particles at the grain boundary to those within the grain interior was found to be 2:3.

SANS is a suitable technique for measuring the quantity and size of nanosized particles in a matrix because the scattered beams can penetrate deeply into specimens and permit volumetric sampling. The scattering intensity *I(Q)* is obtained by summing the information corresponding to the matrix (background) and that obtained from scattering centers (defects). The scattering intensity of the matrix initially follows Porod's law [42].

$$I(Q) = B/Q^n \tag{1}$$

where *B* is the Porod prefactor, and *n* is the Porod exponent related to the structure of the scattering object. The *I(Q)* corresponding to the scattering centers, which has various forms depending on the type of defect, can be expressed as follows for spherical precipitates [43]:

$$I(Q) = \Delta\eta^2 \int_0^\infty \left(\frac{4}{3}\pi R^3\right) N(R) \big(F(Q,R)\big)^2 dR \tag{2}$$

where Δη is the difference in scattering length density between the precipitates and matrix, *R* is the radius of the spherical particles, *N(R)* is the number of particles per unit volume, and *F(Q, R)* is the particle-shape-dependent form factor. The particles were assumed to be spherical, based on the SEM (Figure 8 (d)) and TEM (Figure 9 (a)) images. The form factor for a spherical particle is expressed as follows:

$$F(Q,R) = 3\frac{sin(QR) - QR\,cos(QR)}{(QR)^3} \tag{3}$$

A log-normal distribution was assumed for the size distribution of the precipitates in real space, and the parameters were determined using the least-squares method with SASfit software.

$$N(R) = N_0\, exp\left(-\frac{1}{2}\left(\frac{ln\, R - ln\, R_0}{s}\right)^2\right) \tag{4}$$

Here, N_0 is a scaling factor, and R_0 and s are parameters related to the center and width of the distribution, respectively. This log-normal distribution was fitted to a Q range of 0.003–0.2 $Å^{-1}$. Additionally, the average size ($\langle R \rangle$) and volume fraction (V_f) were calculated as follows:

$$\langle R \rangle = \frac{\int RN(R)dR}{\int N(R)dR}, \qquad V_f = \int \frac{4}{3}\pi R^3 N(R)dR \tag{5}$$

Figure 11 (a) shows a log–log plot of the scattering intensity as a function of the scattering vector. The Porod exponents of Pure W and W-Y were determined to be 4.0 and 3.6, respectively. The Porod exponent is known to range from 3 to 4 and be close to 3 when the material has a high dislocation density [44, 45]. Considering that the average KAM value of the W-Y specimen was higher than that of Pure W (Figures 6 (d and f)), the low Porod exponent of W-Y can be viewed as additional evidence for the numerous dislocations in the specimen. It is worth noting that the Pure W data were fitted with a single background curve in spite of the numerous pores in the sample (Figures 8 (a and c)). This was possibly because most pores in Pure W were larger than 100 nm, which was the upper limit that could be measured under the experimental conditions adopted in this study. Meanwhile, scattering induced by the Y_2O_3 precipitates (red dashed line in Figure 11 (a)) was detected in the analysis of W-Y. The number density and volume fraction of Y_2O_3 in W-Y are shown in Figure 11 (b) and Figure 11 (c), respectively. The average size of Y_2O_3 was determined to be 22.25 nm, which is similar to the value estimated from the TEM images (23.56 nm). Additionally, the volume fraction of Y_2O_3 was 0.145 vol.%, which is close to the theoretical value (0.191 vol.% or 0.05 wt.%). Overall, these results confirmed that a small amount of nanosized Y_2O_3 was dispersed via internal oxidation during SPS.

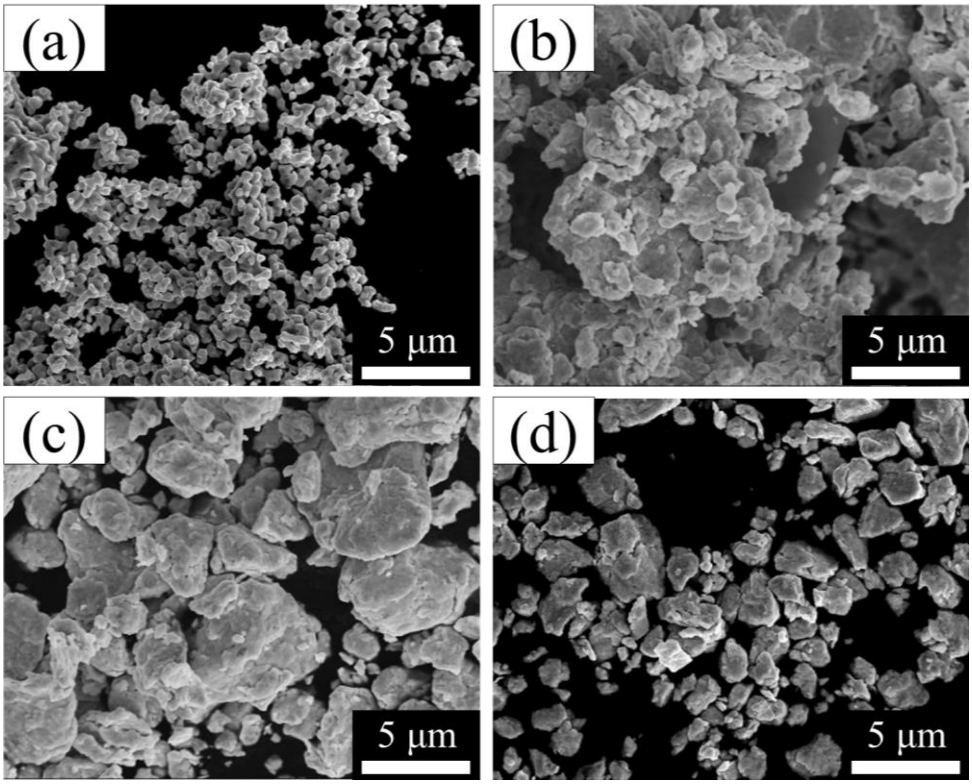

Figure 2 SEM images of W-Y powders milled with different milling durations; (a) initial, (b) 0.5 h milled, (c) 1 h milled, and (d) 2 h milled powder.

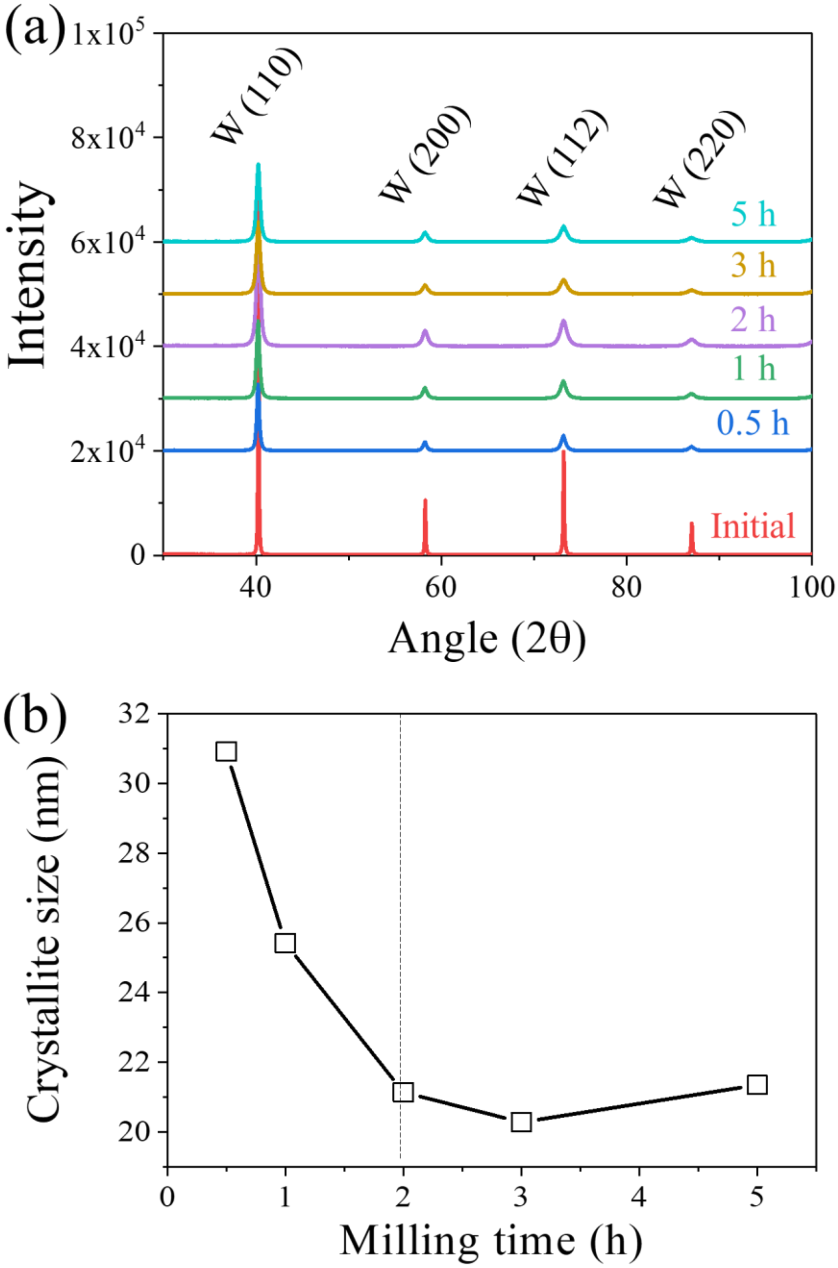

Figure 3 (a) XRD pattern of W-Y powders milled with different milling durations, and (b) crystallite size as a function of milling time.

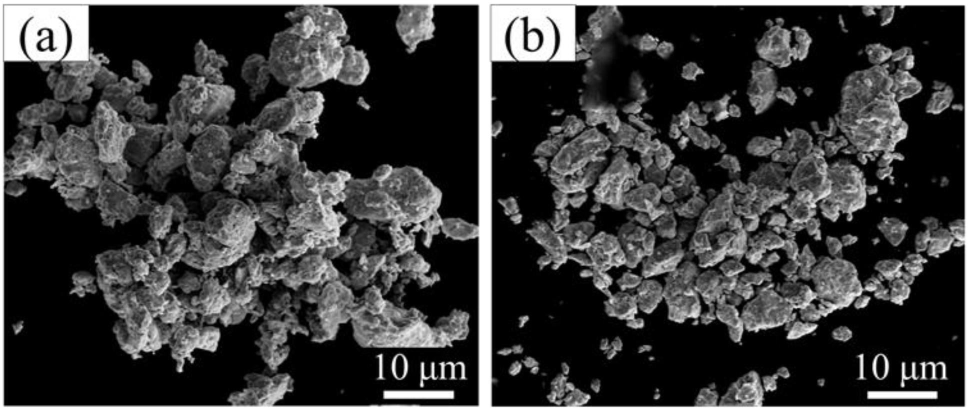

Figure 4 SEM images of ball-milled (a) Pure W and (b) W-Y powders.

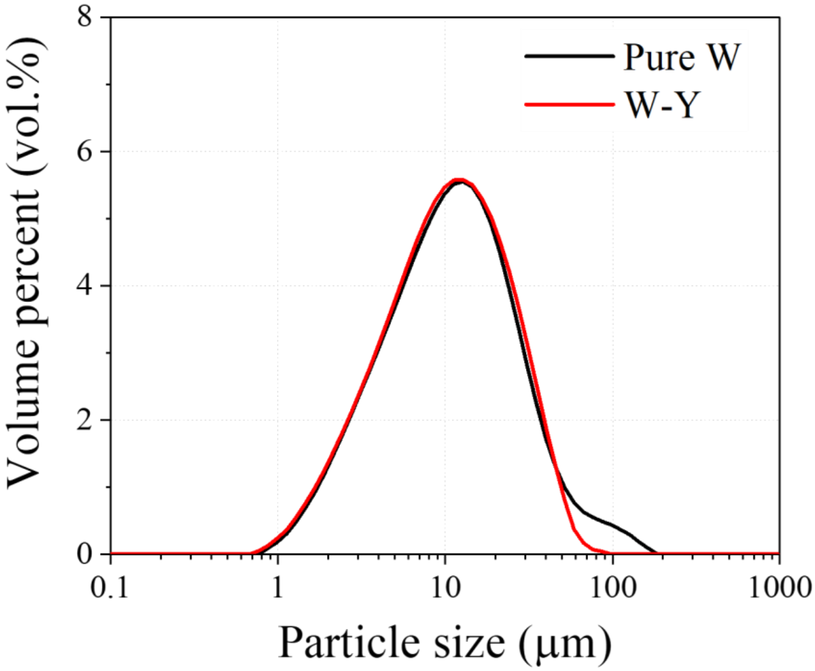

Figure 5 Particle size distribution of Pure W and W-Y milled for 2 h.

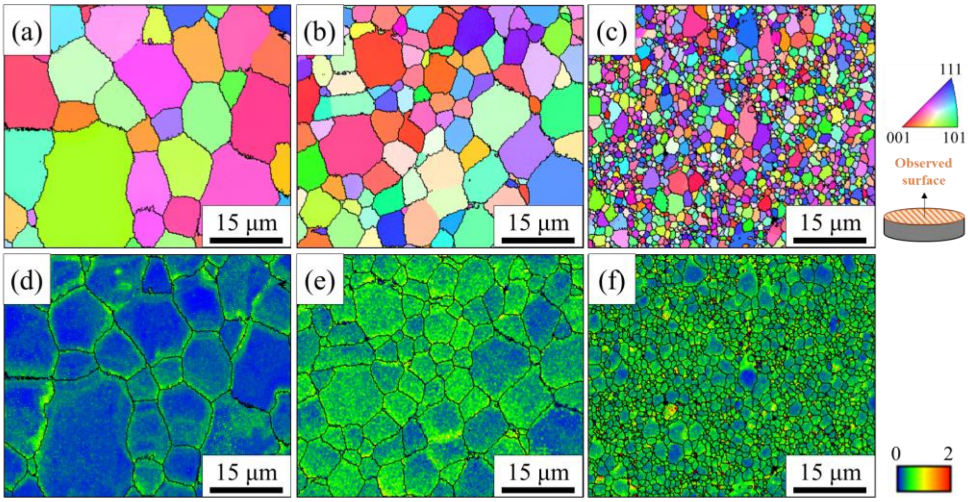

Figure 6 Inverse pole figure (IPF) maps along the normal direction (ND) on the top surface of (a) two-step SPSed Pure W, (b) two-step SPSed W-Y, and (c) one-step SPSed W-Y specimens; the corresponding KAM maps of (d) two-step SPSed Pure W, (e) two-step SPSed W-Y, and (f) one-step SPSed W-Y specimens.

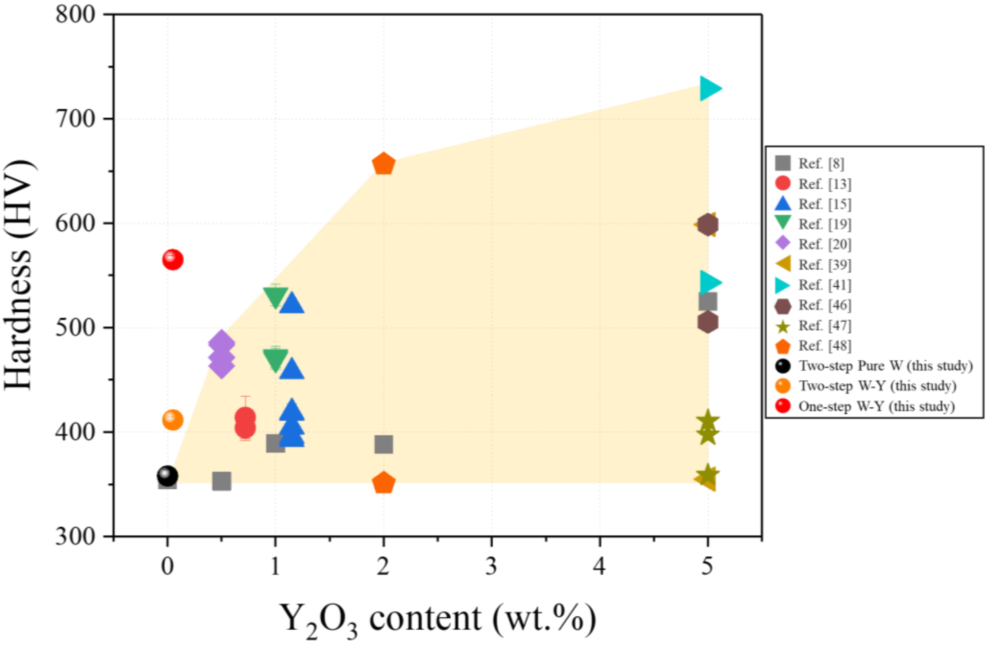

Figure 7 Vickers hardness of the W-Y_2O_3 alloy developed previously ([8, 13, 15, 19, 20, 39, 41, 46-48]) and in this study.

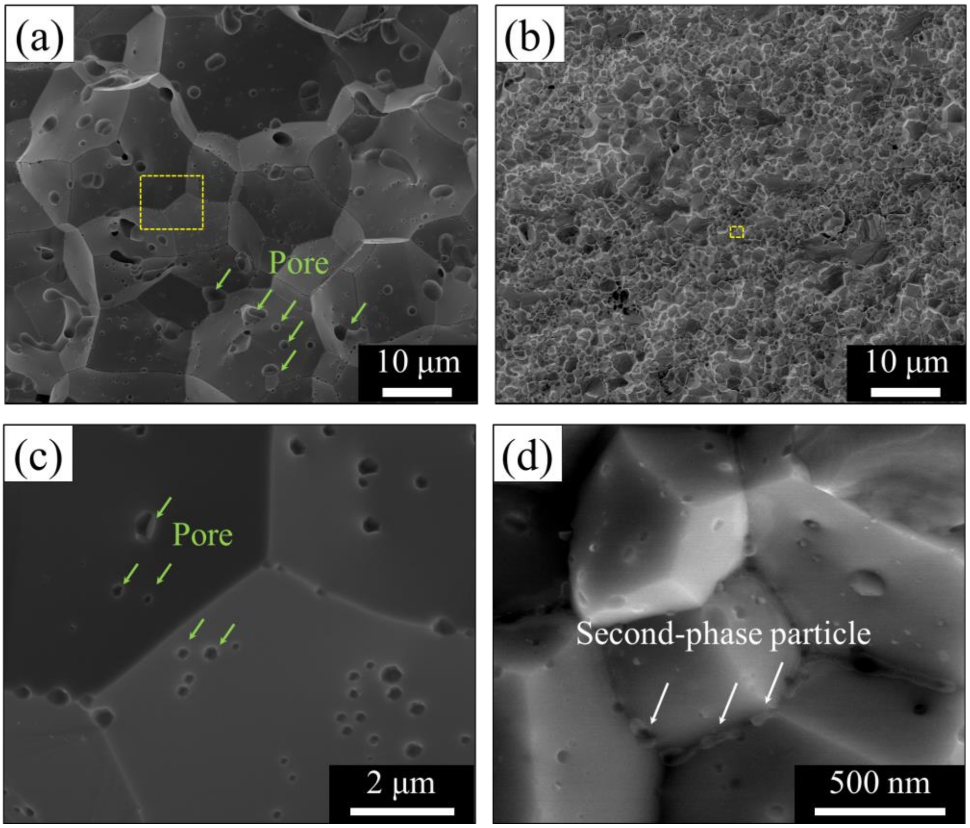

Figure 8 Fractured surfaces of SPSed (a, c) Pure W and (b, d) W-Y alloys. (c) and (d) show high-magnification images of the yellow squares displayed in (a) and (b), respectively.

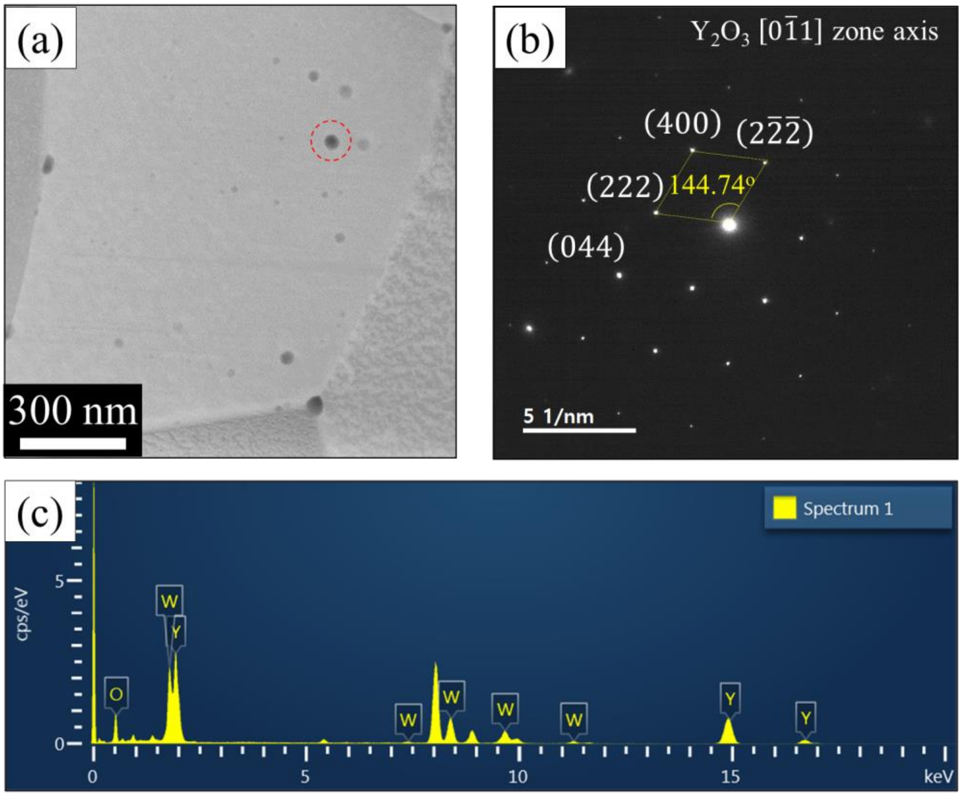

Figure 9 (a) High-angle annular dark-field scanning TEM image of an SPSed W-Y specimen. (b) SAED pattern of the red-circled region in (a). (c) EDS profile of the red-circled region in (a).

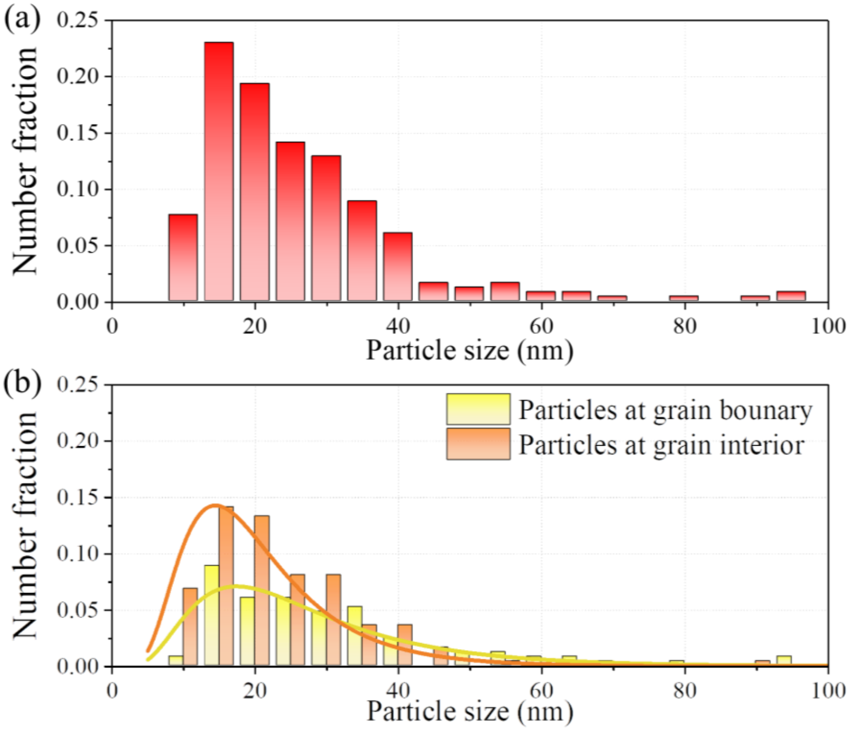

Figure 10 Size distribution of Y_2O_3 particles in W-Y specimen; (a) size distribution for all particles, (b) size distribution for particles present at the grain boundary and inside the grain.

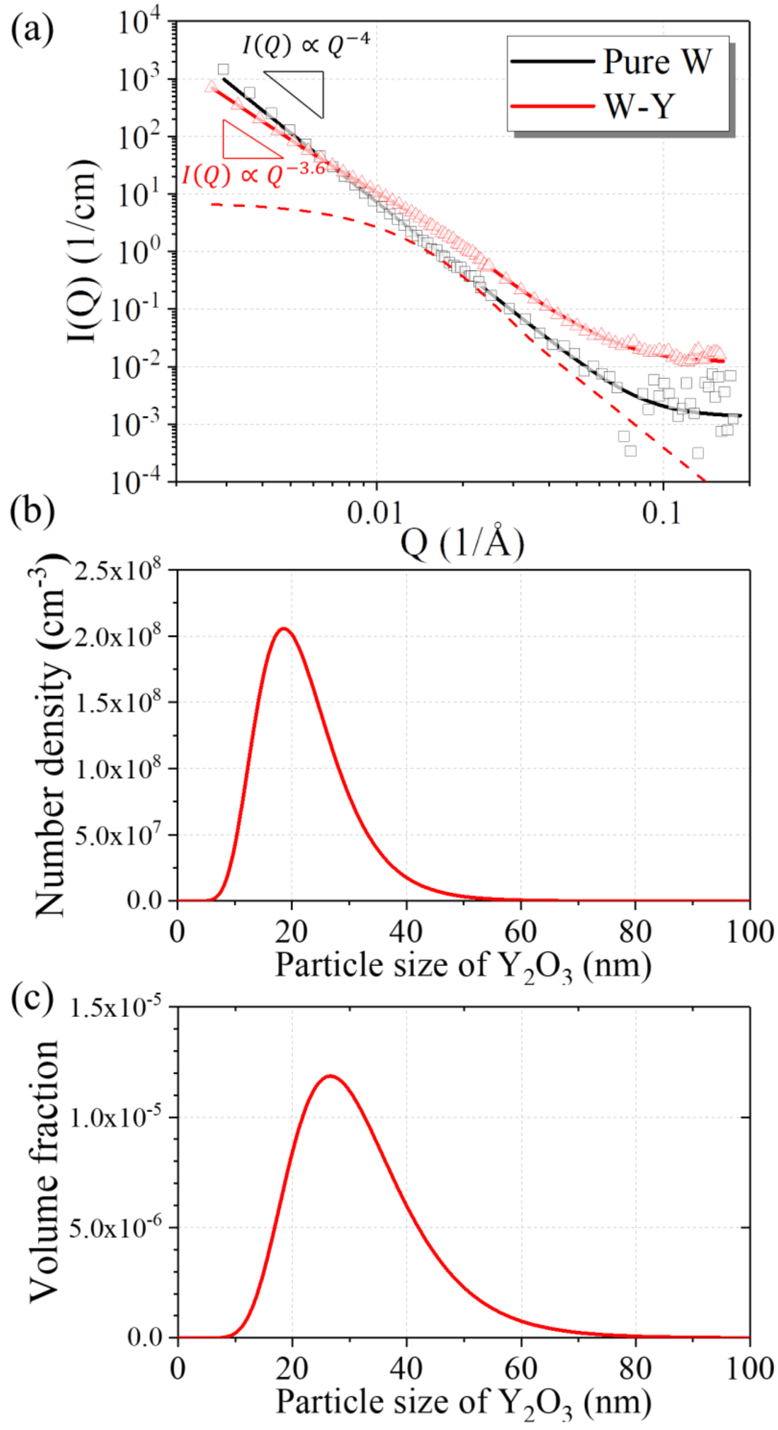

Figure 11 (a) SANS data (symbols) of SPSed Pure W and W-Y samples, and the corresponding fits (lines). (b) Number density and (c) volume fraction of Y_2O_3. The dashed red line in (a) represents the scattering intensity of the Y_2O_3 particles in W-Y.

Table 1 Characterization of two-step Pure W, two-step W-Y, and one step W-Y specimens.

	Relative density (%)	**Hardness (HV_3)**	**Grain size (μm)**
Two-step Pure W	97.71	357.86 ± 6.33	14.81 ± 6.31
Two-step W-Y	99.59	411.57 ± 2.49	8.74 ± 3.80
One-step W-Y	99.77	565.11 ± 3.59	2.07 ± 1.35

2.3.2 Effect of mechanical alloying and internal oxidation

To validate the benefits of mechanical alloying and internal oxidation, W-Y_2O_3 specimen was prepared using powder, in which 0.05 wt.% of Y_2O_3 was directly mixed with tungsten, and were subsequently compared with W-Y specimens. Commercial Y_2O_3 powder (Sigma Aldrich; purity 99.999%) were used to fabricate the specimen. The milling and sintering conditions were set identically to those employed for the one-step W-Y specimen. The SEM observations show that the W-Y_2O_3 specimens exhibit a uniform microstructure with a small number of pores (Figure 12 (a)). The average grain size of W-Y_2O_3 was measured to be 3.47 ± 2.15 um, which was larger than that of W-Y (2.07 ± 1.35 um). This discrepancy in grain size is potentially associated with the size and distribution of Y_2O_3 precipitates. To examine the morphology of the precipitates within the W-Y_2O_3 specimen, the sample was deliberately fractured, and the fractured surface was investigated (Figure 12 (b)). Similar to the W-Y specimen, the fractography of the W-Y_2O_3 specimen predominantly exhibited intergranular fractures. The high-magnification image shows the spherical precipitates with sizes of several tens of nanometers at the grain triple junction (indicated by white arrows in the inset of Figure 12 (b)).

For conducting a statistical analysis of the size of spherical Y_2O_3 particle, the particle sizes were measured from several TEM images, and a histogram was generated to illustrate the distribution (Figure 13). The average particle size in the W-Y_2O_3 specimen was measured to be 31.25 ± 16.14 nm, which exceeded that in the W-Y specimen (23.56 ± 13.94 nm). Additionally, the number of particles per unit area in the W-Y_2O_3 and W-Y specimen was found to be 8.14 μm^{-2} and 14.89 μm^{-2}, respectively. These two observations indicate that Y_2O_3 is more finely distributed within the tungsten matrix when using mechanical alloying and internal oxidation, rather than direct mixing of Y_2O_3. In general, it is widely known that when a material contains a same amount of precipitates, the hardness of the material increases as the size of the precipitates decreases. Indeed, the Vickers hardness of the W-Y_2O_3 specimen was measured as 526.64 ± 4.19 HV_3, which was lower than that of the W-Y specimen (565.11 ± 3.59 HV_3, Table 1). It demonstrates that the simultaneous utilization of mechanical alloying and internal oxidation is more effective in producing oxide-dispersion-strengthened tungsten compared to the direct mixing of oxides.

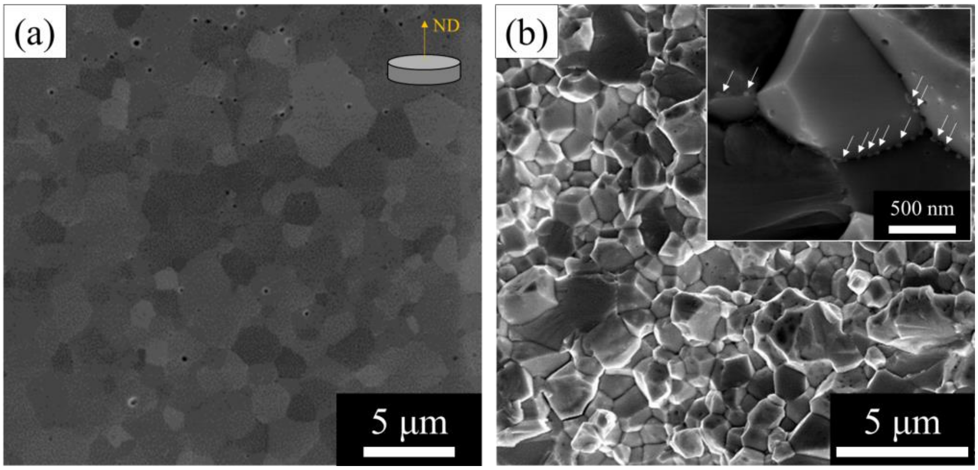

Figure 12 (a) SEM image on the top surface and (b) fractured surface of W-0.05 wt.%Y_2O_3 specimen. The inset in (b) is a high-magnification image of the fractured surface (white arrows indicate precipitates).

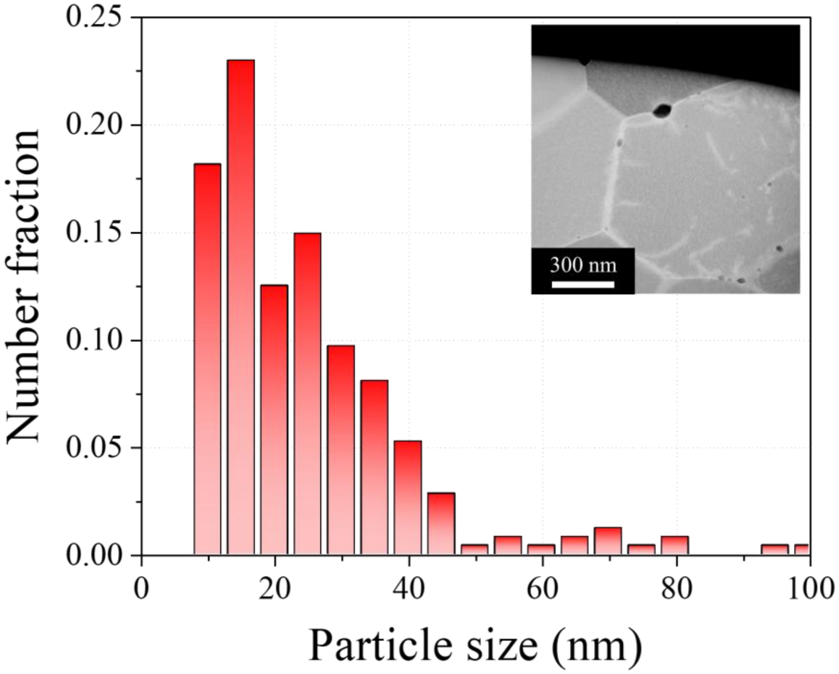

Figure 13 Size distribution of Y_2O_3 particles in W-Y_2O_3 specimen. The inset is a TEM image of W-Y_2O_3 specimen.

2.3.3 Effect of yttrium-doping on sinterability of tungsten

Pure W and W-Y powders were sintered using an SPS machine to obtain their densification curves. Time, temperature, and displacement data were collected at a rate of 5000 times per minute during the sintering. The temperature of the specimens was determined using a pyrometer at a depth of 3.2 mm from the surface of the mold. Downward displacement was measured using a linear variable differential transformer mounted on top of the sintering machine (Figure 14). The thickness (*t*) of the specimen and displacement (*d*) were related as follows:

$$d = d_{max} - (s_1 + s_2 + p_1 + p_2 + t) \tag{6}$$

where d_{max} is the maximum displacement permitted by the machine; s_1 and s_2 are the heights of the lower and upper graphite spacers, respectively; and p_1 and p_2 are the heights of the lower and upper graphite punches, respectively.

Because the graphite spacers and punches expanded thermally at high temperatures, the displacement difference (Δd) at a specific temperature was calculated after repeated sintering to exclude the thermal expansion and obtain only the thickness of the sample. The sintering was performed at 1900 °C at a heating rate of 200 °C/min, and the specimen was sufficiently cooled between each sintering process. Δd and t have the following relationship, according to Equation 6 and the definition of Δd:

$$\Delta d = d_1 - d_N = t_N - t_1 \tag{7}$$

here, the '1' and 'N' subscripts refer to the first and last (N_{th}) sintering processes, respectively. The Δd data were smoothed using the moving average method for 20 datapoints (Figure 15). Because t_N was less than or equal to t_1, Δd was less than or equal to zero.

Assuming that no further densification occurred during the last sintering process, t_N could be considered a constant (t_f) and calculated based on the final density (ρ_f) measured using the Archimedes method. Because the mass (*m*) and basal area (A) of the specimen were known, the relative density of each specimen was calculated using Equation 8.

$$\rho = \frac{m}{\rho_{th} A} \left(\frac{1}{t_f - \Delta d} \right) \times 100 \tag{8}$$

where ρ_{th} is the theoretical density of the specimen.

The densification curves of Pure W and W-Y were fitted to a logistic function, which is a type of sigmoid function, to observe their general trends (Equation 9).

$$\rho(T) = C_1 + \frac{C_2}{1 + exp\left(-\frac{T - C_3}{C_4} \right)} \tag{9}$$

The fitting parameters for the densification curves of Pure W and W-Y are listed in Table 2.

Figure 16 shows densification curves of Pure W and W-Y, which were constructed using the data obtained from SPS. The relative density of Pure W was comparable to that of W-Y up to 1300 °C. However, the densification rate of Pure W decreased with increasing temperature, and the relative density of Pure W began to be small compared to that of W-Y approximately at 1300 °C.

To avoid obscuring the results due to experimental error, the relative density was also plotted against the sintering temperature (Figure 17 (a)). The relative density of Pure W was almost identical to that of W-Y up to ~1300 °C. However, with increasing temperature, the densification rate of Pure W decreased and its final relative density was lower than that of W-Y. This trend was corresponded with the densification curves constructed using the displacement data during SPS (Figure 16).

Kim et al. [49] suggested that the local liquefaction of Y_2O_3 could promote the densification of tungsten. The eutectic temperature of the W– Y_2O_3 system (1560 °C) increases with decreasing amount of Y_2O_3. However, in the present study, the density difference between the two specimens began to appear at temperatures lower than 1560 °C, that is, 1300–1400 °C. Therefore, the formation of the liquid phase hardly contributed to improving the sinterability of tungsten. Another possible factor that enhances sinterability is the easier movement of tungsten atoms through Y_2O_3. Based on the solubility of tungsten atoms in Y_2O_3, Kim et al. [8] suggested that Y_2O_3 can serve as a pathway for tungsten atoms during sintering through dissolution and reprecipitation, which can help increase the densification rate. However, this effect was likely hindered in the present study because of the extremely small amount of Y_2O_3 in the specimen compared to that of tungsten.

The inhibition of grain growth due to Y_2O_3 in the W-Y specimen was analyzed as a potentially major sinterability-enhancing factor. When a grain boundary migrates rapidly during sintering, pores separate from the grain boundary and become trapped in the grain; this is called pore–boundary separation [50]. Because the pores isolated in the grain can only be closed by lattice diffusion, which is a sluggish process, rapid grain growth lowers the densification rate [51]. The Figure 17 (b) indicate that the grain size of W-Y is lower than that of Pure W at temperatures above 1300 °C. This suggests that the nanosized particles formed via internal oxidation of Y effectively pinned grain boundaries, thereby hindering the pore–boundary separation. Therefore, unlike that of Pure W, the densification rate of W-Y during sintering did not decrease notably even at temperatures above 1300 °C, resulting in a high sintering density. Additionally, because the densification of the Y_2O_3-dispersion-strengthened tungsten is dominated by grain-boundary diffusion [21, 52], the higher grain-boundary fraction of W-Y powder than that of Pure W possibly contributed to the rapid densification.

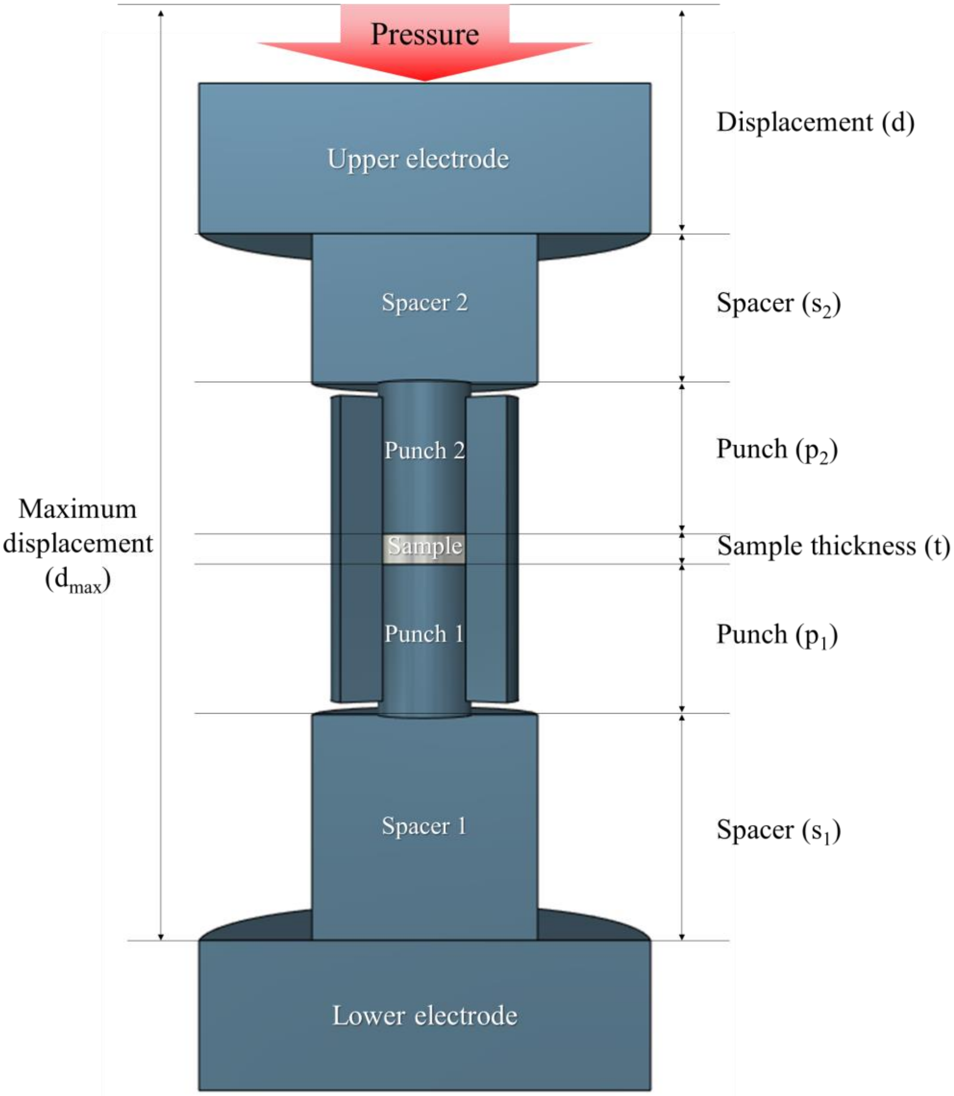

Figure 14 Schematic of test setup featuring a mold mounted on an SPS machine.

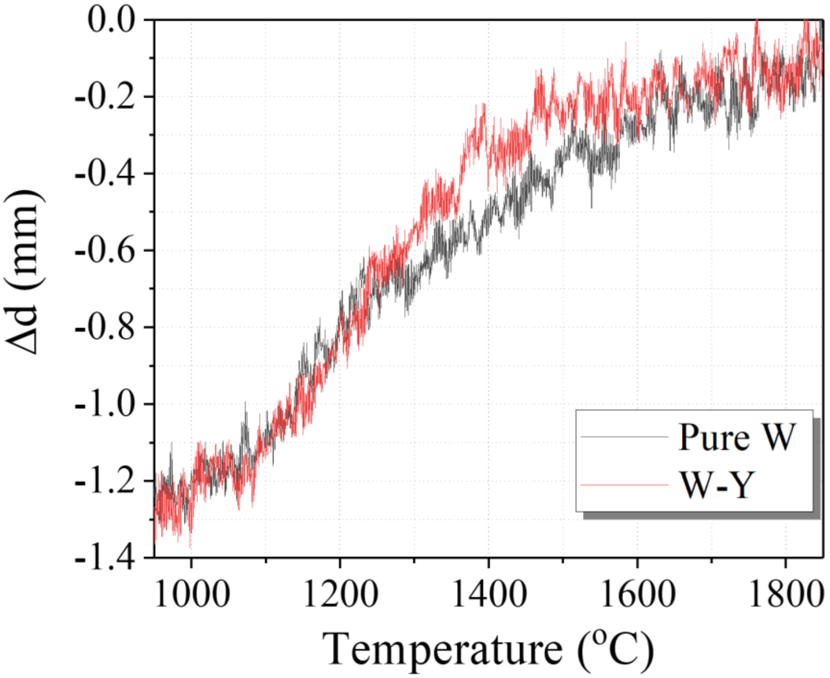

Figure 15 Temperature-related differences in displacement during SPS.

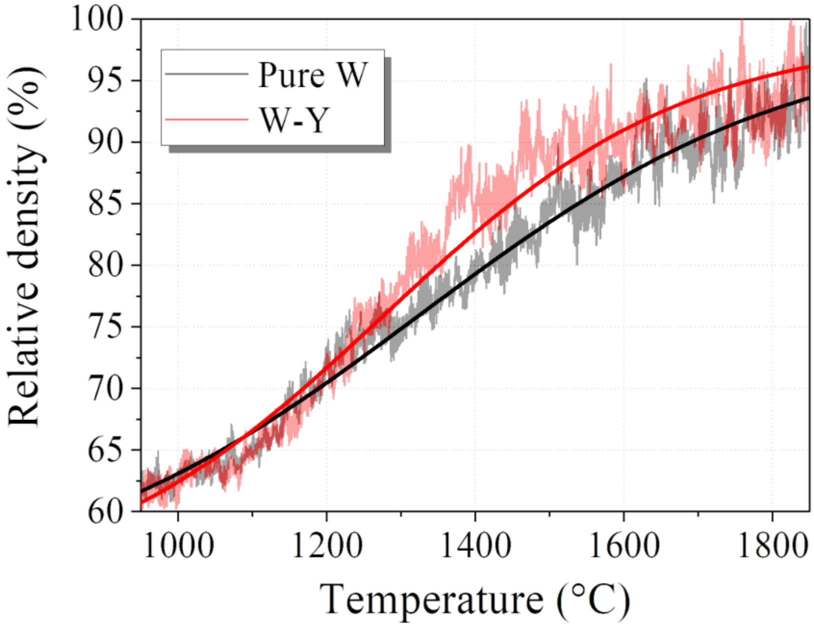

Figure 16 Relative density as a function of temperature during SPS. The solid lines were obtained by fitting the densification curves to the sigmoid function.

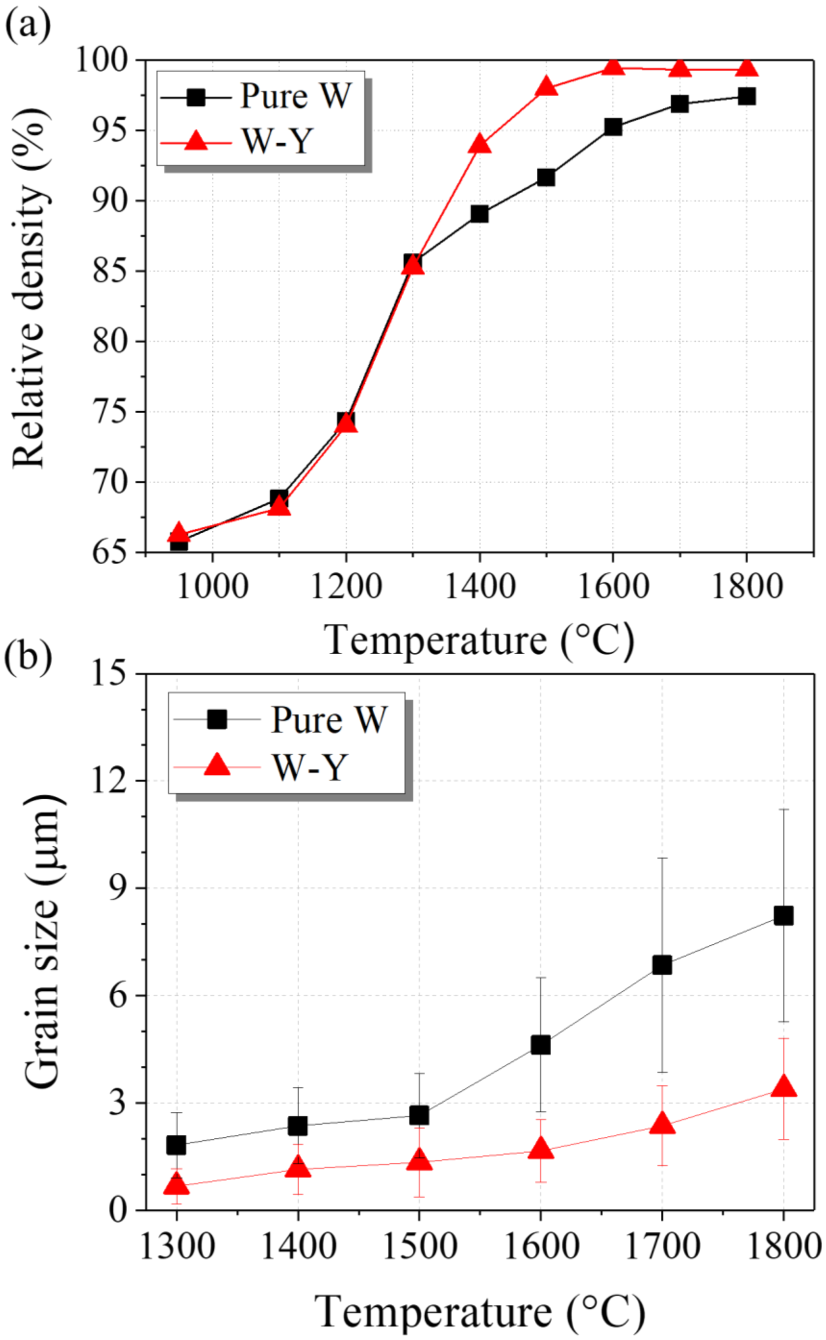

Figure 17 (a) Densification curves of Pure W and W-Y powders. (b) Average grain sizes of Pure W and W-Y.

Table 2 Measured densities and fitting parameters for nonlinear regression of densification data.

	Measured density (ρ_f, g/cm^3)	Thickness of specimen (t_f, cm)	Fitting parameters $\rho(T) = C_1 + C_2/[1 + exp(-(T - C_3)/C_4)]$			
	ρ_f	t_f	C_1	C_2	C_3	C_4
Pure W	18.99	0.2095	53.20	45.47	1324.41	253.445
W-Y	19.02	0.2092	53.37	45.57	1275.84	203.146

2.3.4 Effect of yttrium-doping on plasma-facing properties of tungsten

In plasma-facing environments, materials are exposed to high temperatures and high particle fluxes, which lead to microstructural and mechanical property degradation. Thus, to evaluate the thermal stability of the SPSed Pure W, SPSed W-Y, and commercially obtained pure tungsten, each specimen was heated to high temperatures and its microstructure was investigated by EBSD analysis.

Figures 18 (a and b) indicate that the microstructures of the SPSed specimens hardly change upon heating. The average grain sizes of the Pure W and W-Y specimens heated to 1700 °C were 17.85 ± 7.31 and 1.81 ± 1.2 μm, respectively, which were not significantly different from those of the as-sintered specimens (Table 1). The microstructure of Pure W remained relatively stable because of the scarcity of dislocations that drove recrystallization. Moreover, grain growth was hardly observed in W-Y after heating to 1700 °C, despite its higher dislocation density and smaller grain size than those of Pure W. This was primarily because of the effective inhibition of grain growth by the Y_2O_3 located at grain boundaries. Grains in the as-received commercially obtained pure tungsten were elongated in the transverse direction (TD) by hot-rolling, and the average aspect ratio was determined to be 0.2 (Figure 18 (c)). The KAM and grain-boundary maps (Figure 19) showed that the as-received commercially obtained pure tungsten had a higher dislocation density than those of SPSed Pure W and W-Y. The microstructural change of the commercial specimen was somewhat stable up to 1000 °C; however, polygonal grains were formed via recrystallization at temperatures above 1300 °C. Based on this microstructural variation, the recrystallization temperature of the commercially derived pure tungsten was estimated to be 1000–1300 °C, which is consistent with the literature [53, 54]. The commercially sourced pure tungsten exhibited a fully recrystallized microstructure upon heating to 1700 °C.

Figure 20 shows the temperature-induced changes in hardness of the tungsten specimens. The hardness of the commercially obtained pure tungsten at room temperature (472.83 ± 7.39 HV_3) was higher than that of Pure W; however, the hardness decreased at 1300 °C and became similar to that of SPSed Pure W at

1700 °C, indicating that increase in hardness by hot-rolling likely disappeared via recrystallization. In contrast, the hardness of W-Y only slightly decreased upon heating and was considerably higher than those of Pure W and the commercial sample at all temperatures. This was due to the relatively preserved microstructure of the W-Y specimens upon heating.

When tungsten is irradiated with deuterium ions, dome-shaped defects can be formed on its surface [55-57]. These defects, known as blisters, are associated with cavities that are formed under the pressure generated by deuterium bubbles collected at defects near the surface [58, 59]. Because the formed blisters degrade the thermal and mechanical properties of tungsten [60], the resistance to deuterium ions must be evaluated to utilize tungsten as a plasma-facing material. Figure 21 shows the microstructural changes in Pure W, W-Y, and the commercially obtained pure tungsten before and after the deuterium irradiation. In the Pure W and commercial tungsten specimens, the blisters were mainly dome-shaped, with some of them being ruptured under the pressure of deuterium. The average size of the blisters in the Pure W and commercial tungsten samples were 1.02 and 0.71 μm, respectively. However, the blisters in W-Y were mostly spherical and had an average size of 0.12 μm, which indicated that they were significantly smaller than those in the Pure W and commercial tungsten specimens. Additionally, the estimated number density of blisters in W-Y (2.79×10^4 mm^{-2}) was lower than those in Pure W (8.13×10^4 mm^{-2}) and commercially obtained pure tungsten (5.26×10^4 mm^{-2}). Blistering is related to the dislocation density, grain size, and precipitates in the material [61]. These defects act as nucleation sites for blisters, preventing deuterium from gathering at specific points and inhibiting the nucleation and growth of blisters [14, 62]. Because the commercial tungsten had a higher dislocation density than that of Pure W, the dislocations likely acted as nucleation sites and helped reduce the number and size of blisters. Meanwhile, the W-Y specimen had the smallest grain size among the specimens and contained numerous nanosized Y_2O_3 particles. Since hydrogen is highly reactive with oxygen, these particles could allow deuterium to remain in the material by trapping. Therefore, the abundant nucleation sites presumably contributed to reducing the number and size of blisters.

In the operational environment of a fusion reactor, deuterium and tritium, the reactants of nuclear fusion reactions, can become embedded and retained in plasma-facing materials. Because the density of the reactant plasma ions is closely related to the stability and efficiency of the fusion reaction, it is important to evaluate the amount of deuterium retention in the specimens. To achieve this objective, TDS experiments were conducted. Figure 22 presents the results of the TDS analysis performed on SPSed Pure W, SPSed W-Y, and commercially obtained pure tungsten specimen. The SPSed Pure W specimen exhibits the lowest amount of deuterium retention, which can be attributed to its high purity and small number of defects which serve as trapping sites for deuterium. After the addition of Y_2O_3, the retention rate of deuterium increases due to the increased number of trapping sites such as Y_2O_3 precipitates and grain boundaries. However, the deuterium retention in the W-Y specimen does not exceed that of the commercially obtained pure tungsten specimen. It can be attributed that the commercially obtained pure tungsten contains the high dislocation density which functions as the trapping site of deuterium due to thermo-mechanical processing.

Figure 23 illustrates the microstructural changes in SPSed Pure W, SPSed W-Y, and commercially obtained pure tungsten specimens before and after helium irradiation. The presence of a fuzz structure, resulting from He+ ion bombardment, is clearly observed in all specimens. The cross-sectional image of the commercially available pure tungsten specimen reveals a fuzz depth of approximately 1.2 μm. In contrast, the SPSed Pure W and SPSed W-Y specimens exhibit fuzz structures with shallower depths of 0.35 μm and 0.25 μm, respectively. Furthermore, the width of the fuzz structure in the SPSed specimens is significantly narrower compared to that in the commercially obtained pure tungsten. It is known that the formation of fuzz alters the erosion rate and can contribute to the embrittlement of the divertor and result in the release of tungsten, along with helium bubbles containing trapped tritium, into the plasma within the reactor. From this perspective, it can be concluded that the W-Y specimen exhibits the most optimal resistance to He^+ ion irradiation among the tested specimens in this chapter.

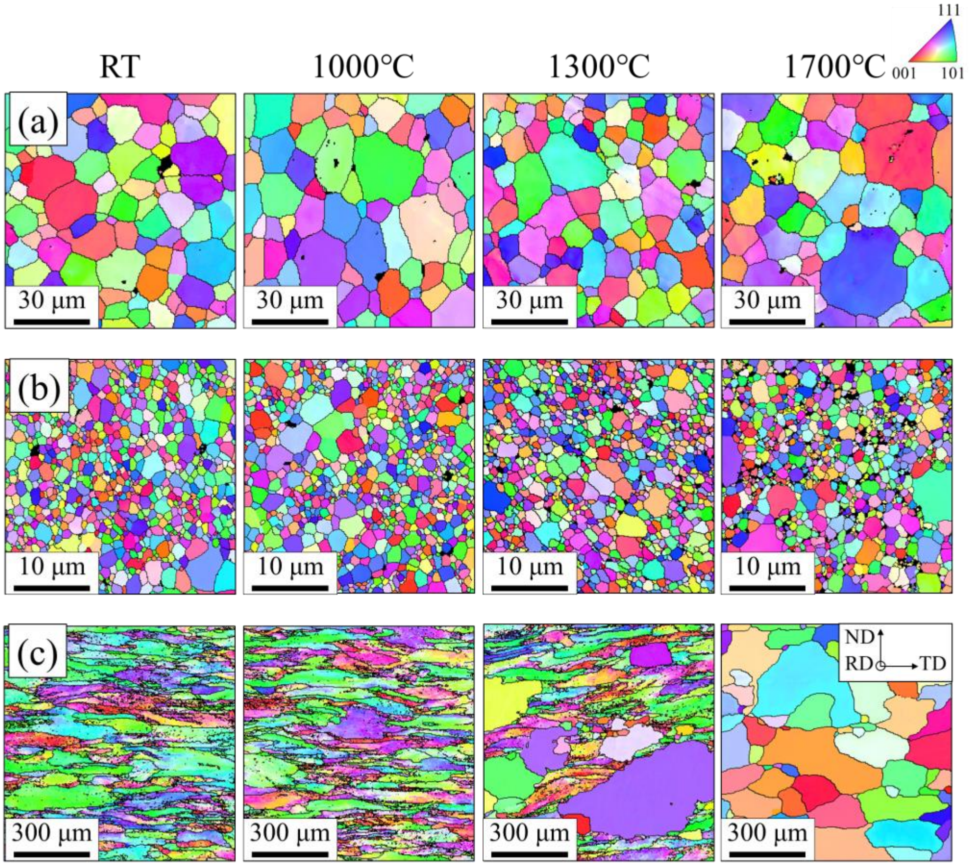

Figure 18 Microstructural changes in tungsten specimens with annealing temperature: (a) Pure W, (b) W-Y, (c) commercially obtained pure tungsten.

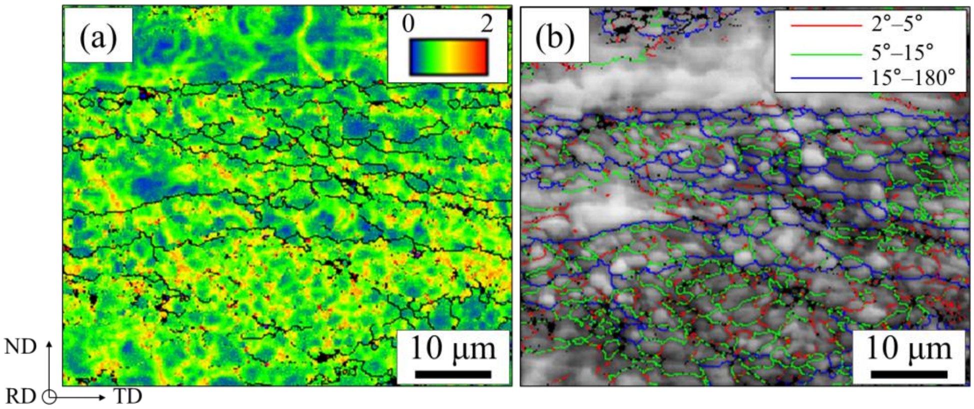

Figure 19 EBSD analysis conducted along the RD surface of as-received commercially obtained pure tungsten at room temperature. (a) KAM and (b) grain-boundary maps. The grain boundaries (black lines) in (a) were drawn based on a misorientation angle of 15°.

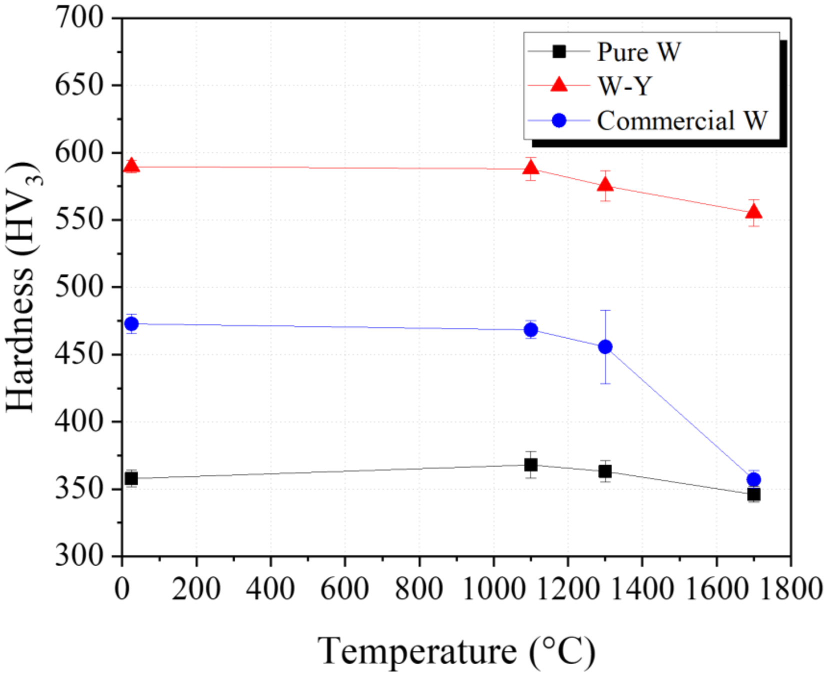

Figure 20 Hardness of (a) Pure W, (b) W-Y, and (c) commercially obtained pure tungsten after annealing at various temperatures.

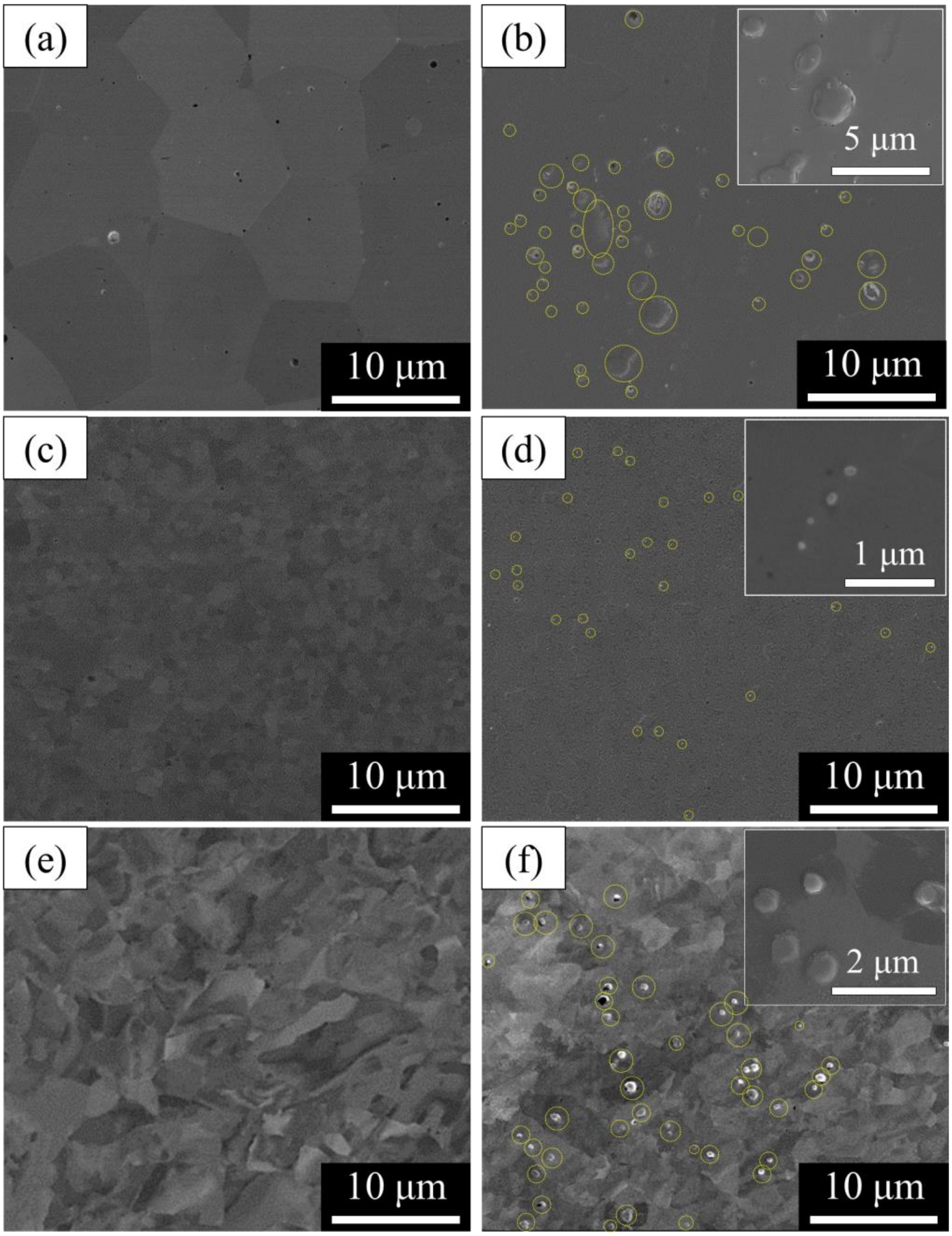

Figure 21 Surface morphologies of (a, b) Pure W, (c, d) W-Y, and (e, f) commercially obtained tungsten specimens (a, c, e) before and (b, d, f) after deuterium irradiation.

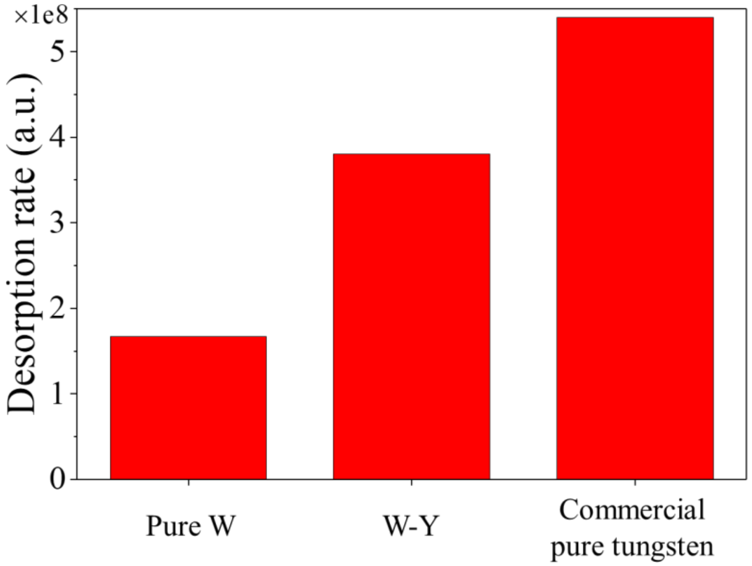

Figure 22 TDS results of Pure W, W-Y, and commercially obtained tungsten specimens.

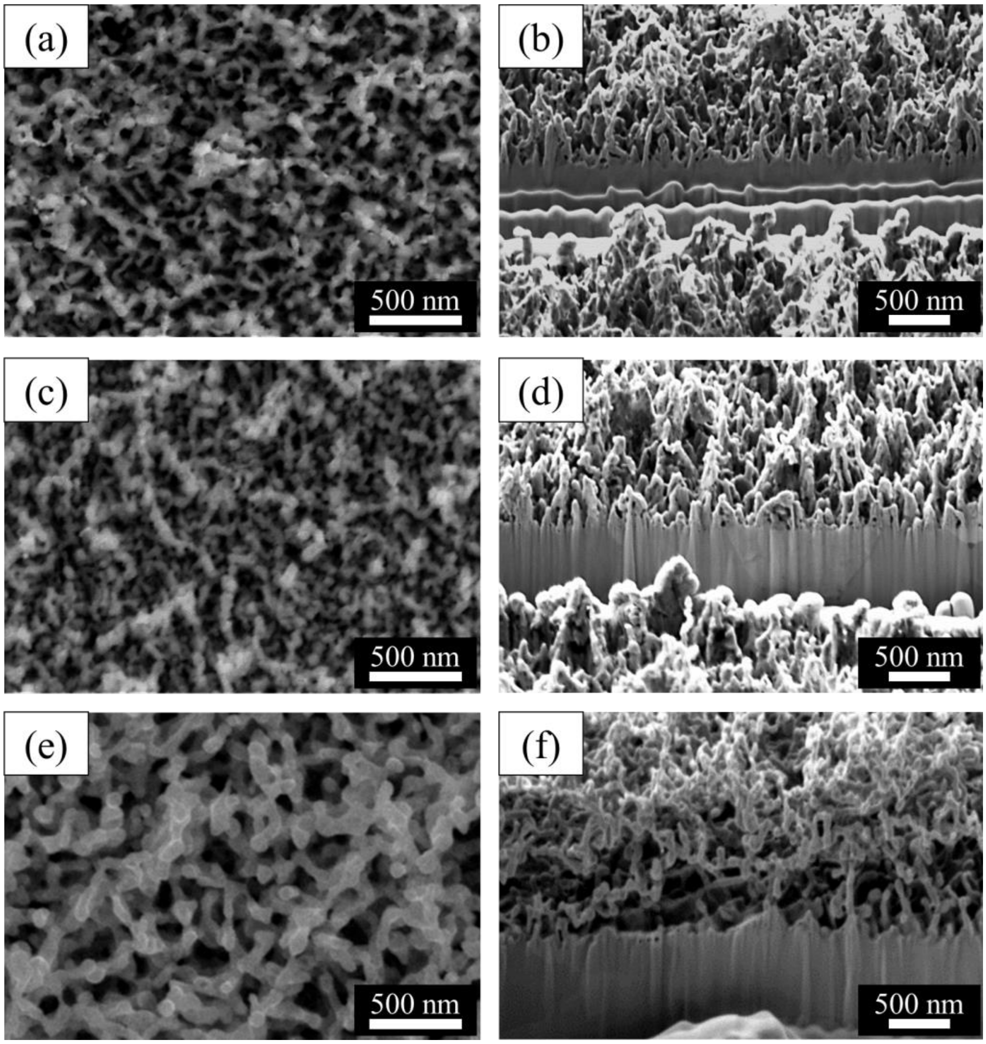

Figure 23 SEM images after He^+ irradiation on SPSed Pure W, SPSed W-Y and commercially obtained pure tungsten; (a, b) incident surface and cross-section of SPSed Pure W, (c, d) incident surface and cross-section of SPSed W-Y, and (e, f) incident surface and cross-section of commercially obtained tungsten specimens.

2.3.5 Effect of yttrium-doping on microscopic mechanical behavior of tungsten

Nanoindentation tests are suitable for evaluating the local plasticity of a material owing to its small activation volume [63]. Therefore, nanoindentation tests were performed on the Pure W, W-Y, and commercial tungsten specimens to investigate their mechanical properties by excluding the influence of grain boundaries. The maximum shear stress for inducing plastic yield can be calculated based on the “pop-in” phenomenon, which is a sudden burst of displacement at the same load during an indentation test [64-66].

The load–displacement (*P–h*) curves for the Pure W, W-Y, and commercial specimens are shown in Figure 24. The purple dotted lines were obtained by fitting the elastic region of the *P–h* curve to the Hertzian-elastic-contact equation. The theoretical equation for elastic deformation induced by a spherical indenter is expressed as follows [67]:

$$P = \frac{4}{3} E_r \sqrt{R_i h^3} \tag{10}$$

where P is the load imposed by the spherical indenter, h is the indentation depth, R_i is the effective indenter tip radius, and E_r is the reduced elastic modulus. The R_i value measured from standard quartz specimen was 316.57 nm. The E_r values obtained by fitting the elastic region of *P-h* curve of the Pure W, W-Y, and commercial specimens to Hertzian curves were 316.86, 318.07, and 328.90 GPa, respectively. Assuming isotropic elasticity, the reduced elastic modulus of a material can be calculated as follows [68]:

$$E_r = \left(\frac{1 - \nu^2}{E} + \frac{1 - \nu_i^2}{E_i} \right)^{-1} \tag{11}$$

where E and E_i are the elastic moduli of tungsten (410 GPa) and the diamond indenter tip (1141 GPa), respectively, and ν and ν_i are the Poisson ratios of tungsten (0.28) and the diamond indenter tip (0.07), respectively [68]. The E_r calculated using these values (320.52 GPa) is similar to that obtained by fitting.

Figure 24 shows a sudden increase in displacement at a constant load. The maximum shear stress (τ_m) for yielding can be calculated using the Hertzian elastic solution at the pop-in load (P_p) [67].

$$\tau_m = 0.31\left(\frac{6P_pE_r^2}{\pi^3R_i^2}\right)^{1/3} \tag{12}$$

Figure 25 shows the maximum shear stresses of the Pure W, W-Y, and commercial tungsten samples as histograms; the corresponding cumulative probability distributions of maximum shear stress are available in Figure 26. The solid lines shown in the figures were obtained by fitting the histograms to a log-normal distribution function for statistical analysis. The maximum shear stresses for Pure W and commercially obtained pure tungsten were determined using one probability distribution (P1 and P4, respectively), whereas that for W-Y was obtained as a combination of two probability distributions (P2 and P3). The average values of P1 and P2 were 19.43 and 19.72 GPa, respectively, which are close to the theoretical strength of pure tungsten (~25 GPa [69]). Because Pure W and W-Y had relatively low dislocation densities, the dislocations were likely not present directly below the indenter tip. Thus, dislocations had to have been formed prior to their movement to ensure plastic deformation, which resulted in the measured maximum shear stress being close to the theoretical strength. Unlike Pure W, W-Y exhibited an additional probability distribution (P3) with an average value of 15.17 GPa, which is comparable to the average maximum shear stress (P4) for the commercially obtained pure tungsten (13.05 GPa). These two average values are closer to the Peierls–Nabarro stress (7.28 GPa [63]) in the {211}<111> slip system than the theoretical strength of tungsten; the former represents stress that enables preexisting dislocations to glide. This indicates that Y_2O_3 doping can contribute to the low local yield strength of tungsten by introducing dislocations.

Figure 27 shows cumulative probability distributions of nanohardness for the Pure W, W-Y, and commercially sourced pure tungsten specimens; the corresponding histograms of nanohardness are present in Figure 28. The average nanohardness of the commercial sample (7.96 ± 0.35 GPa) was higher than that of Pure W (7.32 ±

0.22 GPa) owing to the dislocation-induced strengthening. The nanohardness of the W-Y specimen is related to the distribution of nanosized Y_2O_3 in grains. Based on the average size and number density of Y_2O_3, the average distance between Y_2O_3 particles was calculated to be ~158 nm, which is on the same order of magnitude as the effective radius of the indenter tip (316 nm). Therefore, during the nanoindentation tests, Y_2O_3 particles were likely absent from the activation volume. Because the dislocation density of W-Y was between those of Pure W and the commercial specimen, the nanohardness of W-Y had to be between those of Pure W and the commercial sample if Y_2O_3 particles were not present under the indenter tip. However, when one or more Y_2O_3 particles were present in the activation volume, W-Y exhibited a considerably higher nanohardness than in the absence of Y_2O_3 owing to the precipitation strengthening effect. This is consistent with the trends shown in Figure 27.

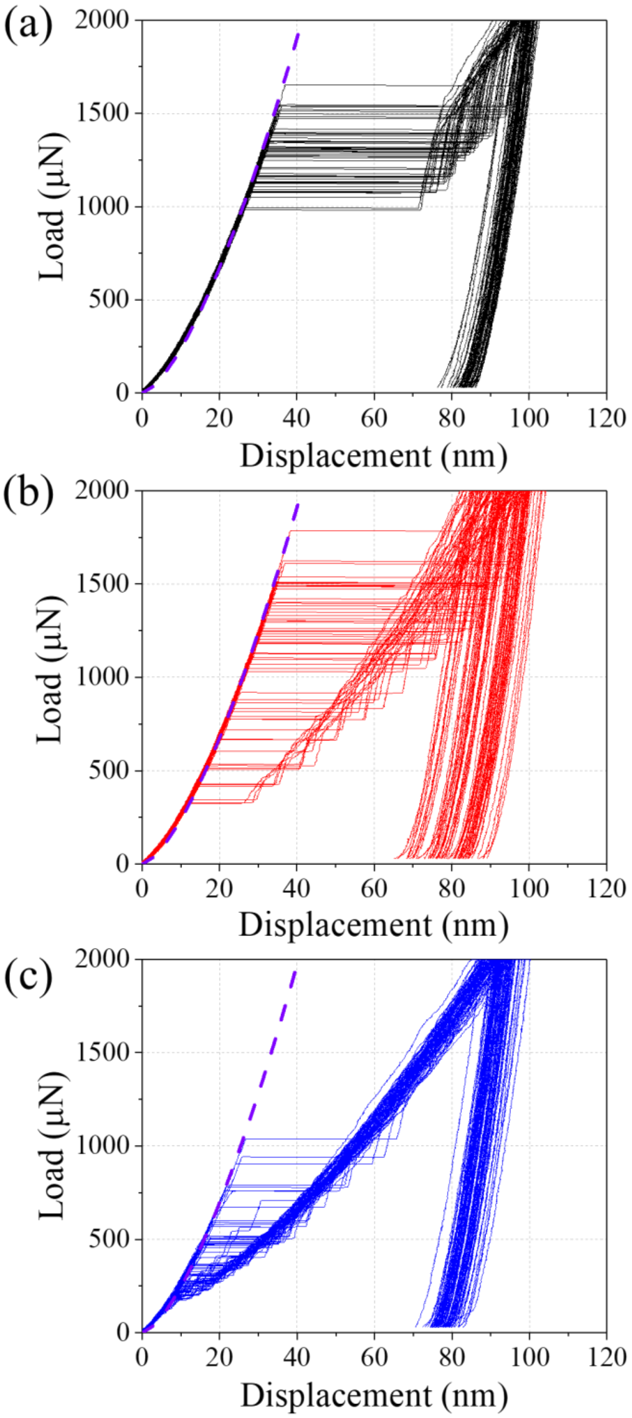

Figure 24 Load–displacement curves of (a) Pure W, (b) W-Y, and (c) commercially obtained pure tungsten acquired during nanoindentation tests. The purple dotted lines were obtained by fitting the elastic deformation region to the Hertzian curve.

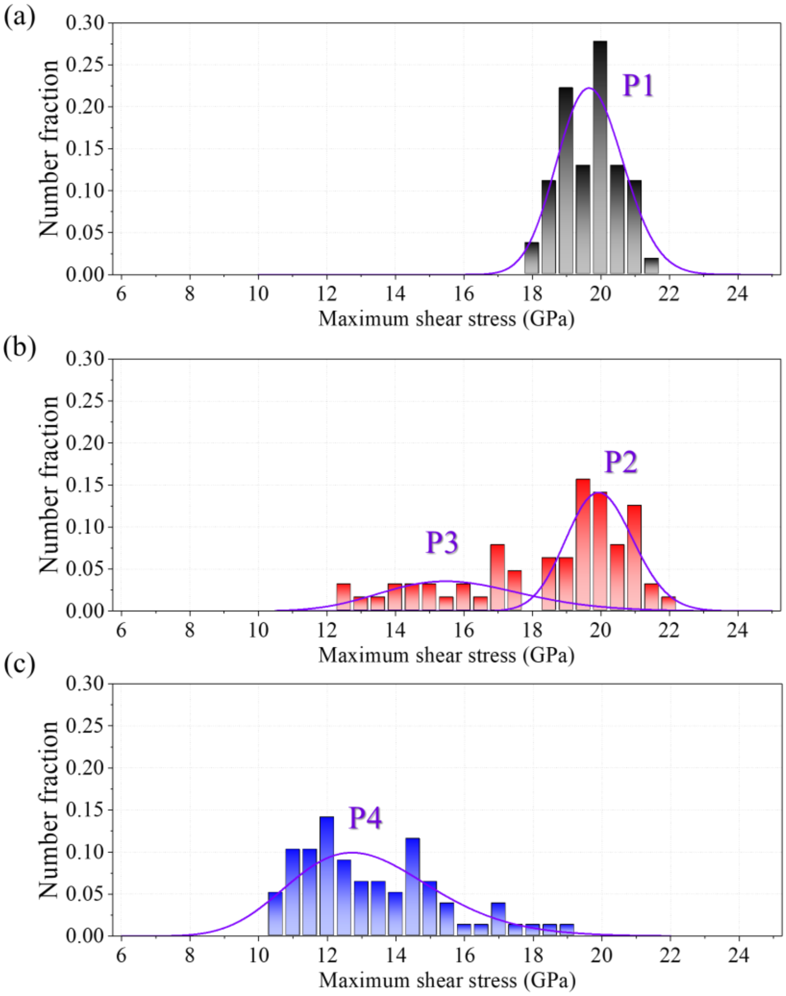

Figure 25 Maximum shear stress for yielding in (a) Pure W, (b) W-Y, and (c) commercially obtained pure tungsten. The purple lines (P1, P2, P3, and P4) were obtained by fitting the histograms to a log-normal distribution.

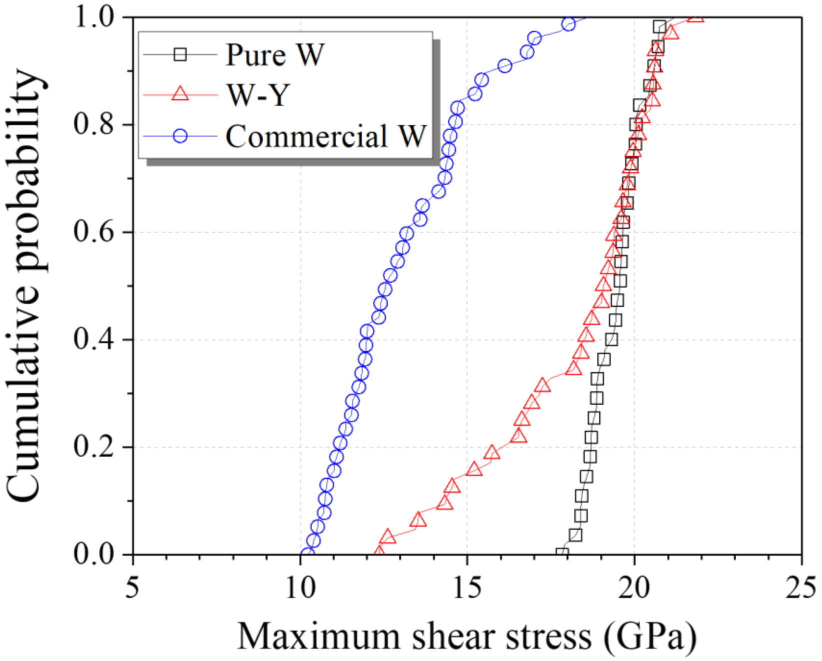

Figure 26 Cumulative probability distribution of maximum shear stress for yielding in Pure W, W-Y and commercially obtained pure tungsten; The raw data are consistent with Fig. 9 in the manuscript.

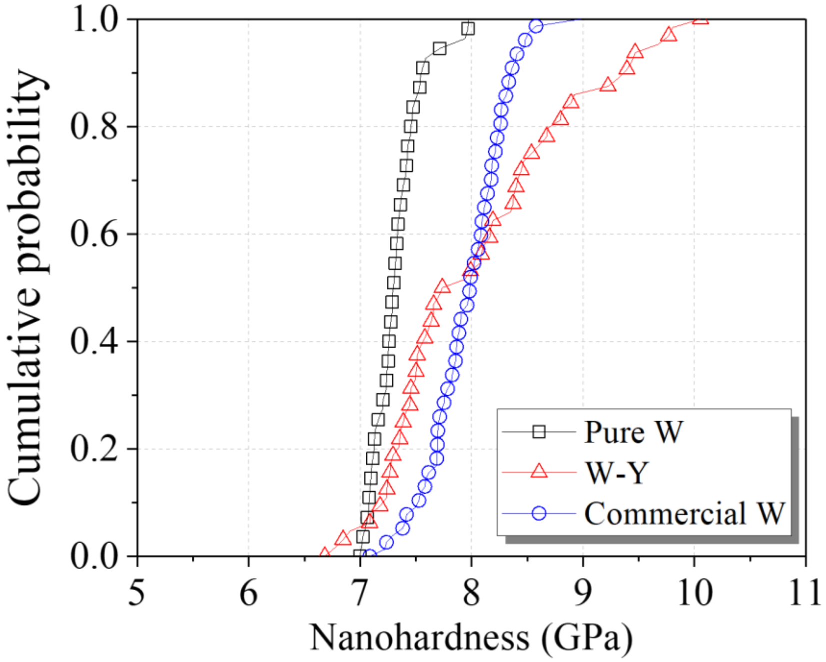

Figure 27 Cumulative probability distributions of nanohardness for Pure W, W-Y, and commercially obtained pure tungsten.

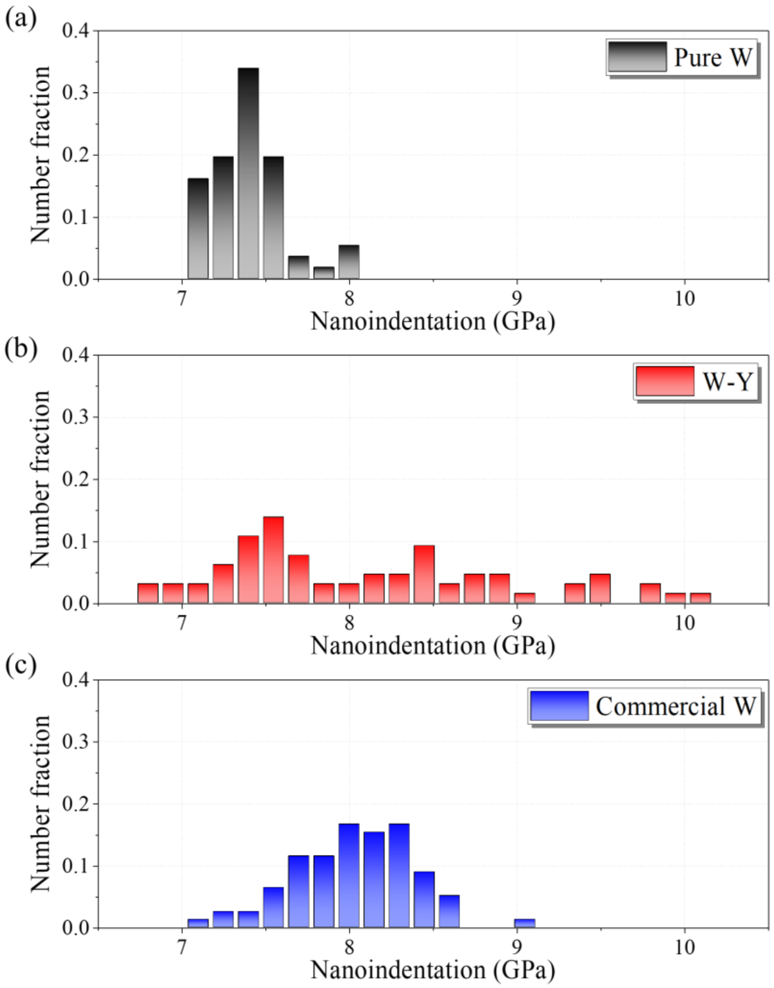

Figure 28 Nanohardness in (a) Pure W, (b) W-Y, and (c) commercially obtained pure tungsten; The raw data are consistent with Fig. 10 in the manuscript.

2.4. Conclusions

In this study, Y-doped tungsten was prepared via internal oxidation during SPS, and its microstructure, plasma-facing properties, and intrinsic mechanical characteristics were compared with those of SPSed Pure W and commercially obtained pure tungsten. Consequently, the following conclusions were obtained:

(1) W-Y had a higher relative density and hardness and a smaller grain size than those of Pure W sintered at higher temperatures. Additionally, spherical Y_2O_3 particles with an average size of 20 nm were distributed in the W-Y specimen, according to TEM and SANS analyses.

(2) The relative density of tungsten was increased using mechanically alloyed Y-doped tungsten powder. This is because the Y_2O_3 formed during the process pinned the grain boundaries, preventing their pores from being isolated in the grains, and the high grain-boundary fraction promoted grain-boundary diffusion, which is the predominant material-transport mechanism for densification of tungsten.

(3) A comparison of the microstructures and hardness values of Pure W, W-Y, and commercially obtained pure tungsten specimens annealed at various temperatures revealed that W-Y maintained its fine microstructure and high hardness even at 1700 °C. This resulted from the pinning effect of nanosized Y_2O_3 particles.

(4) After deuterium irradiation, fewer and smaller blisters were formed in W-Y compared to those in Pure W and commercially obtained pure tungsten. This was likely because numerous defects including oxides and grain boundaries acted as nucleation sites for blisters, preventing deuterium from accumulating at specific positions. In addition, after helium irradiation, the is most shallow depth of fuzz structure was observed in the W-Y specimen.

(5) Nanoindentation experiments revealed that the nanosized Y_2O_3 present in W-Y introduced dislocations to the specimen and lowered the maximum shear stress for yielding in a localized region. Additionally, the nanosized Y_2O_3 helped increase the nanohardness via precipitation strengthening.

2.5. References

[1] X.Y. Ding, L.M. Luo, H.Y. Chen, X.Y. Zhu, X. Zan, J.G. Cheng, Y.C. Wu, Chemical Synthesis and Oxide Dispersion Properties of Strengthened Tungsten via Spark Plasma Sintering, Materials (Basel) 9(11) (2016) 879.

[2] R. Wang, Z.M. Xie, Y.K. Wang, J.P. Song, Q.F. Fang, R. Liu, Y. Jiang, J.F. Yang, T. Zhang, X.P. Wang, C.S. Liu, Fabrication and characterization of nanocrystalline ODS-W via a dissolution-precipitation process, International Journal of Refractory Metals and Hard Materials 80 (2019) 104-113.

[3] R. Liu, Z.M. Xie, J.F. Yang, T. Zhang, T. Hao, X.P. Wang, Q.F. Fang, C.S. Liu, Recent progress on the R&D of W-ZrC alloys for plasma facing components in fusion devices, Nuclear Materials and Energy 16 (2018) 191-206.

[4] E.S. Lee, G. Lee, Y.-I. Lee, Y.-K. Jeong, S.-T. Oh, Fabrication of $W-Y_2O_3-La_2O_3$ composite by chemical process and spark plasma sintering, Powder Metallurgy 64(2) (2021) 108-114.

[5] H. Jia, Z. Zhou, S. Li, A new strategy for additive manufacturing ODS steel using Y-containing gas atomized powder, Materials Characterization 187 (2022).

[6] E. Simondon, P.F. Giroux, J. Ribis, G. Spartacus, L. Chaffron, T. Gloriant, Innovative method of ODS steels manufacturing by direct introduction of pyrochlore phase through milling, Materials Characterization 181 (2021).

[7] C. Suryanarayana, A.A. Al-Joubori, Z. Wang, Nanostructured Materials and Nanocomposites by Mechanical Alloying: An Overview, Metals and Materials International 28(1) (2021) 41-53.

[8] Y. Kim, K.H. Lee, E.-P. Kim, D.-I. Cheong, S.H. Hong, Fabrication of high temperature oxides dispersion strengthened tungsten composites by spark plasma sintering process, International Journal of Refractory Metals and Hard Materials 27(5) (2009) 842-846.

[9] L. Veleva, Z. Oksiuta, U. Vogt, N. Baluc, Sintering and characterization of W−Y and $W-Y_2O_3$ materials, Fusion Engineering and Design 84(7-11) (2009) 1920-1924.

[10] F. Xiao, Q. Miao, S. Wei, Z. Li, T. Sun, L. Xu, Microstructure and mechanical properties of W-ZrO2 alloys by different preparation techniques, Journal of Alloys and Compounds 774 (2019) 210-221.

[11] J.W. Coenen, S. Antusch, M. Aumann, W. Biel, J. Du, J. Engels, S. Heuer, A. Houben, T. Hoeschen, B. Jasper, F. Koch, J. Linke, A. Litnovsky, Y. Mao, R. Neu, G. Pintsuk, J. Riesch, M. Rasinski, J. Reiser, M. Rieth, A. Terra, B. Unterberg, T. Weber, T. Wegener, J.H. You, C. Linsmeier, Materials for DEMO and reactor applications-boundary conditions and new concepts, Physica Scripta T167 (2016).

[12] Y. Lv, Y. Han, S. Zhao, Z. Du, J. Fan, Nano-in-situ-composite ultrafine-grained $W-Y_2O_3$ materials: Microstructure, mechanical properties and high heat load performances, Journal of Alloys and Compounds 855 (2021).

[13] Z. Dong, N. Liu, Z. Ma, C. Liu, Q. Guo, Y. Liu, Preparation of ultra-fine grain W-Y_2O_3 alloy by an improved wet chemical method and two-step spark plasma sintering, Journal of Alloys and Compounds 695 (2017) 2969-2973.

[14] S. Wurster, R. Pippan, Nanostructured metals under irradiation, Scripta Materialia 60(12) (2009) 1083-1087.

[15] W. Hu, Q. Ma, Z. Ma, Y. Huang, Z. Wang, Y. Liu, Ultra-fine W−Y_2O_3 composite powders prepared by an improved chemical co-precipitation method and its interface structure after spark plasma sintering, Tungsten 1(3) (2019) 220-228.

[16] Y. Itoh, Y. Ishiwata, Strength properties of yttrium-oxide-dispersed tungsten alloy, Jsme Int J a-Mech M 39(3) (1996) 429-434.

[17] S.C. Cifuentes, A. Muñoz, M.A. Monge, P. Pérez, Influence of processing route and yttria additions on the oxidation behavior of tungsten, Journal of Nuclear Materials 442(1-3) (2013) S214-S218.

[18] M. Battabyal, P. Spätig, B.S. Murty, N. Baluc, Investigation of microstructure and microhardness of pure W and W-2Y_2O_3 materials before and after ion-irradiation, International Journal of Refractory Metals and Hard Materials 46 (2014) 168-172.

[19] R. Liu, Z.M. Xie, Q.F. Fang, T. Zhang, X.P. Wang, T. Hao, C.S. Liu, Y. Dai, Nanostructured yttria dispersion-strengthened tungsten synthesized by sol−gel method, Journal of Alloys and Compounds 657 (2016) 73-80.

[20] M. Zhao, Z. Zhou, M. Zhong, J. Tan, Y. Lian, X. Liu, Thermal shock behavior of fine grained W−Y_2O_3 materials fabricated via two different manufacturing technologies, Journal of Nuclear Materials 479 (2016) 236-243.

[21] Z. Dong, N. Liu, W. Hu, X. Kong, Z. Ma, Y. Liu, The effect of Y_2O_3 on the grain growth and densification of W matrix during low temperature sintering: Experiments and modelling, Materials & Design 181 (2019).

[22] M. Zhao, Z. Zhou, J. Tan, Q. Ding, M. Zhong, Effects of ball milling parameters on microstructural evolution and mechanical properties of W-3%Y composites, Journal of Nuclear Materials 465 (2015) 6-12.

[23] M. Zhao, Z. Zhou, Q. Ding, M. Zhong, K. Arshad, Effect of rare earth elements on the consolidation behavior and microstructure of tungsten alloys, International Journal of Refractory Metals and Hard Materials 48 (2015) 19-23.

[24] T. Hirai, V. Barabash, F. Escourbiac, A. Durocher, L. Ferrand, V. Komarov, M. Merola, ITER divertor materials and manufacturing challenges, Fusion Engineering and Design 125 (2017) 250-255.

[25] J. Choi, H.-M. Sung, K.-B. Roh, S.-H. Hong, G.-H. Kim, H.N. Han, Fabrication of sintered tungsten by spark plasma sintering and investigation of thermal stability, International Journal of Refractory Metals and Hard Materials 69 (2017) 164-169.

[26] S.-R. Huh, N.-K. Kim, B.-K. Jung, K.-J. Chung, Y.-S. Hwang, G.-H. Kim, Global model analysis of negative ion generation in low-pressure inductively coupled hydrogen plasmas with bi-Maxwellian electron energy distributions,

Physics of Plasmas 22(3) (2015).

[27] P.A. Redhead, Thermal desorption of gases, Vacuum 12(4) (1962) 203-211.

[28] M.J. Baldwin, R. Dejarnac, M. Komm, R.P. Doerner, Fuzz growth in the gaps of castellated W in PISCES-A: experiment and modeling, Plasma Physics and Controlled Fusion 59(6) (2017).

[29] S. Kajita, N. Yoshida, N. Ohno, Tungsten fuzz: Deposition effects and influence to fusion devices, Nuclear Materials and Energy 25 (2020).

[30] P. Debye, P. Scherrer, Interference of irregularly oriented particles in X-rays, Phys. Zeit 17 (1916) 277-283.

[31] P. Scherrer, Nachr Ges wiss goettingen, Math. Phys. 2 (1918) 98-100.

[32] M.A. Yar, S. Wahlberg, H. Bergqvis, H.G. Salem, M. Johnsson, M. Muhammed, Chemically produced nanostructured ODS-lanthanum oxide-tungsten composites sintered by spark plasma, Journal of Nuclear Materials 408(2) (2011) 129-135.

[33] B. Gludovatz, S. Wurster, A. Hoffmann, R. Pippan, Fracture toughness of polycrystalline tungsten alloys, International Journal of Refractory Metals and Hard Materials 28(6) (2010) 674-678.

[34] B. Gludovatz, S. Wurster, T. Weingärtner, A. Hoffmann, R. Pippan, Influence of impurities on the fracture behaviour of tungsten, Philosophical Magazine 91(22) (2011) 3006-3020.

[35] H.J. Borchardt, Yittrum-Tungsten Oxides, Inorganic chemistry 2(1) (1962) 170-173.

[36] L. Veleva, R. Schaeublin, M. Battabyal, T. Plociski, N. Baluc, Investigation of microstructure and mechanical properties of W−Y and W−Y_2O_3 materials fabricated by powder metallurgy method, International Journal of Refractory Metals and Hard Materials 50 (2015) 210-216.

[37] W. Hu, Z. Dong, Z. Ma, Y. Liu, W−Y_2O_3 composite nanopowders prepared by hydrothermal synthesis method: Co-deposition mechanism and low temperature sintering characteristics, Journal of Alloys and Compounds 821 (2020).

[38] Z. Dong, Z. Ma, J. Dong, C. Li, L. Yu, C. Liu, Y. Liu, The simultaneous improvements of strength and ductility in W−Y_2O_3 alloy obtained via an alkaline hydrothermal method and subsequent low temperature sintering, Materials Science and Engineering: A 784 (2020).

[39] W. Hu, Z. Dong, L. Yu, Z. Ma, Y. Liu, Synthesis of W-Y_2O_3 alloys by freeze-drying and subsequent low temperature sintering: Microstructure refinement and second phase particles regulation, Journal of Materials Science & Technology 36 (2020) 84-90.

[40] W. Hu, L. Yu, Z. Ma, Y. Liu, W-Y_2O_3 composite nanopowders prepared by freeze-drying method and its sintering characteristics, Journal of Alloys and Compounds 806 (2019) 127-135.

[41] Z. Dong, N. Liu, Z. Ma, C. Liu, Q. Guo, Y. Yamauchi, H.R. Alamri, Z.A. Alothman, M. Shahriar A. Hossain, Y. Liu, Synthesis of nanosized composite powders via a wet chemical process for sintering high performance W-Y_2O_3 alloy, International Journal of Refractory Metals and Hard Materials 69 (2017) 266-272.

[42] G. Beaucage, H.K. Kammler, S.E. Pratsinis, Particle size distributions from small-angle scattering using global scattering functions, Journal of Applied Crystallography 37(4) (2004) 523-535.

[43] U. Keiderling, A. Wiedenmann, V. Srdic, M. Winterer, H. Hahn, Nano-sized ceramics of coated alumina and zirconia analyzed with SANS, Journal of Applied Crystallography 33(1) (2000) 483-487.

[44] M. Rogante, V.T. Lebedev, F. Nicolaie, E. Rétfalvi, L. Rosta, SANS study of the precipitates microstructural evolution in Al 4032 car engine pistons, Physica B: Condensed Matter 358(1-4) (2005) 224-231.

[45] G. Spartacus, J. Malaplate, F. De Geuser, D. Sornin, A. Gangloff, R. Guillou, A. Deschamps, Nano-oxide precipitation kinetics during the consolidation process of a ferritic oxide dispersion strengthened steel, Scripta Materialia 188 (2020) 10-15.

[46] S. Wahlberg, M.A. Yar, M.O. Abuelnaga, H.G. Salem, M. Johnsson, M. Muhammed, Fabrication of nanostructured W-Y_2O_3 materials by chemical methods, Journal of Materials Chemistry 22(25) (2012) 12622-12628.

[47] M.A. Yar, S. Wahlberg, M.O. Abuelnaga, M. Johnsson, M. Muhammed, Processing and sintering of yttrium-doped tungsten oxide nanopowders to tungsten-based composites, Journal of Materials Science 49(16) (2014) 5703-5713.

[48] Z. Dong, N. Liu, Z. Ma, C. Liu, Q. Guo, Z.A. Alothman, Y. Yamauchi, A.H.M. Shahriar, Y. Liu, Microstructure Refinement in W-Y_2O_3 Alloy Fabricated by Wet Chemical Method with Surfactant Addition and Subsequent Spark Plasma Sintering, Scientific Reports 7(1) (2017) 6051.

[49] Y. Kim, M.H. Hong, S.H. Lee, E.P. Kim, S. Lee, J.W. Nohl, The effect of yttrium oxide on the sintering behavior and hardness of tungsten, Metals and Materials International 12(3) (2006) 245-248.

[50] R.J. Brook, Pore-Grain Boundary Interactions and Grain Growth, J Am Ceram Soc 52(1) (1969) 56-&.

[51] J. Ma, J. Zhang, W. Liu, Z. Shen, Suppressing pore-boundary separation during spark plasma sintering of tungsten, Journal of Nuclear Materials 438(1-3) (2013) 199-203.

[52] S. Deng, T. Yuan, R. Li, F. Zeng, G. Liu, X. Zhou, Spark plasma sintering of pure tungsten powder: Densification kinetics and grain growth, Powder Technology 310 (2017) 264-271.

[53] K. Tsuchida, T. Miyazawa, A. Hasegawa, S. Nogami, M. Fukuda, Recrystallization behavior of hot-rolled pure tungsten and its alloy plates during high-temperature annealing, Nuclear Materials and Energy 15 (2018) 158-163.

[54] C. Ren, Z.Z. Fang, L. Xu, J.P. Ligda, J.D. Paramore, B.G. Butler, An

investigation of the microstructure and ductility of annealed cold-rolled tungsten, Acta Materialia 162 (2019) 202-213.

[55] W.M. Shu, A. Kawasuso, Y. Miwa, E. Wakai, G.N. Luo, T. Yamanishi, Microstructure dependence of deuterium retention and blistering in the near-surface region of tungsten exposed to high flux deuterium plasmas of 38 eV at 315 K, Physica Scripta T128 (2007) 96-99.

[56] A. Manhard, L. Gao, Blisters formed by D plasma exposure in an electron-transparent tungsten sample, Nuclear Materials and Energy 17 (2018) 248-252.

[57] Y. Oh, G. Min, K.-B. Roh, H. Kim, H.C. Kim, G.-H. Kim, H.N. Han, Competitive roles of dislocations on blister formation in polycrystalline pure tungsten, Journal of Alloys and Compounds 918 (2022).

[58] W.M. Shu, E. Wakai, T. Yamanishi, Blister bursting and deuterium bursting release from tungsten exposed to high fluences of high flux and low energy deuterium plasma, Nuclear Fusion 47(3) (2007) 201-209.

[59] W.M. Shu, A. Kawasuso, T. Yamanishi, Recent findings on blistering and deuterium retention in tungsten exposed to high-fluence deuterium plasma, Journal of Nuclear Materials 386-388 (2009) 356-359.

[60] X.-X. Zhang, L. Qiao, H. Zhang, Y.-H. Li, P. Wang, C.-S. Liu, Surface blistering and deuterium retention behaviors in pure and ZrC-doped tungsten exposed to deuterium plasma, Nuclear Fusion 61(4) (2021).

[61] Y. Ueda, T. Funabiki, T. Shimada, K. Fukumoto, H. Kurishita, M. Nishikawa, Hydrogen blister formation and cracking behavior for various tungsten materials, Journal of Nuclear Materials 337-339 (2005) 1010-1014.

[62] M. Zhao, W. Jacob, A. Manhard, L. Gao, M. Balden, U. von Toussaint, Z. Zhou, Deuterium implantation into Y_2O_3-doped and pure tungsten: Deuterium retention and blistering behavior, Journal of Nuclear Materials 487 (2017) 75-83.

[63] Y. Oh, W.-S. Ko, N. Kwak, J.-i. Jang, T. Ohmura, H.N. Han, Small-scale analysis of brittle-to-ductile transition behavior in pure tungsten, Journal of Materials Science & Technology 105 (2022) 242-258.

[64] C.A. Schuh, Nanoindentation studies of materials, Mater Today 9(5) (2006) 32-40.

[65] T.H. Ahn, C.S. Oh, D.H. Kim, K.H. Oh, H. Bei, E.P. George, H.N. Han, Investigation of strain-induced martensitic transformation in metastable austenite using nanoindentation, Scripta Materialia 63(5) (2010) 540-543.

[66] T.-H. Ahn, C.-S. Oh, K. Lee, E.P. George, H.N. Han, Relationship between yield point phenomena and the nanoindentation pop-in behavior of steel, Journal of Materials Research 27(1) (2011) 39-44.

[67] K.L. Johnson, K.L. Johnson, Contact mechanics, Cambridge university press1987.

[68] W.C. Oliver, G.M. Pharr, An Improved Technique for Determining Hardness

and Elastic-Modulus Using Load and Displacement Sensing Indentation Experiments, Journal of Materials Research 7(6) (1992) 1564-1583.

[69] T.H. Courtney, Mechanical behavior of materials, Waveland Press2005.

Chapter 3. Effect of potassium-doping on tungsten

3.1. Introduction

Tungsten is widely used as a plasma-facing material in an extreme environment where high temperatures, high heat fluxes, and high ion fluxes act in combination, such as in the divertor of a nuclear fusion reactor, due to its excellent properties, including a high melting point, high thermal conductivity, and low erosion rate [1-3]. However, it is known that the high ductile-to-brittle transition temperature (DBTT) of tungsten (300-400 °C [4]) significantly limits its applicable temperature range [5-7]. In particular, in the operating environment of a fusion reactor, plasma-facing components are exposed to a wide temperature range of 150-2400 °C ([8]) and experience intense thermal shock due to transient events such as edge localized modes [9]. This thermal shock may contribute to crack or destruction of the components and cause accidents such as coolant leakage [10]. Therefore, reduction of the DBTT in tungsten is an important issue for long-term and reliable utilization of the tungsten material in plasma-facing environments.

One of the most prominent approaches to enhancing the mechanical properties of materials, such as strength and toughness, is to properly design the microstructure [11-14]. For instance, it is known that nanocrystalline materials possess high strength owing to the Hall-Petch effect, while exhibiting minimal reduction in ductility [15]. Especially, in the case of tungsten, a high fraction of grain boundaries resulting from the nanocrystalline structure serves to dilute impurities like oxygen which lower grain boundary strength ([16]) and contributes to improving toughness [17, 18]. Another method to reduce the DBTT in tungsten through microstructural control is to introduce mobile dislocations through plastic deformation [19, 20]. Oh et al. conducted a comparative study on the yield stress and fracture stress of tungsten, demonstrating that dislocation motion can occur at lower stress compared to grain boundary fracture. Consequently, it was confirmed that tungsten can exhibit ductility when a sufficient amount of mobile dislocations is present within tungsten [20]. However, because tungsten with a nanocrystalline or heavily deformed microstructure contains numerous defects, prolonged exposure to elevated temperatures can result in the loss of the intended microstructure and properties through grain growth or recrystallization.

It is well known that the DBTT of tungsten can be significantly reduced through alloy design [21-23]. For instance, it has been reported that the addition of rhenium (Re) to tungsten greatly enhances its ductility [24, 25]. However, the W-Re alloy has a disadvantage in that radiation hardening or embrittlement occurs due to clustering of Re when the alloy is irradiated with high-energy particles or neutrons [26]. Potassium is another alloying element that has a beneficial effect on the mechanical properties of tungsten [27]. When potassium-doped tungsten (K-doped W) powder is sintered at a high temperature, potassium-bubbles (K-bubble) are formed within the tungsten by the vaporization of potassium due to its low boiling point (~760 °C) [28]. These K-bubbles can contribute to the improvement of material strength by impeding the movement of dislocations [29, 30]. It is commonly acknowledged that a trade-off relationship exists between the strength and ductility of metallic materials. However, in the case of K-doped W, simultaneous enhancements in both strength and ductility have been reported [28, 31, 32], and the underlying mechanism behind this phenomenon remains incompletely understood.

In this study, we investigated the factors contributing to the reduction of DBTT in tungsten through potassium doping, employing a combination of experiments and simulations. First, we conducted a comparative analysis of the microstructure and mechanical properties of K-doped W specimens prepared by sintering, in contrast to commercially available pure tungsten specimens with varying microstructures. The K-doped W was sintered using a spark plasma sintering (SPS) method known to be suitable for producing high-density tungsten [33, 34]. The microstructure of each specimen was characterized using electron backscatter diffraction (EBSD), and transmission electron microscopy (TEM) was employed to verify the presence of K-bubbles and analyze their shape and size distribution within the K-doped W specimen. Uniaxial tensile tests were conducted at different temperatures to assess the DBTT of the specimens, and nanoindentation tests were performed to examine the microscopic mechanical properties. To gain insight into the underlying mechanisms of the observed differences in mechanical properties, molecular dynamics (MD) and dislocation dynamics (DD) simulations were performed, and the results were analyzed by correlating with the experimental findings. Furthermore, to assess the feasibility in a practical fusion reactor, plasma-facing properties, such as thermal stability, resistance to deuterium irradiation, and deuterium retention, were tested and analyzed.

3.2. Experimental procedures

3.2.1 Materials and methods

In this study, commercially available K-doped W powder (Xinzhou Great Wall Tungsten & Molybdenum, ~2.8 μm) was used to fabricate the sintered specimen (Figure 29). The K-doped W powder underwent hydrogen reduction at 1200°C for 2 h in a 99.999% H_2 atmosphere to lower the oxygen content. The H_2-reduced K-doped W powder was placed in a graphite mold, with a graphite foil and a tantalum (Ta) foil inserted between the mold and the powder, which serving as a lubricant and a carbon diffusion barrier, respectively [35]. The sintering was carried out using an SPS machine (Welltech). The specimen was heated to sintering temperature at a heating rate of 200 °C/min, maintained for 5 minutes, and then cooled within the machine. The sintering pressure was initially set at 20 MPa, increased to 80 MPa at 1000 °C, and maintained until the end of sintering. The sintering process was conducted in a vacuum of approximately 10^{-5} atm. For comparison with the K-doped W specimens produced by SPS, two types of pure tungsten specimens (As-received W and Annealed W) were prepared. The As-received W specimen was obtained from a commercially available high-purity tungsten sheet (Plansee, Austria, purity: 99.997%) fabricated through sintering and subsequent thermodynamic processes. The Annealed W specimen was prepared by heat treatment of the As-received W in an atmosphere of 5% H_2 and 95% Ar. During the heat treatment, the specimens were heated to 1450 °C at a heating rate of 5 °C/min below 1200 °C and 3 °C/min above 1200 °C. Subsequently, the specimens were held at 1450 °C for 1 h and cooled to room temperature at a cooling rate of 3 °C/min. At this time, the flow rate of 5% H_2 and 95% Ar gas was set to 1 L/min.

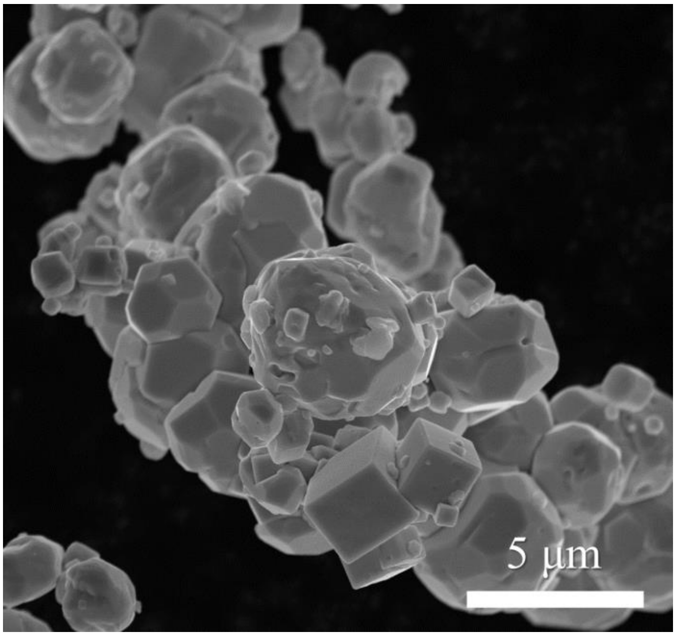

Figure 29 SEM image of initial K-doped W powder.

3.2.2 Characterization

The morphologies of the powders and specimens were examined using a field-emission scanning electron microscopy (FE-SEM) device (SU-70, Hitachi) equipped with an EBSD system (EDAX/TSL, Hikari). Grain size was measured based on high-angle grain boundaries with a misorientation angle of 15° to adjacent grains. To evaluate the amount of dislocation inside each sample, an X-ray diffraction (XRD, D8 advance, Bruker) instrument with a copper $K_{\alpha1}$ radiation source was used. XRD data were obtained at a scan rate of 1°/min in the range of 30-120°. The XRD patterns were analyzed using the convolutional multiple whole profile fitting method [36, 37]. Nano-sized K-bubbles were identified and characterized using field-emission transmission electron microscopy (FE-TEM, JEM-2100F, JEOL Ltd), and TEM specimens were prepared using a focused ion beam device (FIB, Helios G4, Thermo Fisher Scientific). The density of the specimen was measured using the Archimedes method, and the theoretical density of K-doped W was assumed to be 19.25 g/cm^3, the same as that of pure tungsten, due to the small potassium composition.

The mechanical properties of the specimens were measured through miniature uniaxial tensile tests and nanoindentation tests. The macroscopic mechanical properties of the specimens were evaluated at various temperatures using a universal testing machine (INSTRON 5584, Instron Inc.). The uniaxial tensile test was conducted in a furnace, and the temperature of the specimen was measured using a thermocouple. The strain rate was set to 10^{-3} s^{-1} in all tests. Miniature uniaxial tensile specimens were machined to have gauge widths, lengths, and thicknesses of 1.2 mm, 5 mm, and 2 mm, respectively. For the As-received W and the Annealed W, the length and thickness directions of the sample were parallel to the rolling and normal directions. Microscopic mechanical properties of the specimens were measured using a nanoindenter (Ti 750 L UBi, Hysitron). For the As-received W and the Annealed W, nanoindentation tests were performed on a surface perpendicular to the rolling direction, and the surface was mechanically polished and electropolished. In the case of K-doped W, nanoindentation tests were performed on the top surface of the specimen, and the tested surface was prepared by polishing with low pressure for a long time to minimize the formation of dislocations during mechanical polishing. Nanohardness was measured using a Berkovich-type diamond indenter tip with loading and unloading rates of ±1000 μN·s^{-1} and a maximum load of 5000 μN, and the dwelling time was 2 s. To exclude the effects of grain boundaries from the nanohardness measurements, only the tests conducted on the grain interior were selected through FE-SEM observation and analyzed.

To evaluate the thermal stability of the K-doped W specimen, heat treatment was performed on the specimens at elevated temperatures, and the changes in microstructure and Vickers hardness (Duramin-40 M1, Sturers) were analyzed. The specimens were subjected to a temperature of 1700°C in a 95% Ar + 5% H_2 atmosphere and held at this temperature for a maximum of 10 h. The heating rate was 5°C/min below 1000°C and adjusted to 3°C/min above 1000°C, while the cooling rate was set to 3°C/min. Throughout the heat treatment process, the flow rate of 5% H_2 and 95% Ar gas was set to 1 L/min. To evaluate the resistance to plasma ion flux, specimens with a diameter of 10 mm were irradiated with deuterium using electron-cyclotron-resonance (ECR) system. The incident ion energy was 100 eV per D_2^+, and the corresponding target bias and plasma potential were −87 V and 13 V, respectively. The ratio of D^+, D_2^+ and D_3^+ ion fluxes on the specimens was estimated to be 5:80:15 by the hydrogen global model, and the total ion flux was 4.74×10^{21} D^+ m^{-2} s^{-1}. All specimens were exposed for 4 h, which corresponded to a total fluence of ~6.8×10^{25} D^+ m^{-2}. The deuterium retention of each specimen was examined using thermal desorption spectroscopy (TDS). The TDS temperature range was 300–1273 K with a heating rate of 12 K·s^{-1}, which satisfied the Redhead approximation and the Kissinger equation for the analysis of desorption energy from the TDS spectra [38]. The retained amount of deuterium was calculated by integrating the release rate with respect to the temperature in the TDS spectrum.

3.2.3 Simulations

MD simulations were conducted to investigate the influence of nano-sized bubbles on dislocation behavior during nanoindentation tests. The simulations were performed using the LAMMPS (Large-scale Atomic/Molecular Massively Parallel Simulator) MD package. The Open Visualization Tool (OVITO [39]) was employed to visualize the simulation results, and the dislocation extraction algorithm (DXA) was utilized to analyze the nucleation and formation of dislocations during the simulation [40, 41]. For the accurate capture of physical and microstructural characteristics such as elasticity, structure, and defects of pure tungsten, a novel interatomic potential based on the second-nearest-neighbor modified embedded-atom method was employed [42]. The simulation cell dimensions were set to 236.14 × 157.43 × 236.14 nm, and the bubble was assumed as a spherical cavity with a diameter of 3.165 nm. The total number of atoms within the cell was 562,500. The initial cell was structurally optimized through an MD run using the conjugate gradient method. Energy stabilization was performed for 10 ps under the designated temperature and zero pressure conditions in the isothermal-isobaric (NPT) ensemble. For the indentation simulations, the diameter of the spherical indenter tip was set to 20 nm, and the tip speed was set to 100 m/s. The size of the indenter tip was selected to maintain a similar size ratio between the bubble and the indenter tip as the actual nanoindentation experiments. A fixed boundary condition was applied in the direction of indentation (y-axis), while periodic boundary conditions were used for the other two axis directions (x, z-axis). A time step of 1 fs was employed for all simulations, and temperature and pressure were controlled using a Nosé-Hoover thermostat and barostat, respectively. The simulation temperature was set to 300 K [43, 44].

Mesoscale finite element method (FEM) analysis and DD simulation were conducted to analyze the influence of nano-sized bubbles on the behavior and interaction of dislocations during nanoindentation, as well as their impact on the mechanical properties of tungsten. In the FEM analysis, the cell size was set to 20 × 10 × 20 μm. The indenter tip diameter was set at 360 nm and the indentation depth was 10 nm. DD simulations were performed using the parallel dislocation simulator (ParaDiS), a code developed by Lawrence Livermore National Laboratory [45].

Initially, the simulation cell was set as a single crystal with dimensions of 20 × 10 × 20 μm. However, the DD simulation focused on a smaller region of 2 × 1 × 2 μm beneath the indenter tip, as dislocation plasticity was observed only in that specific region. The nano-sized bubble was considered as a spherical cavity with a diameter of 25 nm, positioned 50 nm away from the indentation face. The diameter of the spherical indenter tip was set to 360 nm.

3.3. Results and discussion

3.3.1 Fabrication of potassium-doped tungsten specimen

To investigate the influence of impurities on the microstructure after sintering, K-doped W specimens were fabricated with and without the application of Ta foil as a carbon diffusion barrier at different sintering temperatures. Figures 30 (a and b) presents the EBSD inverse pole figure map normal to the center of the top surface of the sintered K-doped W specimen produced without Ta foil. It clearly indicates the occurrence of abnormal grain growth in the K-doped W specimen. However, when Ta foil was applied during the sintering process (Figures 30 (c and d)), no abnormal grain growth was observed in the K-doped W specimen. It is well known that Ta foil can effectively prevent carbon diffusion from the graphite mold and punch during SPS [35]. Therefore, it can be concluded that the carbon diffusion from the mold may have an effect on the evolution of abnormal grain growth. Since the presence of abnormal grain leads to microstructural and mechanical inhomogeneities in the K-doped W specimen, it is important to minimize this phenomenon. Consequently, we selected the adjustment of Ta foil between the K-doped W powder and the graphite mold to inhibit abnormal grain growth during SPS.

Despite the use of Ta foil during sintering, the occurrence of abnormal grain growth near the surface region cannot be completely eliminated, if K-doped W is spark plasma sintered (SPSed) at high sintering temperatures. Figure 31 (a) and Figure 31 (b) present the microstructures near the cylindrical surface of the Ta foil-applied K-doped W specimen fabricated at 1700 °C and 1800 °C, respectively. In the specimen sintered at 1800 °C (Figure 31 (b)), abnormal grains with a size of approximately 100 μm were observed in close proximity to the Ta foil, which is roughly 30 times larger than the average grain size. However, in the specimen sintered at 1700 °C, no abnormal grain growth was observed, indicating that this sintering temperature is suitable for the sintering of the K-doped W powder. Therefore, all the K-doped W specimens investigated in this study were sintered at 1700 °C.

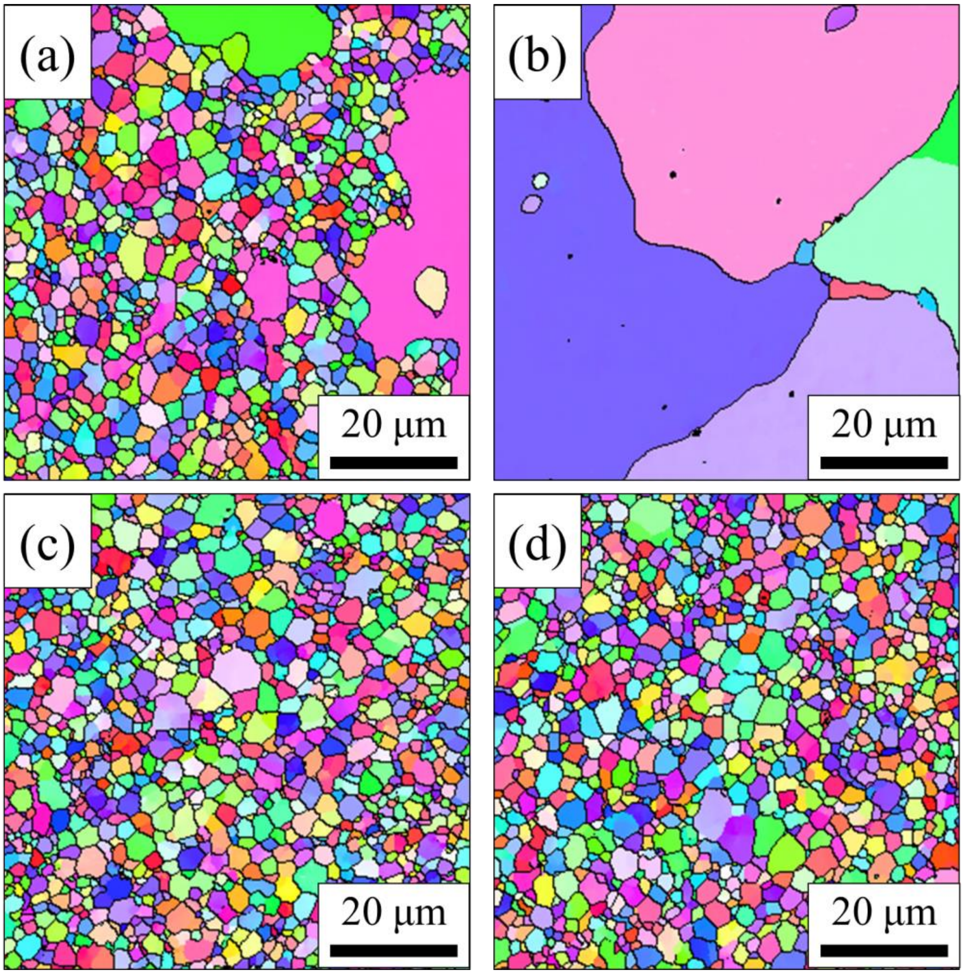

Figure 30 the inverse pole figures along the normal direction of the center of top surface of the K-doped W sintered with difference conditions; (a) sintered at 1700°C without Ta foil, (b) sintered at 1800°C without Ta foil, (c) sintered at 1700°C with Ta foil, (d) sintered at 1800°C without Ta foil.

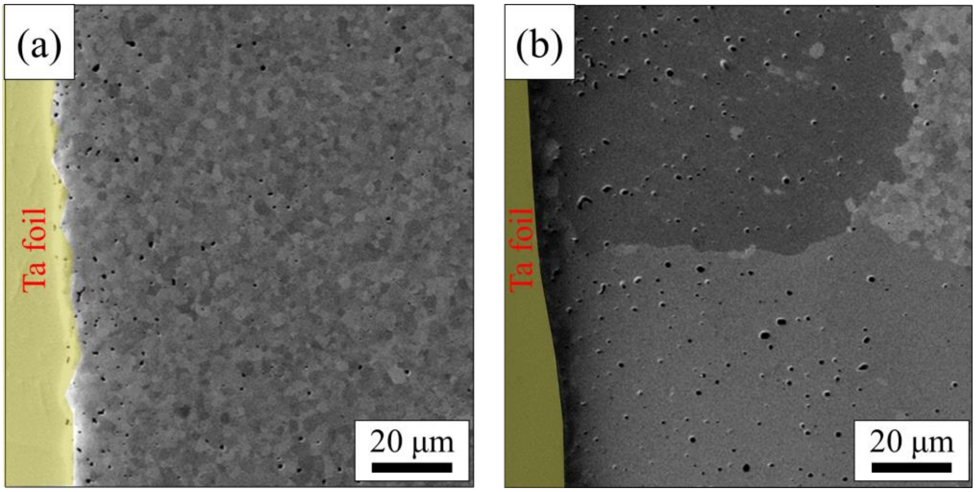

Figure 31 the SEM images about a region near the cylindrical surface of top surface of the K-doped W specimens sintered with applying Ta foil at (a) 1700°C, and (b) 1800°C.

3.3.2 Characterization of specimens

Figure 32 shows the microstructures of the As-received W, Annealed W, and K-doped W specimens. The As-received W specimen exhibits a deformed structure elongated along the transverse direction and consists of grains displaying a color gradient internally (Figure 32 (a)). The color gradient indicates lattice distortion within the grains, suggesting the presence of numerous dislocations in the specimen. After being annealed at 1450 °C, the previously deformed grains undergo complete recrystallization, as indicated by the uniform color observed in the grains (Figure 32 (b)). It corresponds with previous researches reporting the recrystallization temperature of pure tungsten to be around 1300 °C [46, 47] . The average grain sizes of the As-received W and Annealed W specimens were measured to be 86.38 ± 64.88 μm and 247.45 ± 136.31 μm, respectively (Table 3). Figure 32 (c) illustrates the microstructure of the K-doped W specimen. K-doped W exhibits a uniform microstructure with an average grain size of 3.20 ± 1.26 μm. This fine-grained structure could be attributed to the formation of K-bubbles resulting from the vaporization of potassium during the sintering process of K-doped W powder [28]. The K-bubbles at grain boundaries can contribute to the maintenance of initial particle sizes (~2.8 μm) by hindering grain boundary migration.

TEM observation was conducted to verify the presence of K-bubbles in the K-doped W specimens and analyze their shapes and sizes. Figure 33 (a) shows a high-angle annular dark-field scanning TEM image of a K-doped W specimen, revealing light-colored spherical defects embedded within the dark-colored tungsten matrix. To determine the composition of the defects and the matrix, energy dispersive spectrometer (EDS) analysis was performed at Point 1 (defect) and Point 2 (matrix) in Figure 33 (a). The EDS results showed the presence of 0.22 wt.% of K at Point 1 (Figure 33 (c)), while no potassium was detected at Point 2 (Figure 33 (d)). Considering that the composition of potassium in K-doped W is approximately 0.0033 wt.% (Table 3), it can be concluded that the spherical defects observed in Figure 33 (a) are bubbles formed by potassium. The size distribution of K-bubbles was measured by statistically analyzing about 160 bubbles in several TEM images. Figure 33 (b) shows the size distribution of K-bubbles, which predominantly ranged from 20 nm to 200 nm, with an average size of 55.52 ± 23.64 nm. Despite the presence of these K-bubbles, the relative density of K-doped W (99.66%, Table 3) indicates that the sample is fully densified.

XRD experiments were performed to quantify the dislocation densities inside As-received W, Annealed W, and K-doped W specimens. It is known that the Fourier coefficient (A_L) of X-ray diffraction pattern can be expressed as the product of the 'size' and 'distortion' coefficients, A_L^{S} and A_L^{D} [48].

$$\mathrm{A_L}(L) = A_L^S(L)A_L^D(L) \tag{1}$$

where, L is a Fourier length, defined as $L = Na_3$. N is an integer, and a_3 is a Fourier length unit in the direction of diffraction vector (**g**).

$$a_3 = \lambda\,/[2(\sin\theta_2 - \sin\theta_1)] \tag{2}$$

where, $\theta_1$and θ_2 represent the starting and ending angles in the XRD experiment, and λ is a wavelength of the X-ray. According to Warren and Averbach [49], the A_L^{D} can be expressed as follows:

$$A_L^D(L) = exp(-2\pi^2\mathbf{g}^2L^2\langle\varepsilon_{\mathbf{g},L}^2\rangle) \tag{3}$$

where, $\langle\varepsilon_{\mathbf{g},L}^2\rangle$ is mean square strain in the direction of the diffraction vector, which is associated with relative displacement about ideal atomic position. Assuming that dislocations are randomly distributed within a region with effective outer cut-off radius (R_e) and that there is no interaction between dislocations outside of these regions, $\langle\varepsilon_{\mathbf{g},L}^2\rangle$ can be written as [50, 51] :

$$\langle\varepsilon_{\mathbf{g},L}^2\rangle = (\rho_d\bar{C}b^2/4\pi)\,ln(R_e/L) \tag{4}$$

where, ρ_d is dislocation density, b is a Burgers vector, and $\bar{C}$ is a contrast factor of dislocation. In this method, the parameters in $\bar{C}$ are not fitted, but are fixed to particular values. Combining the Equations 1, 3, and 4 gives the following equation, which is known as "*modified Warren-Averbach* equation".

$$\ln A_L(L) = \ln A_L^S(L) - \rho_d B_L L^2 \, ln(R_e/L) \, (\mathbf{g}^2 \bar{C}) \tag{5}$$

where, $B_L = \pi b^2/2$. For the each L_i value, $\ln A_L(L_i)$ can be fitted by a linear equation $a_i + b_i \mathbf{g}^2 \bar{C}$. By plotting the exponential of the a_i values as a function of L, the size Fourier transform (A_L^S) can be obtained. Additionally, by applying linear regression to the initial straight region of the $\ln L - b_i/L^2$ plot, the slope (=$\rho_d B_L$) and y-intercept ($= -\rho_d B_L \, ln \, R_e$) can be obtained. Therefore, it is possible to evaluate the dislocation density of the material.

To employ the adapted Warren-Averbach equation, it is necessary to acquire an experimental C value. To this purpose, we utilized the "*modified Williamson-Hall* equation," which allows the determination of the fraction of edge and screw dislocations within the specimen based on the XRD profile. This technique relies on the anisotropic contrast of dislocations observed in the diffraction pattern and is expressed as follows [52]:

$$\Delta K = \frac{0.9}{D} + \left(\frac{\pi M^2 b^2 \rho_d}{2} K^2 \bar{C} \right)^{\frac{1}{2}} \tag{6}$$

where ΔK is peak width and D is average grain size. M is the dimensionless parameter depending on the effective outer cutoff radius of dislocation. ΔK and K can be obtained as a function of full-width half-maximum (β) and Bragg angle (θ) of diffraction peaks.

$$\Delta K = \frac{2\beta \, cos(\theta)}{\lambda}, \qquad K = \frac{2 \, sin \, \theta}{\lambda} \tag{7}$$

The value of $\bar{C}$ depends on {hkl} reflections, and in the case of a cubic crystal structure, it can be mathematically expressed as [51]:

$$\bar{C} = \bar{C}_{h00}(1 - qH^2) \tag{8}$$

$$H^2 = \frac{h^2k^2 + k^2l^2 + l^2h^2}{(h^2 + k^2 + l^2)^2} \tag{9}$$

Here, $\bar{C}_{h00}$ represents the average dislocation contrast factor for {h00} reflections. The value of q depends on the characteristic of the dislocation (edge or screw) and can be obtained through experiments [51]. The combination of Equation 6 with Equation 8 is expressed as:

$$\frac{[(\Delta K)^2 - \alpha^*]}{K^2} = \beta^*\bar{C}_{h00}(1 - qH^2) \tag{10}$$

where $\alpha^* = (0.9/D)^2$ and $\beta^* = (\pi M^2 b^2 \rho_d/2)$. If one applies linear regression for $[(\Delta K)^2 - \alpha^*]/K^2$ with respect to H^2 and the fitting function is expressed by $y = A^*x + B^*$, the slope (A^*) and the y intercept (B^*) will correspond to $-q\beta^*\bar{C}_{h00}$ and $\beta^*\bar{C}_{h00}$, respectively. Therefore, the experimental q value can easily be obtained as $-A^*/B^*$ (Figure 34). The fraction of edge and screw dislocation can be calculated by comparing the experimental q with theoretical values (q^{th}) of pure edge and screw components [53].

$$f_{edge} = \frac{q^{th}_{screw} - q}{q^{th}_{screw} - q^{th}_{edge}} \tag{11}$$

$$q^{th} = a^q\left[1 - exp\left(-\frac{A_i}{b^q}\right)\right] + c^qA_i + d^q \tag{12}$$

$$A_i = \frac{2C_{44}}{C_{11} - C_{12}} \tag{13}$$

where f_{edge} is fraction of edge dislocation and A_i is elastic anisotropy, which depended on elastic constants ($C_{11}, C_{12}, and\ C_{44}$) of the material. parameters a^q, b^q, c^q, and d^q also depend on the elastic constants.

The $\bar{C}_{h00}$ can be calculated by a weighted average of C_{h00} values for pure edge and screw components considering the calculated fractions of each component. C_{h00} is also expressed by a^C, b^C, c^C, and d^C as follows [51]:

$$C_{h00} = a^C \left[1 - exp\left(-\frac{A_i}{b^C}\right)\right] + c^C A_i + d^C \tag{14}$$

We have used the reported elastic constants, C_{11} (501 GPa), C_{12} (198 GPa), and C_{44} (151 GPa), of pure tungsten [54]. Other parameters required for Equations 12 and 14 are listed in Table 4 [51].

The regression of the XRD pattern utilized the Convolutional Multiple Whole Profile Fitting (CMWP) method, which is a technique for fitting the entire XRD profile based on the *modified Warren-Averbach* analysis. For this purpose, the lattice constant and Burgers vector were set to 0.3159 nm and 0.274 nm, respectively [54]. Moreover, the contrast factor was used as 0.1582, which is obtained by *modified Williamson-Hall* analysis for K-doped W. The XRD profile for K-doped W and its corresponding fitting result can be observed in Figure 35, while the corresponding dislocation densities and mean distance between dislocations ($l_d = 1/\sqrt{\rho_d}$) in specimens are presented in Table 5.

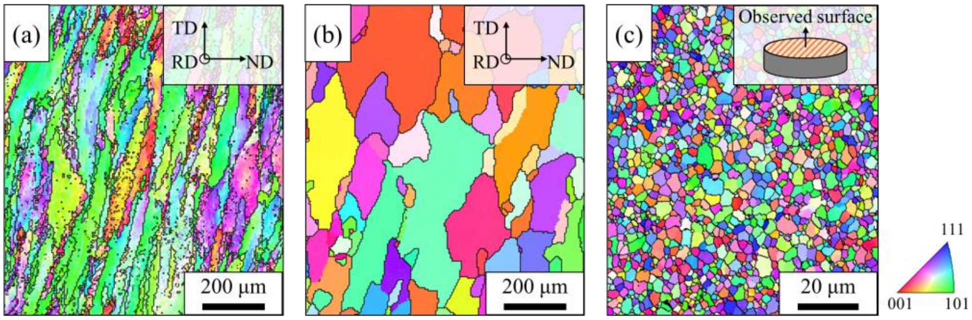

Figure 32 the inverse pole figures along the normal direction of the observed surfaces of the specimens: (a) As-received W, (b) Annealed W, and (c) K-doped W.

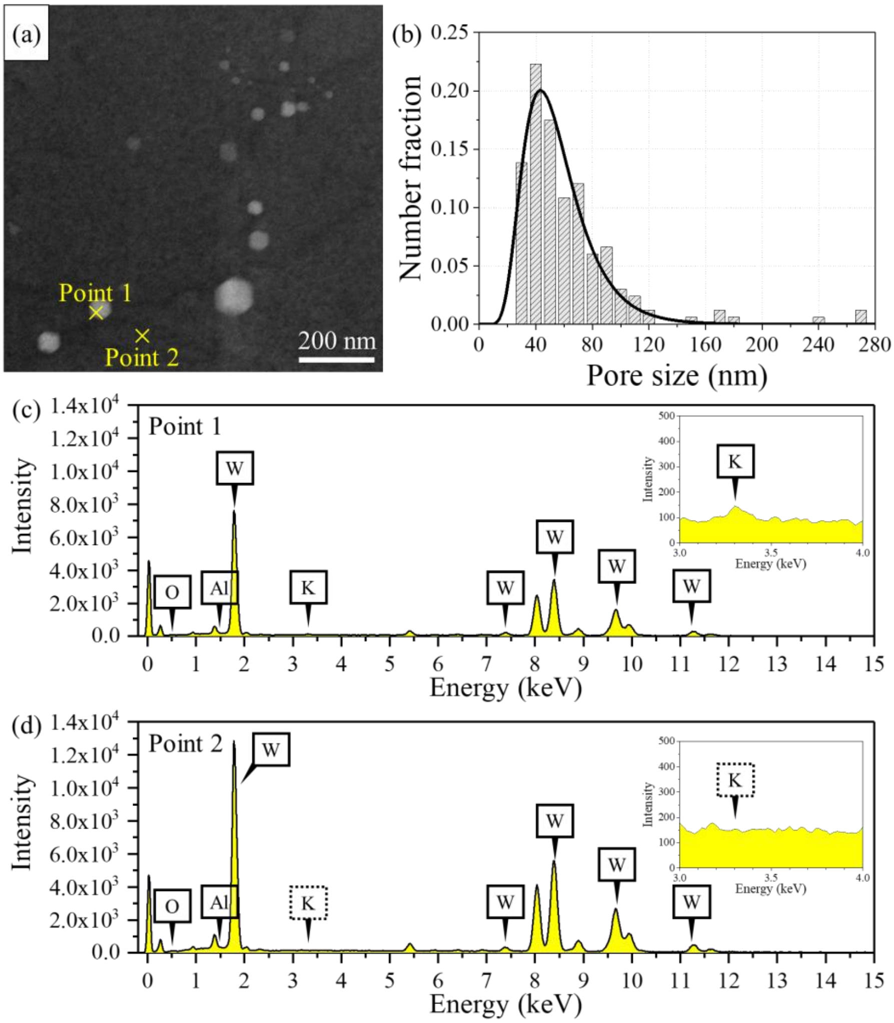

Figure 33 (a) High angle annular dark field scanning TEM image of K-doped W sample; (b) Size distribution of pores; (c-d) EDS results about the yellow points in (a).

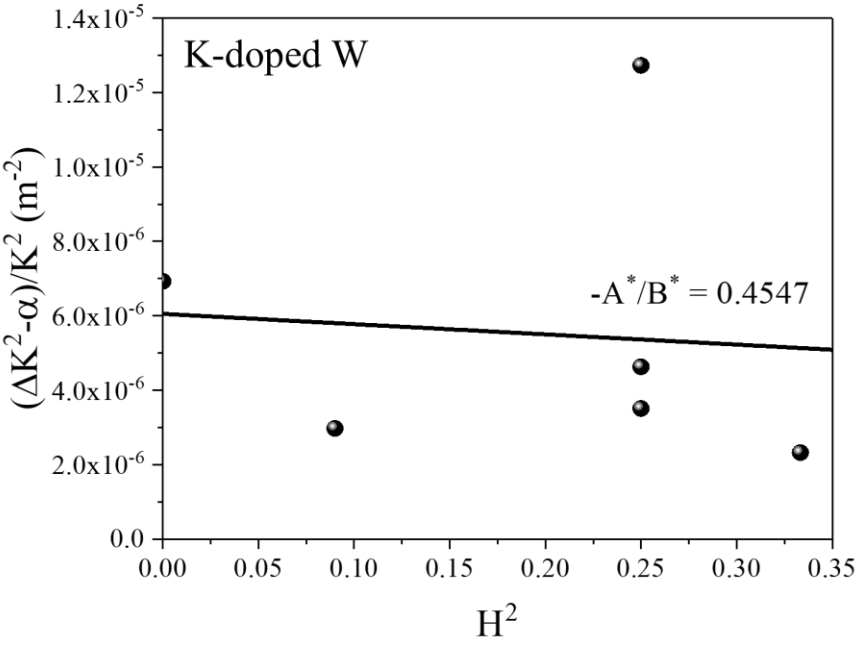

Figure 34 Modified Williamson-Hall fitting for K-doped W specimen.

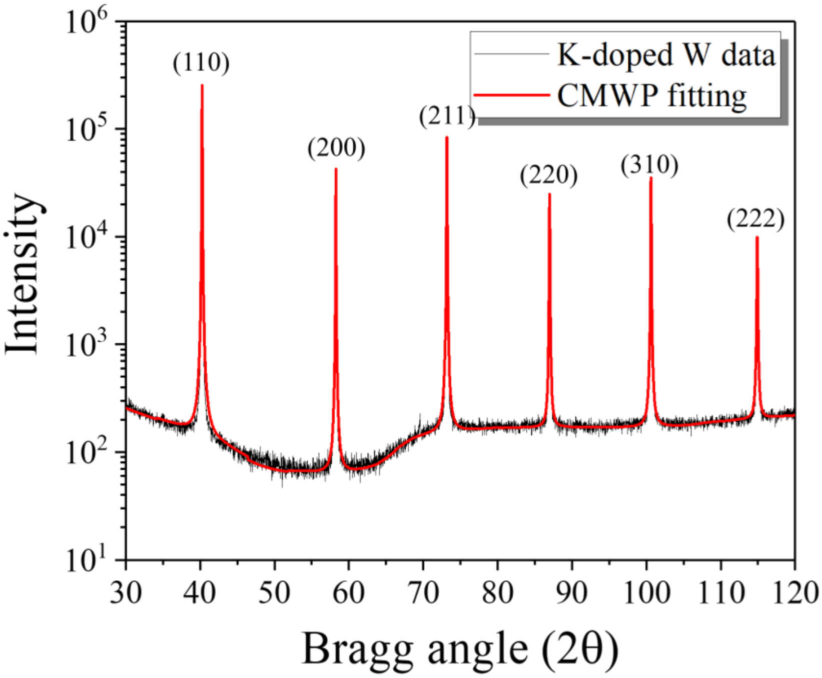

Figure 35 XRD profile and CMWP fitted line for K-doped W.

Table 3 Sample characterization.

	Composition	Grain size (μm)	Relative density (%)
As-received W	> 99.997 wt.%W	86.38 ± 64.88	> 99.99
Annealed W	> 99.997 wt.%W	247.45 ± 136.31	> 99.99
K-doped W	W-0.0033 wt.%K	3.20 ± 1.26	99.66

Table 4 Input values of the parameters (a, b, c, and d) for determining q and C_{h00} for the pure screw and edge components in tungsten.

Parameter	Edge dislocation	Screw dislocation
a^q	7.2361	8.6590
b^q	0.9285	0.3730
c^q	0.1359	0.0424
d^q	-5.7484	-6.074
a^C	1.6690	0.1740
b^C	21.124	1.9522
c^C	0	0.0293
d^C	0.0757	0.0662

Table 5 Dislocation density and mean distance between the dislocations.

	Dislocation density (ρ_d, m^{-2})	Mean distance between dislocations (l_d, nm)
As-received W	3.51×10^{14}	53.38
Annealed W	3.78×10^{12}	514.34
K-doped W	4.58×10^{12}	467.27

3.3.3 Effect of potassium-doping on mechanical behavior of tungsten

Figure 36 illustrates the engineering stress-strain curves obtained from uniaxial tensile tests conducted at various temperatures for the As-received W, Annealed W, and K-doped W specimens. At low temperatures, the specimens underwent fracture during elastic deformation. However, at temperatures above a certain threshold, the specimens exhibited plastic deformation prior to fracture. Based on these experimental results, it can be concluded that the DBTT of the As-received W, Annealed W, and K-doped W specimens lie within the ranges of approximately 300–330 °C, 350–400 °C, and 300–350 °C, respectively.

Figure 37 illustrates the fractured surfaces of As-received W, Annealed W, and K-doped W specimens after uniaxial tensile testing. The SEM images of the fractured surfaces of Annealed W (Figure 37 (b)) and K-doped W (Figure 37 (c)) specimens, performed uniaxial tensile tests in the DBTT region, exhibit characteristics of brittle fracture. Predominantly, intergranular fractures were dominantly observed in both specimens and some transgranular fractures were also observed in localized areas. It is a typical fractured surface observed when recrystallized tungsten fractures at temperatures below its DBTT [55, 56]. After tensile tests at temperatures above the DBTT region, although intergranular fractures remained the primary mode of fracture, some evidences of plastic deformation, such as slip traces [57] (indicated by arrows in Figure 37 (e)) or knife-edge grains [58] (indicated by arrows in Figure 37 (f)), were identified. In contrast to Annealed W and K-doped W specimens, the fractured surface of As-received W specimens tested within the DBTT region predominantly shows a delaminated flat fracture profile, indicating brittle fracture of the specimens (Figure 37 (a)) [59]. These trends correspond with the uniaxial tensile tests (Figure 36).

Figure 38 shows the tensile toughness of As-received W, Annealed W, and K-doped W specimens as a function of temperature. The tensile toughness was calculated by integrating the engineering stress-strain curve within the plastic deformation range. According to Oh et al. [20], the DBTT of pure tungsten tends to decrease with an increase in dislocation density. The dislocation densities were measured to be 3.51×10^{14} m^{-2}, 3.78×10^{12} m^{-2}, and 4.58×10^{12} m^{-2} for the As-received W, Annealed W, and K-doped W specimens, respectively (Table 5). As-received W exhibited higher tensile toughness compared to Annealed W, which can be attributed to its higher dislocation density. In the case of K-doped W, it has a larger fraction of grain boundaries that serve as initiation sites and propagation paths for cracks, while the dislocation density in K-doped W is of the same order of magnitude as that of Annealed W. Despite these facts, K-doped W displayed significantly higher tensile toughness than Annealed W. It suggests that potassium has a significant effect on reducing the DBTT of tungsten.

Nanoindentation tests are suitable for evaluating the local plasticity of a material owing to its small activation volume. Therefore, nanoindentation tests were performed on the As-received W, Annealed W, and K-doped W specimens to investigate their mechanical properties by excluding the influence of grain boundaries. The maximum shear stress for inducing plastic yield can be calculated based on the "pop-in" phenomenon, which is a sudden burst of displacement at the same load during an indentation test [60-62]. The details on estimating the maximum shear stress under pop-in load obtained from load–displacement curves (Figure 39) have been provided in Section 2.3.5.

Figure 40 illustrates the cumulative probability distribution of the maximum shear stress for yielding measured in three specimens. Initially, in the case of the As-received W specimen, the average maximum shear stress was determined to be 11.5 ± 2.54 GPa (Table 6), which was lower compared to the other two specimens. These low maximum shear stresses can be attributed to the presence of mobile dislocations in the specimen. The mean distance between dislocations in the As-received W specimen (~53.38 nm, Table 5) is shorter compared to the other specimens due to the higher dislocation density in the specimen. This mean distance is comparable to the diameter of the contact surface during the nanoindentation test (~59 nm, Table 6). Consequently, it is highly probable that dislocations are present below the indenter tip during the experiment on the As-received W specimen. The Peierls-Nabarro stress, which represents the stress required for dislocation gliding in pure tungsten, is reported as 7.28 GPa [42], indicating that As-received W can easily undergo plastic deformation even at relatively low stresses. On the other hand, the mean distance between dislocations in the Annealed W specimen (~514.34 nm, Table 5) is larger than the diameter of the contact surface of the nanoindenter tip (~124 nm, Table 6). It suggests that dislocations may not exist directly beneath the nanoindenter tip during nanoindentation testing in Annealed W. Therefore, in order for the Annealed W specimen to undergo plastic deformation, the nucleation of dislocations must be accompanied. As a result, the plastic deformation of Annealed W requires a higher maximum shear stress (21.7 ± 0.94 GPa, Table 6), which is closer to the theoretical shear strength of pure tungsten (~25 GPa [63]).

In the case of K-doped W specimens, the mean distance between dislocations (~478.36 nm, Table 5) is significantly larger than the diameter of the contact surface (~79 nm, Table 6). It implies that a plastic deformation in K-doped W specimen requires the nucleation of dislocations, similar to the case of Annealed W. However, the maximum shear stress measured in K-doped W was 14.3 ± 4.20 GPa (Table 6), which is considerably lower than the theoretical shear stress of pure tungsten. Therefore, it can be concluded that dislocations can form in K-doped W with significantly less stress than expected in a perfect crystal of pure tungsten.

Figure 41 illustrates the nanohardness of As-received W, Annealed W, and K-doped W specimens as cumulative probability distributions. The average nanohardness of the As-received W specimen was found to be 7.43 ± 0.23 GPa, which is higher than those of the other two specimens. It can be attributed to the work hardening effect resulting from the high dislocation density present in the specimen. In contrast, the average nanohardness of the Annealed W specimen was determined to be 6.11 ± 0.28 GPa, which is the lowest among the three specimens, indicating the absence of hardening effects. For the K-doped W specimen, the average nanohardness was measured to be 7.16 ± 0.35 GPa, which is closer to that of the As-received W specimen rather than the Annealed W specimen. It suggests that the nano-sized K-bubbles in the specimen can contribute to hinder the movement of dislocations, thereby increasing its hardness.

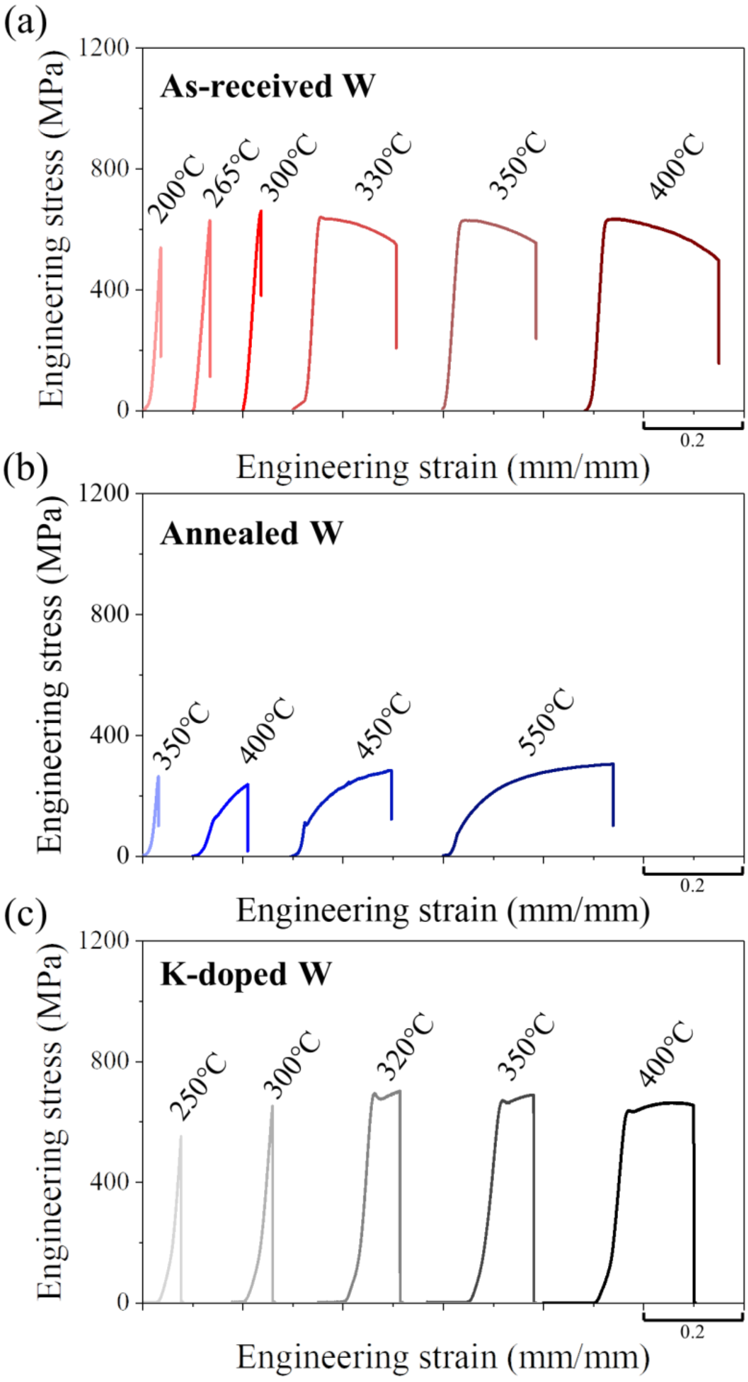

Figure 36 Engineering stress–strain curves of uniaxial tensile tests; (a) As-received W, (b) Annealed W, and (c) K-doped W. ((a) and (b) were reproduced utilizing the data obtained from [42].)

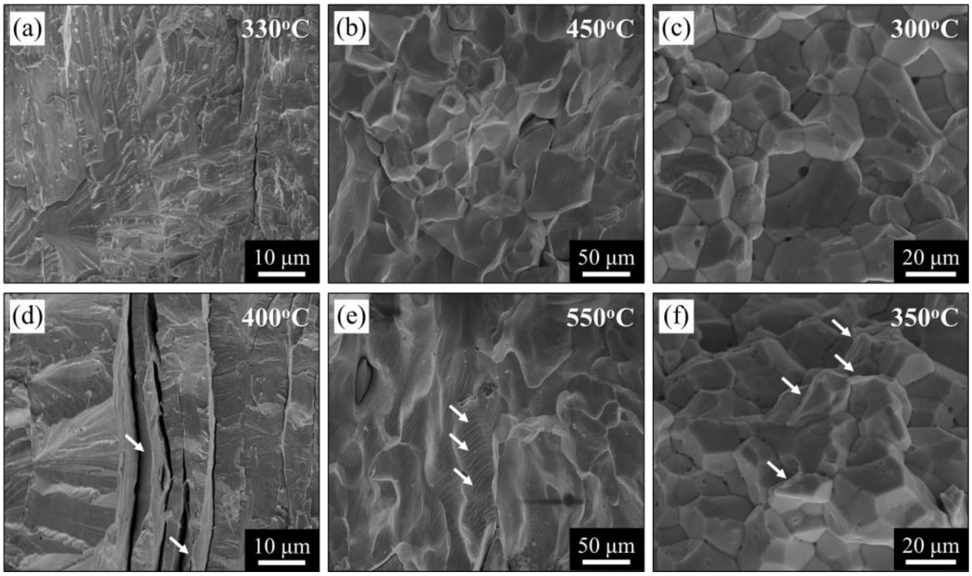

Figure 37 Fractured surfaces of samples after uniaxial tensile tests; (a, d) As-received W, (b, e) Annealed W, and (c, f) K-doped W.

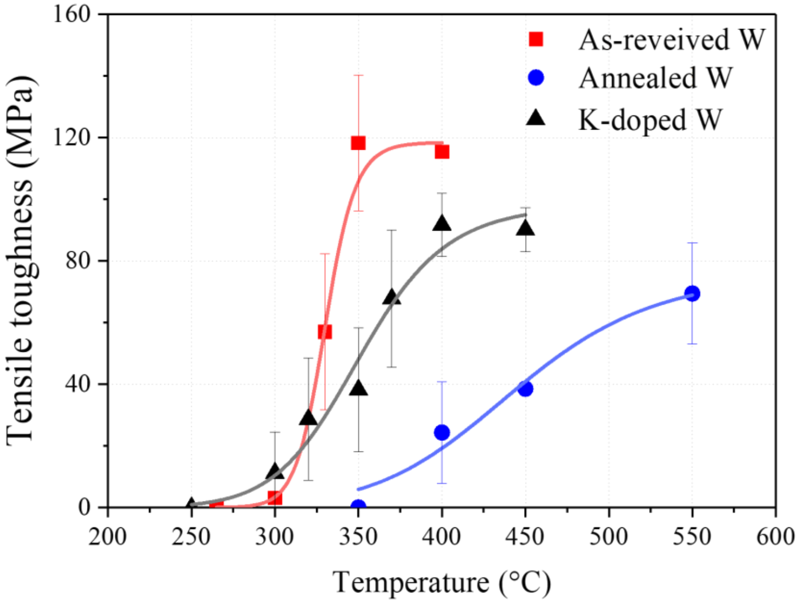

Figure 38 The toughness of the specimens obtained from uniaxial tensile tests. (As-received W and Annealed W data were utilized from [42].)

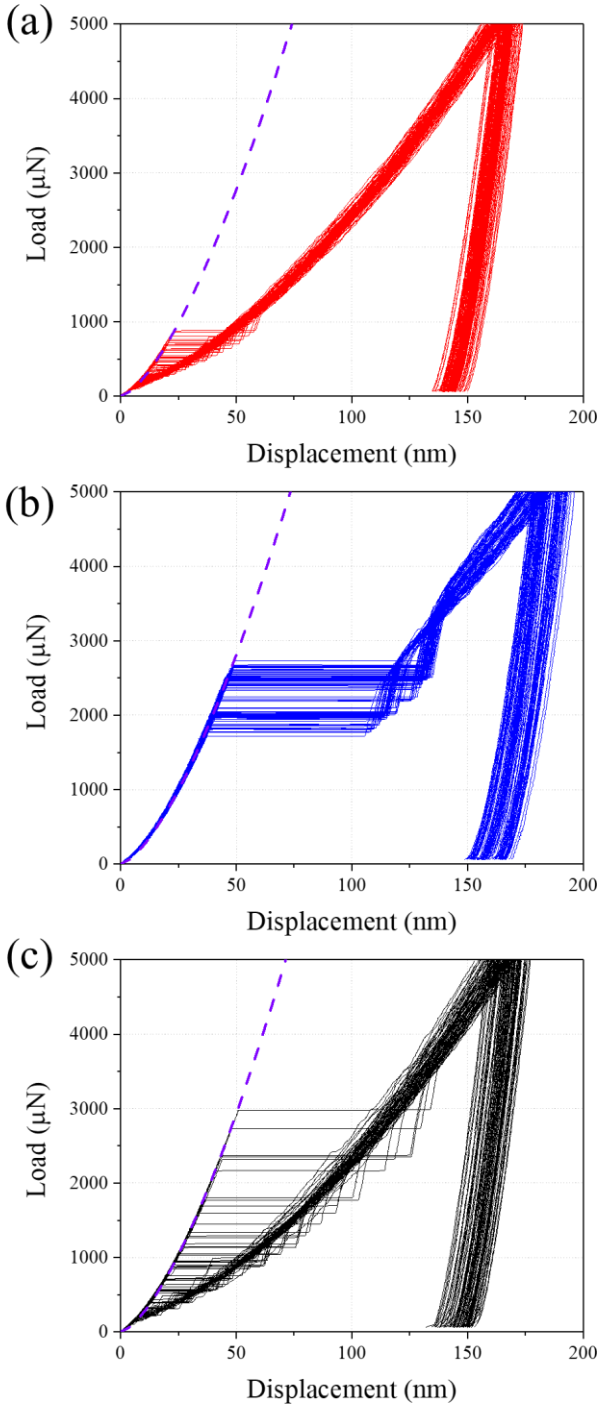

Figure 39 Load-displacement curves of (a) As-received pure W, (b) Annealed pure W, and (c) K-doped W during nanoindentation tests. The purple dotted lines are obtained by fitting the elastic deformation region with Hertzian curve.

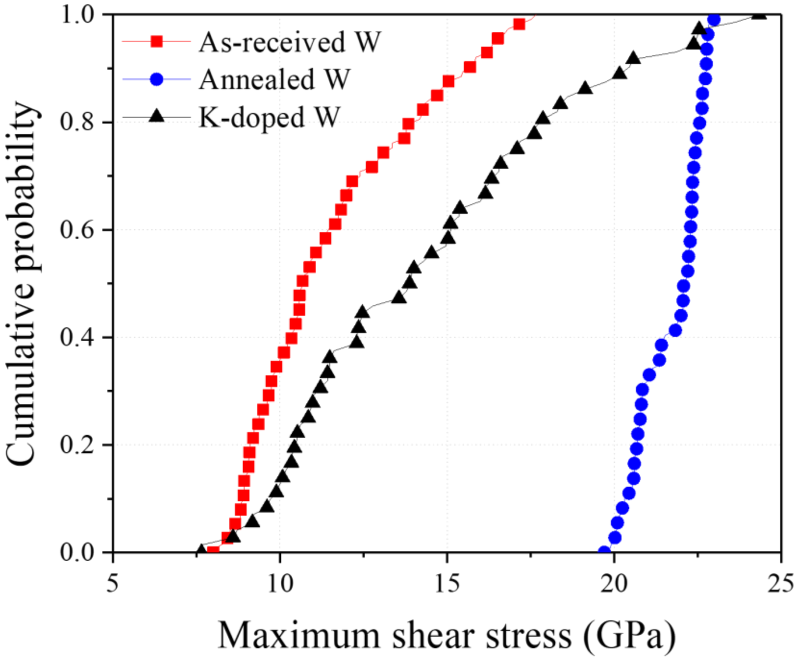

Figure 40 The maximum shear stress for yielding in As-received W, Annealed W, and K-doped W.

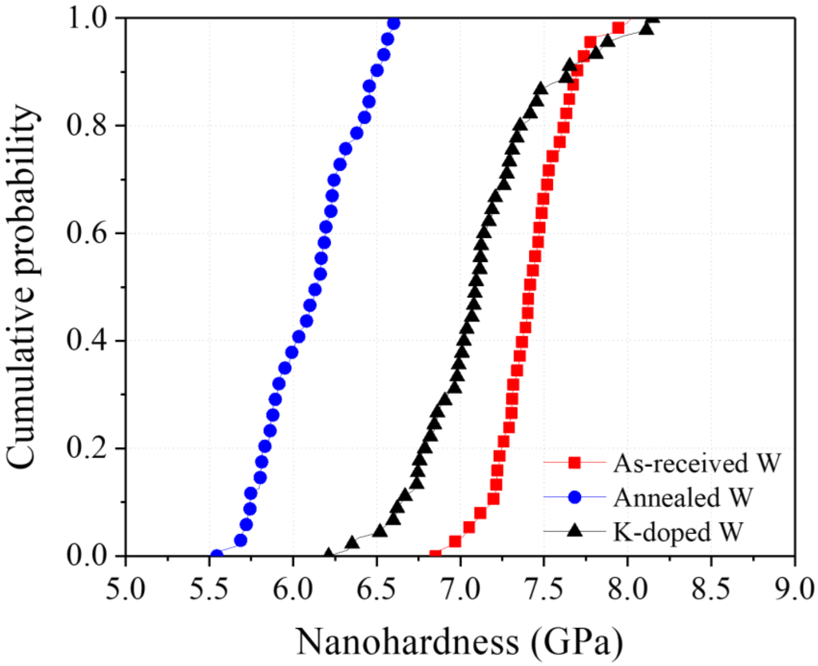

Figure 41 The nanohardness in As-received W, Annealed W, and K-doped W.

Table 6 Diameter of contact surface at the pop-in event and maximum shear stress of as-received W, annealed W, and K-doped W. Only those indentations inside the grains and a sufficient distance from the grain boundaries were considered for the calculation of average values. The number of indentations included in the calculation is listed in the last column.

Specimen	Diameter of contact surface (nm)		Maximum shear stress (GPa)		No. of indentations
	Avg.	Std.	Avg.	Std.	
As-received W	59	13.1	11.5	2.54	114
Annealed W	124	6.5	21.7	0.94	108
K-doped W	79	23.3	14.3	4.20	73

3.3.4 Molecular dynamics simulations for nanoindentation

Molecular dynamics simulations were conducted to analyze the influence of nano-sized K-bubbles within the grains on dislocation behavior. Figures 42 (a and b) show snapshots at a point that dislocation was firstly generated during molecular dynamics simulations of perfect crystals and crystals with nano-sized bubbles, and are correspond to 22.2 ps and 24.0 ps, respectively. It is noteworthy that dislocations were formed near bubble in the simulation for single crystal with nano-sized bubble, indicating that the presence of nano-sized bubble induces stress concentration in the surrounding matrix [64, 65]. Consequently, even if the applied stress is smaller than the theoretical shear stress, a localized stress higher than the theoretical shear stress may occur in the vicinity of the bubble, leading to the nucleation of dislocations in that region. Figure 42 (c) shows the load-displacement curves calculated from molecular dynamics simulations. The circles in the Figure 42 (c) represent the points at which the pop-in phenomenon occurred in both the perfect crystal and the crystal with nano-sized bubble. It confirms that the presence of nano-sized bubbles in tungsten can reduce the pop-in load.

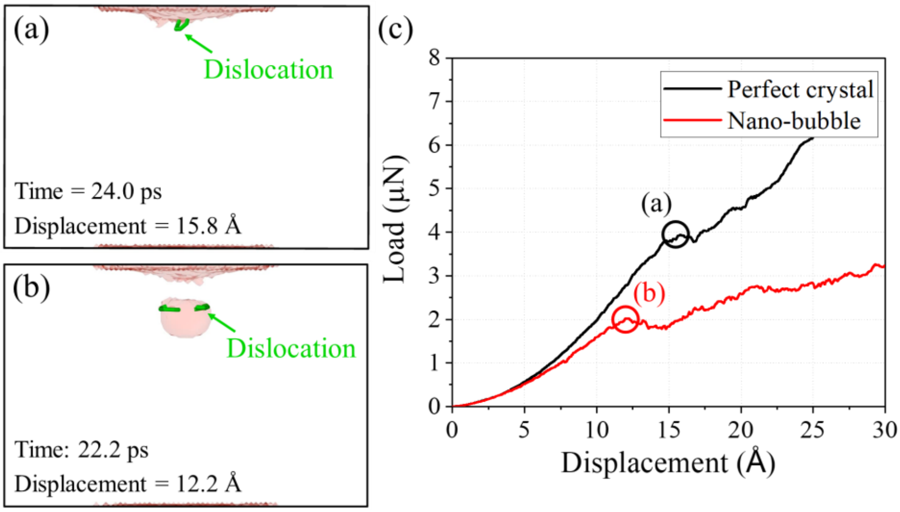

Figure 42 Snapshots at the time of pop-in event during molecular dynamics simulations; (a) perfect single crystal of tungsten, (b) single crystal of tungsten with a nano-sized bubble. (c) Load-displacement curves obtained from the simulations; the black and red circles are corresponded with (a) and (b).

3.3.5 Dislocation dynamics simulation for nanoindentation

Prior to DD simulation, FEM analysis was conducted to assess the extent of stress concentration induced around nano-sized bubbles during the nanoindentation test (Figure 43). Figure 44 presents the outcomes of simulations carried out by varing the sizes and positions of the nano-sized bubbles. Remarkably, when a nano-sized bubble with a radius of 25 nm was positioned 50 nm from the indentation surface, a von Mises stress of 31.9 GPa was observed near the bubble, which was higher than 26.9 GPa obtained in a perfect crystal (Table 7). It is noteworthy that the diameter of the bubble is similar to the average size of the K-bubbles (55.52 ± 23.64 nm, Figure 33 (b)) observed in the K-doped W specimen. In contrast, the simulations conducted under different conditions, including larger bubble diameters or deeper depths of bubble, did not exhibit notable stress concentration effects in the matrix surrounding the nano-sized bubble. It suggests the presence of a threshold size and position of the nano-sized bubble required to amplify the external stress by stress concentration. Based on the FEM results, we set the radius and depth of bubble to 25 nm and 50 nm for the following DD simulations.

DD simulations were conducted to examine the influence of the size, location, and number of nano-sized bubbles on the nucleation and movement of dislocations in tungsten. Figure 45 illustrates the load-displacement curve of a single crystal tungsten specimen with varying numbers of nano-sized bubbles. In the case of single crystal tungsten containing nano-sized pores, the pop-in phenomenon occurred at lower stress state compared to perfect crystal tungsten. It suggests that the presence of nano-sized bubbles promotes the nucleation of dislocations in tungsten, which is consistent with the MD simulations. Conversely, when comparing simulations with a single nano-sized bubble to those with four nano-sized bubbles, there is only minimal difference in the pop-in stress. Figure 46 shows the load-displacement curves of single crystal tungsten specimens with varying dislocation densities. For single crystal tungsten specimens with a high density of dislocations, the pop-in phenomenon occurred at a lower stress compared to a perfect crystal without dislocations. This behavior can be attributed to the presence of numerous mobile dislocations, which enable plastic deformation through the gliding of dislocations at lower stress state. These findings provide further support to the results obtained from nanoindentation experiments.

The results of the dislocation dynamics (DD) simulations are presented in Table 8. The "analytic" maximum shear stress was obtained based on the pop-in load using Equation 12 in Section 2.3.5, without considering the presence of a nano-sized bubble. On the other hand, the "numerical" maximum shear stress was calculated at the localized region where dislocations were nucleated in each DD simulation. In the case of a perfect tungsten crystal without any dislocations (simulation 1, Table 8), the analytic and numerical maximum shear stresses were found to be similar to each other, and these values were close to the theoretical shear stress of tungsten (~25 GPa). It validates the accuracy of the DD simulations. In the cases of single crystals containing nano-sized bubble (simulations 2 and 3, Table 8), the numerical maximum shear stress remains almost unchanged compared to simulation 1, indicating that the stress required for nucleating dislocations is the same as in a perfect tungsten crystal. However, the analytic maximum shear stress in these simulations significantly decreases. It clearly explains that the presence of nano-sized bubbles amplifies the stress in the localized region surrounding them through stress concentration, thereby enabling dislocation nucleation at a lower external stress state. In the simulation of a single crystal containing a large number of dislocations (simulation 4, Table 8), both the analytic and numerical maximum shear stresses decrease compared to those in the simulation for a perfect tungsten crystal. It indicates a transition in the dominant mechanism for plastic deformation from dislocation nucleation to the gliding of mobile dislocations.

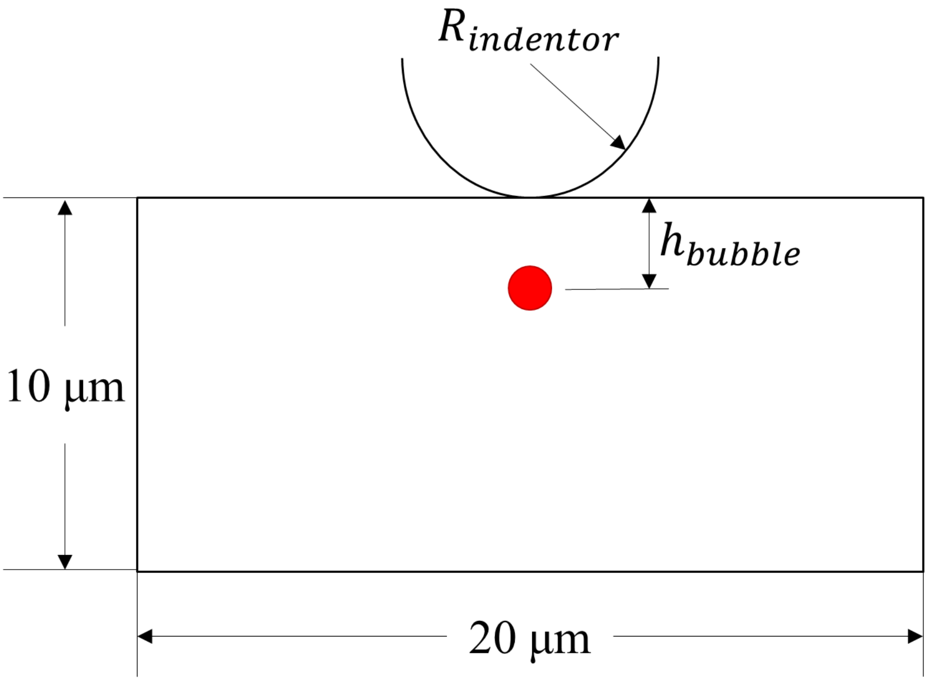

Figure 43 Schematic diagram of FEM simulations

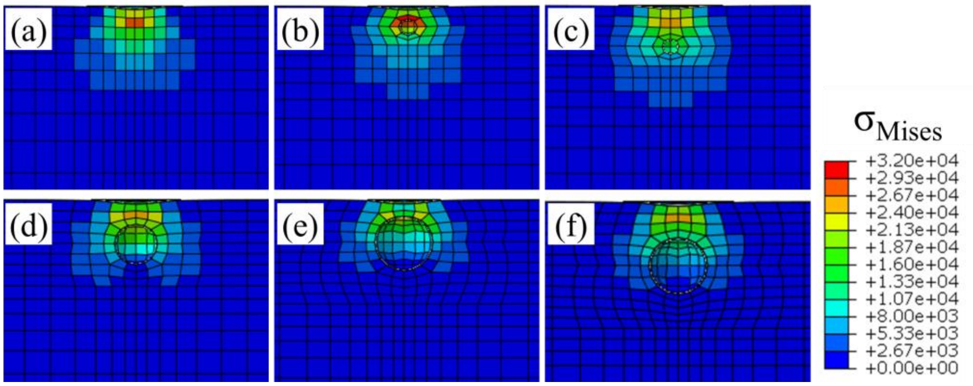

Figure 44 Distribution of von Mises stress in a perfect single crystal and single crystals with a nano-sized bubble simulated by FEM; diameters and depths of the bubble in the FEM simulations are represented in Table 7.

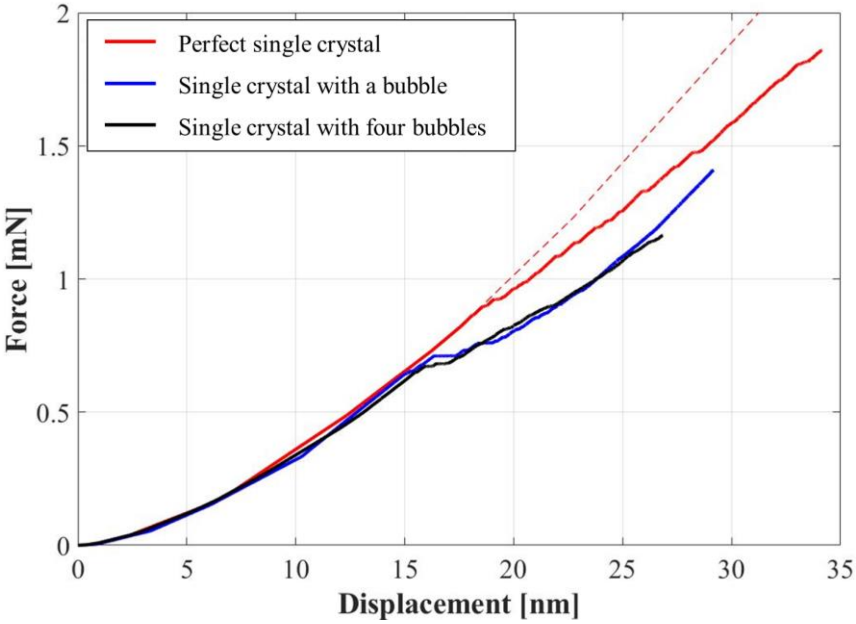

Figure 45 the load-displacement curves of the dislocation dynamics simulations for perfect single crystal, single crystal with a bubble, and single crystal with four bubbles.

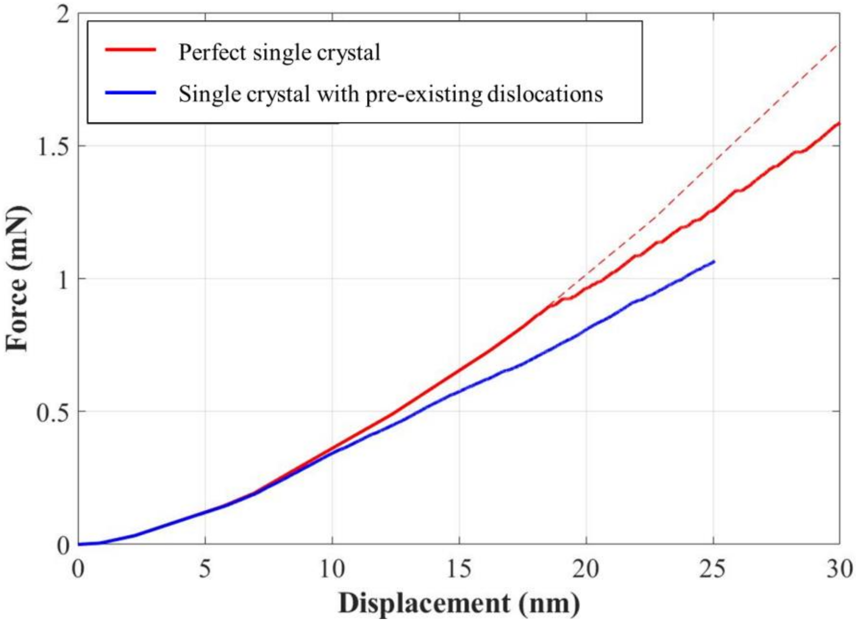

Figure 46 the load-displacement curves of the dislocation dynamics simulations for perfect single crystal, and single crystal with pre-existing dislocations ($\rho = 10^{14} m^{-2}$).

Table 7 Von Mises Stress at indentation depth of 10 nm were calculated by FEM simulations with various diameters and depths of bubble.

Simulations	Diameter (nm)	Depth (nm)	Von Mises Stress (GPa)
a (perfect crystal)	-	-	26.9
b	25	50	31.9
c	25	100	26.6
d	50	100	26.4
e	70	100	22.4
f	70	150	24.9

Table 8 Maximum shear stresses were calculated by DD simulations

Index	Bubble	Dislocation density (m^{-2})	Pop-in depth (nm)	Pop-in load (mN)	Maximum shear stress (analytic) (GPa)	Maximum shear stress (numerical) (GPa)
1	Without nano-sized bubble	0	17.90	0.848	19.55	20.38
2	With nano-sized bubble	0	14.79	0.629	17.69	20.16
3	With nano-sized bubble	0	15.31	0.639	17.78	19.76
4	Without nano-sized bubble	10^{14}	10.34	0.358	14.65	13.25

3.3.6 Effect of potassium-doping on plasma-facing properties of tungsten

Figure 47 illustrates the microstructure of K-doped W specimens before and after heat treatment at 1700 °C for varying durations. From the figure, it is evident that there is minimal change in the microstructure pre- and post-heat treatment. The average grain sizes of the specimens were measured as 3.20 ± 1.24 μm, 3.53 ± 1.52 μm, and 3.57 ± 1.41 μm in the initial specimen, the specimen subjected to a 3-hour heat treatment, and the specimen subjected to a 10-hour heat treatment, respectively. Likewise, the hardness values of the three specimens were measured as 465.00 ± 4.55 HV_3, 469.52 ± 2.98 HV_3, and 469.51 ± 3.19 HV_3, respectively, indicating no significant change. It is attributed to the pinning effect on grain boundaries by nano-sized the K-bubbles, which effectively inhibits grain growth.

To assess the resistance of K-doped W to deuterium ion irradiation, a D_2^+ ion irradiation test was conducted on the surface of the K-doped W specimen. Figure 48 illustrates the microstructural changes in the specimen before and after deuterium irradiation. Interestingly, despite the development of a nanostructure on the surface, no blister formation was observed after D_2^+ ion bombardment. This significant resistance to D_2^+ ions is potentially attributed to the presence of nano-sized K-bubbles. The incident deuterium ions tend to precipitate and form deuterium gas at trapping sites. When numerous trapping sites are present in a material, the deuterium ions cannot accumulate at a specific location and cannot exert sufficient pressure for blister formation. Given that the nano-sized K-bubbles can also serve as trapping sites, it is plausible that K-doped W exhibits high stability under D_2^+ ion irradiation.

The TDS experiment was conducted to evaluate the amount of deuterium retention in the K-doped W specimen, in comparison to SPSed Pure W (the same as described in Chapter 2) and commercially available pure tungsten (the same as As-received W in this chapter) (Figure 49). The results reveal that the retention of deuterium in the K-doped W specimen, following D_2^+ ion irradiation, is higher than that in SPSed Pure W but lower than that in As-received W. It can be attributed to the presence of nano-sized K-bubbles acting as trapping sites. However, the nano-sized K-bubbles may not be sufficient to retain deuterium ions exceeding the retention observed in As-received W, due to the relatively low potassium composition. The result suggest that the K-doped W could be suitable candidates for the plasma-facing material in the practical nuclear fusion reactor.

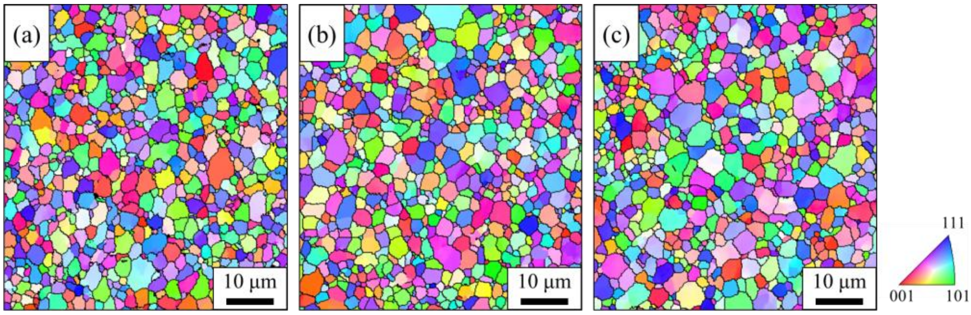

Figure 47 the inverse pole figures along the normal direction of the observed surface of heat-treated K-doped W specimens; (a) initial, (b) 3 h heat-treated, and (c) 10 h heat-treated sample.

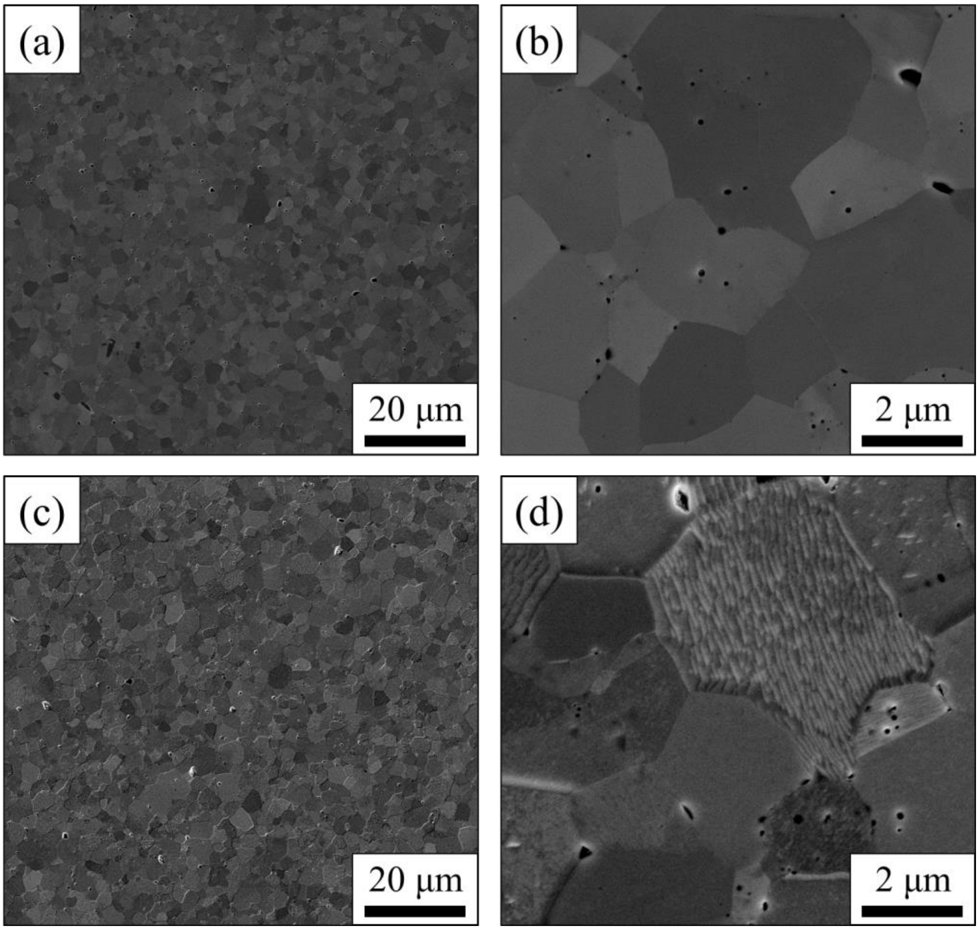

Figure 48 Surface morphologies of K-doped W (a, b) before and (c, d) after deuterium irradiation.

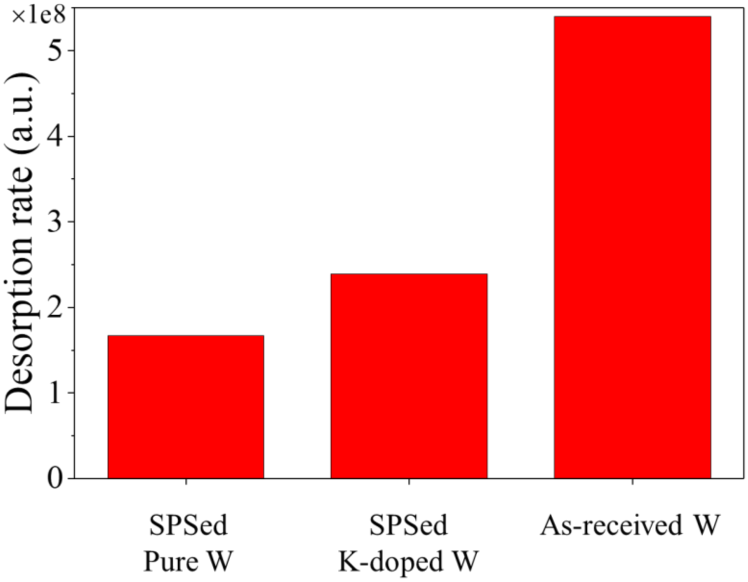

Figure 49 TDS results of SPSed Pure W, SPSed K-doped W, and As-received W specimens. (the SPSed Pure W specimen is the same as the one described in Chapter 2)

3.4. Conclusion

In this study, we systematically analyzed the effect of nano-sized K-bubbles in tungsten on their mechanical behavior using both experimental and computational methods. Consequently, the following conclusions were obtained:

1. It has been verified through TEM observations that K-doped W contains spherical bubbles with an average size of 55.52 nm. Additionally, EDS analysis confirmed that these bubbles are formed by potassium.

2. Based on the results of the uniaxial tensile test, it was found that the DBTT of K-doped W is approximately in the range of 300-320°C. This DBTT value is similar to that of the As-received W (300-330°C) and lower than that of the Annealed W (350-400°C).

3. The nanoindentation test results revealed that the maximum shear stress for yielding in K-doped W was significantly lower compared to Annealed W, despite having a similar dislocation density.

4. Through MD and DD simulations, it has been confirmed that nano-sized bubbles can facilitate the nucleation of dislocations under low macroscopic stress, owing to localized stress concentration in their vicinity.

5. After heat treatment of K-doped W at 1700 °C for various durations, changes in hardness and microstructure were observed. The results show that even after 10 hours of heat treatment, the specimen retained its high hardness and small grain size. It can be attributed to the low dislocation density and the pinning effect by K-bubbles.

6. The deuterium irradiation experiment demonstrates that K-doped W exhibits excellent resistance to ion irradiation and lower deuterium retention compared to As-received W. These findings suggest that the K-doped W specimen could be a suitable candidate for the plasma-facing material in practical nuclear fusion reactors.

3.5. References

[1] M. Merola, D. Loesser, A. Martin, P. Chappuis, R. Mitteau, V. Komarov, R.A. Pitts, S. Gicquel, V. Barabash, L. Giancarli, J. Palmer, M. Nakahira, A. Loarte, D. Campbell, R. Eaton, A. Kukushkin, M. Sugihara, F. Zhang, C.S. Kim, R. Raffray, L. Ferrand, D. Yao, S. Sadakov, A. Furmanek, V. Rozov, T. Hirai, F. Escourbiac, T. Jokinen, B. Calcagno, S. Mori, ITER plasma-facing components, Fusion Engineering and Design 85(10-12) (2010) 2312-2322.

[2] G. Pintsuk, Tungsten as a Plasma-Facing Material, Comprehensive Nuclear Materials2012, pp. 551-581.

[3] S. Wurster, N. Baluc, M. Battabyal, T. Crosby, J. Du, C. García-Rosales, A. Hasegawa, A. Hoffmann, A. Kimura, H. Kurishita, R.J. Kurtz, H. Li, S. Noh, J. Reiser, J. Riesch, M. Rieth, W. Setyawan, M. Walter, J.H. You, R. Pippan, Recent progress in R&D on tungsten alloys for divertor structural and plasma facing materials, Journal of Nuclear Materials 442(1-3) (2013) S181-S189.

[4] C. Yin, D. Terentyev, T. Pardoen, R. Petrov, Z. Tong, Ductile to brittle transition in ITER specification tungsten assessed by combined fracture toughness and bending tests analysis, Materials Science and Engineering: A 750 (2019) 20-30.

[5] P. Gumbsch, Brittle fracture and the brittle-to-ductile transition of tungsten, Journal of Nuclear Materials 323(2-3) (2003) 304-312.

[6] A. Giannattasio, M. Tanaka, T.D. Joseph, S.G. Roberts, An empirical correlation between temperature and activation energy for brittle-to-ductile transitions in single-phase materials, Physica Scripta T128 (2007) 87-90.

[7] S. Nogami, S. Watanabe, J. Reiser, M. Rieth, S. Sickinger, A. Hasegawa, A review of impact properties of tungsten materials, Fusion Engineering and Design 135 (2018) 196-203.

[8] J.-H. You, M. Li, K. Zhang, Structural lifetime assessment for the DEMO divertor targets: Design-by-analysis approach and outstanding issues, Fusion Engineering and Design 164 (2021).

[9] M. Wirtz, J. Linke, T. Loewenhoff, G. Pintsuk, I. Uytdenhouwen, Thermal shock tests to qualify different tungsten grades as plasma facing material, Physica Scripta T167 (2016).

[10] G. Pintsuk, I. Bobin-Vastra, S. Constans, P. Gavila, M. Rödig, B. Riccardi, Qualification and post-mortem characterization of tungsten mock-ups exposed to cyclic high heat flux loading, Fusion Engineering and Design 88(9-10) (2013) 1858-1861.

[11] A. Sharma, Y. Morisada, T. Nagaoka, H. Fujii, Enhanced strength-ductility combination in the cold-rolled spark plasma sintered pure aluminium by FSP, Materials Characterization 188 (2022).

[12] Y. Lee, E.S. Kim, S. Park, J.M. Park, J.B. Seol, H.S. Kim, T. Lee, H. Sung, J.G. Kim, Effects of Laser Power on the Microstructure Evolution and Mechanical Properties of Ti–6Al–4V Alloy Manufactured by Direct Energy Deposition, Metals

and Materials International 28(1) (2021) 197-204.

[13] Z. Tang, W. Xiong, J. Zhang, Y. Zheng, C. Huang, Simultaneously Enhancing the Strength and Ductility of Spin-Extruded 2195 Al–Li Alloy by Grain Configuration Tunning, Metals and Materials International (2022).

[14] X. Liu, M. Zhou, X. Zhang, Ultra-flash annealing constructed heterogeneous austenitic stainless steel with excellent strength-ductility, Materials Characterization 192 (2022).

[15] E. Ma, Instabilities and ductility of nanocrystalline and ultrafine-grained metals, Scripta Materialia 49(7) (2003) 663-668.

[16] M. Zhao, Z. Zhou, Q. Ding, M. Zhong, K. Arshad, Effect of rare earth elements on the consolidation behavior and microstructure of tungsten alloys, International Journal of Refractory Metals and Hard Materials 48 (2015) 19-23.

[17] C. Linsmeier, M. Rieth, J. Aktaa, T. Chikada, A. Hoffmann, J. Hoffmann, A. Houben, H. Kurishita, X. Jin, M. Li, A. Litnovsky, S. Matsuo, A. von Müller, V. Nikolic, T. Palacios, R. Pippan, D. Qu, J. Reiser, J. Riesch, T. Shikama, R. Stieglitz, T. Weber, S. Wurster, J.H. You, Z. Zhou, Development of advanced high heat flux and plasma-facing materials, Nuclear Fusion 57(9) (2017).

[18] R. Wang, Z.M. Xie, Y.K. Wang, J.P. Song, Q.F. Fang, R. Liu, Y. Jiang, J.F. Yang, T. Zhang, X.P. Wang, C.S. Liu, Fabrication and characterization of nanocrystalline ODS-W via a dissolution-precipitation process, International Journal of Refractory Metals and Hard Materials 80 (2019) 104-113.

[19] Z.S. Levin, K.T. Hartwig, Strong ductile bulk tungsten, Materials Science and Engineering: A 707 (2017) 602-611.

[20] Y. Oh, N. Kwak, K. Lee, W.-S. Ko, H.N. Han, Ductility enhancement of tungsten after plastic deformation, Journal of Alloys and Compounds 787 (2019) 801-814.

[21] C. Lai, J. Wang, F. Zhou, W. Liu, N. Miao, Reduction, sintering and mechanical properties of rhenium-tungsten compounds, Journal of Alloys and Compounds 735 (2018) 2685-2693.

[22] P. Schade, 100years of doped tungsten wire, International Journal of Refractory Metals and Hard Materials 28(6) (2010) 648-660.

[23] C. Ren, Z.Z. Fang, M. Koopman, B. Butler, J. Paramore, S. Middlemas, Methods for improving ductility of tungsten - A review, International Journal of Refractory Metals and Hard Materials 75 (2018) 170-183.

[24] S. Watanabe, S. Nogami, J. Reiser, M. Rieth, S. Sickinger, S. Baumgärtner, T. Miyazawa, A. Hasegawa, Tensile and impact properties of tungsten-rhenium alloy for plasma-facing components in fusion reactor, Fusion Engineering and Design 148 (2019).

[25] D.D. Caillard, A TEM in situ study of the softening of Tungsten by Rhenium, Acta Materialia 194 (2020) 249-256.

[26] Y.-H. Li, H.-B. Zhou, L. Liang, N. Gao, H. Deng, F. Gao, G. Lu, G.-H. Lu, Transition from ductilizing to hardening in tungsten: The dependence on rhenium distribution, Acta Materialia 181 (2019) 110-123.

[27] X. Yang, W. Qiu, L. Chen, J. Tang, Tungsten–potassium: a promising plasma-facing material, Tungsten 1(2) (2019) 141-158.

[28] B. Huang, J. Tang, L. Chen, X. Yang, Y. Lian, L. Chen, X. Liu, X. Cui, L. Gu, C.-T. Liu, Design of highly thermal-shock resistant tungsten alloys with nanoscaled intra- and inter-type K bubbles, Journal of Alloys and Compounds 782 (2019) 149-159.

[29] K. Sasaki, K. Yabuuchi, S. Nogami, A. Hasegawa, Effects of temperature and strain rate on the tensile properties of potassium-doped tungsten, Journal of Nuclear Materials 461 (2015) 357-364.

[30] K. Shi, B. Huang, B. He, Y. Xiao, X. Yang, Y. Lian, X. Liu, J. Tang, Room-temperature tensile strength and thermal shock behavior of spark plasma sintered W-K-TiC alloys, Nuclear Engineering and Technology 51(1) (2019) 190-197.

[31] H. Sheng, I. Uytdenhouwen, G. Van Oost, J. Vleugels, Mechanical properties and microstructural characterizations of potassium doped tungsten, Nuclear Engineering and Design 246 (2012) 198-202.

[32] B. Huang, L. Chen, W. Qiu, X. Yang, K. Shi, Y. Lian, X. Liu, J. Tang, Correlation between the microstructure, mechanical/thermal properties, and thermal shock resistance of K-doped tungsten alloys, Journal of Nuclear Materials 520 (2019) 6-18.

[33] J. Choi, H.-M. Sung, K.-B. Roh, S.-H. Hong, G.-H. Kim, H.N. Han, Fabrication of sintered tungsten by spark plasma sintering and investigation of thermal stability, International Journal of Refractory Metals and Hard Materials 69 (2017) 164-169.

[34] G. Min, Y. Oh, H. Kim, E. Shin, K.-B. Roh, J. Kim, N. Kwak, Y. Kim, H.C. Kim, G.-H. Kim, H.N. Han, Effect of yttrium doping in tungsten on sinterability and properties as a plasma-facing material, Journal of Alloys and Compounds 953 (2023).

[35] N. Kwak, G. Min, Y. Oh, D.-W. Suh, H.C. Kim, S.-g. Kang, H.N. Han, Tantalum and molybdenum barriers to prevent carbon diffusion in spark plasma sintered tungsten, Scripta Materialia 196 (2021).

[36] G. Ribárik, J. Gubicza, T. Ungár, Correlation between strength and microstructure of ball-milled Al–Mg alloys determined by X-ray diffraction, Materials Science and Engineering: A 387-389 (2004) 343-347.

[37] G. Ribárik, Modeling of diffraction patterns based on microstructural properties, Department of Materials Physics, Eötvös Loránd University

Institute of Physics, 2008.

[38] P.A. Redhead, Thermal desorption of gases, Vacuum 12(4) (1962) 203-211.

[39] A. Stukowski, Visualization and analysis of atomistic simulation data with OVITO–the Open Visualization Tool, Modelling and Simulation in Materials

Science and Engineering 18(1) (2010).

[40] A. Stukowski, K. Albe, Extracting dislocations and non-dislocation crystal defects from atomistic simulation data, Modelling and Simulation in Materials Science and Engineering 18(8) (2010).

[41] A. Stukowski, V.V. Bulatov, A. Arsenlis, Automated identification and indexing of dislocations in crystal interfaces, Modelling and Simulation in Materials Science and Engineering 20(8) (2012).

[42] Y. Oh, W.-S. Ko, N. Kwak, J.-i. Jang, T. Ohmura, H.N. Han, Small-scale analysis of brittle-to-ductile transition behavior in pure tungsten, Journal of Materials Science & Technology 105 (2022) 242-258.

[43] S. Nosé, A unified formulation of the constant temperature molecular dynamics methods, The Journal of Chemical Physics 81(1) (1984) 511-519.

[44] W.G. Hoover, Canonical dynamics: Equilibrium phase-space distributions, Phys Rev A Gen Phys 31(3) (1985) 1695-1697.

[45] A. Arsenlis, W. Cai, M. Tang, M. Rhee, T. Oppelstrup, G. Hommes, T.G. Pierce, V.V. Bulatov, Enabling strain hardening simulations with dislocation dynamics, Modelling and Simulation in Materials Science and Engineering 15(6) (2007) 553-595.

[46] K. Tsuchida, T. Miyazawa, A. Hasegawa, S. Nogami, M. Fukuda, Recrystallization behavior of hot-rolled pure tungsten and its alloy plates during high-temperature annealing, Nuclear Materials and Energy 15 (2018) 158-163.

[47] C. Ren, Z.Z. Fang, L. Xu, J.P. Ligda, J.D. Paramore, B.G. Butler, An investigation of the microstructure and ductility of annealed cold-rolled tungsten, Acta Materialia 162 (2019) 202-213.

[48] B.E. Warren, X-Ray Studies of Deformed Metals, Prog Met Phys 8 (1959) 147-202.

[49] B.E. Warren, B.L. Averbach, The Separation of Cold-Work Distortion and Particle Size Broadening in X-Ray Patterns, Journal of Applied Physics 23(4) (1952) 497-497.

[50] M. Wilkens, The determination of density and distribution of dislocations in deformed single crystals from broadened X-ray diffraction profiles, Physica Status Solidi (a) 2(2) (1970) 359-370.

[51] T. Ungar, I. Dragomir, A. Revesz, A. Borbely, The contrast factors of dislocations in cubic crystals: the dislocation model of strain anisotropy in practice, Journal of Applied Crystallography 32 (1999) 992-1002.

[52] T. Ungár, A. Borbély, The effect of dislocation contrast on x-ray line broadening: A new approach to line profile analysis, Applied Physics Letters 69(21) (1996) 3173-3175.

[53] Z.H. Cong, Y. Murata, Dislocation Density of Lath Martensite in 10Cr-5W Heat-Resistant Steels, Materials Transactions 52(12) (2011) 2151-2154.

[54] E. Lassner, W.-D. Schubert, Tungsten: properties, chemistry, technology of the elements, alloys, and chemical compounds, Springer Science & Business Media1999.

[55] B. Gludovatz, S. Wurster, A. Hoffmann, R. Pippan, Fracture toughness of polycrystalline tungsten alloys, International Journal of Refractory Metals and Hard Materials 28(6) (2010) 674-678.

[56] B. Gludovatz, S. Wurster, T. Weingärtner, A. Hoffmann, R. Pippan, Influence of impurities on the fracture behaviour of tungsten, Philosophical Magazine 91(22) (2011) 3006-3020.

[57] M.L. Martin, B.P. Somerday, R.O. Ritchie, P. Sofronis, I.M. Robertson, Hydrogen-induced intergranular failure in nickel revisited, Acta Materialia 60(6-7) (2012) 2739-2745.

[58] J. Riesch, Y. Han, J. Almanstötter, J.W. Coenen, T. Höschen, B. Jasper, P. Zhao, C. Linsmeier, R. Neu, Development of tungsten fibre-reinforced tungsten composites towards their use in DEMO—potassium doped tungsten wire, Physica Scripta T167 (2016).

[59] V. Shah, J.A.W. van Dommelen, E. Altstadt, A. Das, M.G.D. Geers, Brittle-ductile transition temperature of recrystallized tungsten following exposure to fusion relevant cyclic high heat load, Journal of Nuclear Materials 541 (2020).

[60] C.A. Schuh, Nanoindentation studies of materials, Mater Today 9(5) (2006) 32-40.

[61] T.H. Ahn, C.S. Oh, D.H. Kim, K.H. Oh, H. Bei, E.P. George, H.N. Han, Investigation of strain-induced martensitic transformation in metastable austenite using nanoindentation, Scripta Materialia 63(5) (2010) 540-543.

[62] T.-H. Ahn, C.-S. Oh, K. Lee, E.P. George, H.N. Han, Relationship between yield point phenomena and the nanoindentation pop-in behavior of steel, Journal of Materials Research 27(1) (2011) 39-44.

[63] T.H. Courtney, Mechanical behavior of materials, Waveland Press2005.

[64] I. Sevostianov, V. Kushch, Effect of pore distribution on the statistics of peak stress and overall properties of porous material, International Journal of Solids and Structures 46(25-26) (2009) 4419-4429.

[65] T. Davis, D. Healy, A. Bubeck, R. Walker, Stress concentrations around voids in three dimensions: The roots of failure, Journal of Structural Geology 102 (2017) 193-207.

Chapter 4. Conclusions and Outlook

In order to develop tungsten as a plasma-facing material (PFM), the effects of two different doping elements, yttrium and potassium, on properties of tungsten were investigated. By employing powder metallurgical techniques, the defects induced by these doping elements, including yttrium-rich particles and potassium bubbles, were uniformly dispersed throughout fully densified tungsten matrix. Notably, Despite the low contents of these alloying elements, they exhibited a significant influence on various properties of tungsten, such as sinterability, mechanical properties, and plasma-facing properties. To gain a profound understanding of the relationship between the addition of elements and the improvement of properties, a comprehensive investigation was conducted through experiments and simulations. The significant conclusions elicited from this thesis are discussed below.

In Chapter 2, the properties of yttrium-doped tungsten fabricated through mechanical alloying and subsequent internal oxidation during spark plasma sintering (SPS) were comprehensively investigated. The transmission electron microscopy (TEM) and small-angle neutron scattering experiments revealed a homogeneous distribution of 0.05 wt.% Y_2O_3 particles with an average size of approximately 20 nm within the tungsten matrix. Despite the low concentration, these Y_2O_3 particles exert a significant influence on various properties of tungsten, including sinterability, plasma-facing characteristics, and microscopic mechanical properties. Firstly, it contributes to enhance the sinterability of tungsten through expedited grain boundary diffusion of tungsten atoms during the sintering process. Secondly, the pinning effect exerted by nano-sized Y_2O_3 particles contributes to the maintenance of a fine-grained microstructure at high temperatures, subsequently leading to a decrease in defects induced by plasma ion bombardments such as blisters. Finally, the dislocations generated during the sintering process contributes to an increase in the microscopic ductility and nanohardness of tungsten.

In Chapter 3, the study focused on elucidating the underlying mechanism responsible for the reduction of the ductile-to-brittle transition temperature (DBTT) in potassium-doped tungsten (K-doped W) through a combination of experimental and computational methods. The fabrication of the K-doped W specimens was carried out using SPS, employing optimized processing conditions to prevent abnormal grain growth. TEM analysis revealed the presence of nano-sized bubbles with an average size of approximately 30 nm in the K-doped W specimen, formed through the vaporization of potassium during the fabrication process. By performing a comparative analysis of the dislocation density and maximum shear stress between K-doped W and pure tungsten specimens, it is concluded that the nucleation of dislocations plays a dominant role in the plastic deformation behavior in K-doped W. The nucleation of dislocations was found to be significantly facilitated by stress concentration in the localized region near the nano-sized bubble. it was demonstrated by molecular dynamics and dislocation dynamics simulations. In addition, the thermal stability and the resistance for deuterium irradiation of K-doped W were evaluated.

For the realization of nuclear fusion reactor, the selection of a PFM is important due to the extreme operational environment within the fusion reactor. Although tungsten is widely regarded as the most promising candidates for plasma-facing materials, several challenging issues, such as a low recrystallization temperature and high DBTT, still were remained. Given that impurities can lead to plasma instability in nuclear reactors, such issues should be addressed through minimal additions of alloying elements. In this study, we investigated the alloying effects of two different doping elements on the properties of tungsten. Both yttrium and potassium doping beneficially influenced the properties of tungsten required as a PFM. Therefore, these findings will have significant implications for the further development of PFM.

국문 초록

텅스텐은 높은 융점, 높은 열전도율, 낮은 침식률 등의 우수한 특성 조합으로 인해 차세대 핵융합로의 플라즈마 대면 부품에 선호되고 있는 대표 후보물질 중 하나이다. 그러나 텅스텐의 낮은 재결정 온도와 높은 연성-취성 천이 온도는 핵융합 환경에서의 적용을 크게 제한한다. 따라서 텅스텐의 물성을 향상시키기 위해서 다양한 합금 원소를 첨가하는 연구들이 이루어지고 있다. 그러나 첨가 원소가 핵융합로에 유입되면 플라즈마의 불안정성을 야기할 수 있으므로, 텅스텐을 플라즈마 대면재로 활용하기 위해서는 합금 원소의 양이 어느 수준으로 제한될 필요가 있다. 본 연구에서는 분말 야금학적 방법을 활용하여 미량의 합금 원소(이트륨 및 포타슘)가 기지상에 균일하게 분산된 텅스텐 소재를 제작하고, 플라즈마 대면 특성과 기계적 특성을 평가하였다. 또한, 합금 원소 첨가와 물성의 상관 관계를 파악하기 위해 다양한 실험 및 계산이 수행되었다.

첫째, 미량의 이트륨 첨가가 텅스텐의 물성에 미치는 영향을 조사하였다. 0.05 wt.% 이하의 이트륨을 기계적 합금화를 통해 텅스텐 분말에 분산하고, 이어지는 통전활성소결 공정에서 잔류 산소와의 반응을 통해 이트륨 산화물을 기지상에 균일하게 형성시켰다. 이트륨 산화물은 평균 입자 크기가 약 20 nm인 이트리아 (Y_2O_3)로 확인되었다. 나노 크기의 Y_2O_3는 결정립계를 고정하여 조밀한 미세구조 형성과 고온에서의 결정립 성장 억제에 기여하였다. 또한, 재료의 높은 입계 분율은 소결 중 텅스텐 원자의 입계 확산을 촉진하여 결과적으로 소결성을 향상시켰다. 핵융합로에서 재료의 활용 가능성을 평가하기 위하여, 중수소 및 헬륨 이온 조사에 대한 저항성 평가가 수행되었으며, Y_2O_3가 분산된 시편의 조사 저항성이 순수 텅스텐 시편들에 비해 우수한 것으로 확인되었다. 또한, Y_2O_3 입자가 텅스텐의 국소적인 기계적 성질에 미치는 영향을 분석하기 위해 나노압입 시험이 수행되었다. Y_2O_3가 분산된 텅스텐에서 최대 전단 응력의 분포는 평균값이 다른 두 로그정규분포의 합으로 나타났으며, 이는 소결 중에 Y_2O_3에 의해 도입된 전위의 이동이 재료의 국소적 항복 응력을 감소시켰기 때문이다.

둘째, 미량의 포타슘 첨가가 텅스텐의 물성에 미치는 영향을 조사하였다. 포타슘이 33 wt ppm 가량 도핑된 텅스텐 분말을 사용하여 비정상 결정립이 형성되지 않는 조건에서 소결을 수행하였다. 소결 중 포타슘의 기화는 텅스텐 기지상에 미세한 거품을 형성시켰으며, 평균 거품 크기는 약 30 nm였다. 일축 인장 시험은 포타슘이 도핑된 텅스텐 시편이 비슷한 전위 분포를 가지는 순수 텅스텐에

비해 낮은 DBTT를 가진다는 사실을 보였다. 포타슘이 도핑된 텅스텐과 순수 텅스텐 시편들의 전위 밀도와 최대 전단 응력을 비교 분석하여, 전위의 핵생성이 포타슘이 도핑된 텅스텐의 소성 변형에 지배적인 역할을 한다는 것을 발견하였다. 분자 동역학 및 전위 동역학 모사는 나노압입시험 중에 포타슘에 의한 나노 크기의 거품이 주변의 기지상에 응력을 집중시키며, 따라서 더 낮은 외부 응력에서 전위가 핵성성 된다는 사실을 증명하였다. 이를 통해, 우리는 포타슘이 도핑된 텅스텐에서 DBTT가 감소하는 메커니즘을 완전히 이해하였다. 또한, 포타슘이 도핑된 텅스텐의 플라즈마 대면 성질을 평가하였으며, 열적 안정성과 중수소 이온 조사 저항성이 우수함을 확인하였다.

이 연구를 통해 우리는 미량의 합금 원소 첨가만으로도 텅스텐의 물성을 크게 향상시킬 수 있다는 사실을 확인하였다. 소량의 원소를 기지상에 균일하게 분산시키는 생산 기술과 물성 향상 메커니즘에 대한 포괄적인 이해는 앞으로의 고순도 텅스텐 대면 소재 제작 기술 개발을 위한 주춧돌이 될 것이라 예상한다. 마지막으로, 본 연구의 개념은 다양한 극한환경 대응용 소재 분야에서 획기적인 진전을 가져오고 새로운 분야를 개척할 수 있는 원동력을 제공할 것으로 기대된다.

핵심어 : 텅스텐, 플라즈마 대면재, 연성-취성 천이 온도, 이트륨, 포타슘, 플라즈마 대면 특성, 기계적 특성

Student Number : 2019-38391